POLITECNICO DI MILANO

SCUOLA INTERPOLITECNICA DI DOTTORATO

Doctoral Program in Physics

Final Dissertation

Electric field control of remanent states in magnetic and ferroelectric tunnel junctions

Greta Radaelli

Tutor
prof. Riccardo Bertacco

Co-ordinator of the Research Doctorate Course
prof. Paola Taroni

February 2014

A chi c'è sempre stato

Abstract

Tunnel junctions consist of two metal electrodes separated by a very thin insulating barrier. Functional properties of tunnel junctions can be extended by using ferromagnetic materials as electrodes and/or ferroelectric ones as barrier, thanks to the tunnel magnetoresistance (TMR) and electroresistance (TER) effects. Tunnel junctions thus have great potential for application in real memory/logic devices, provided that room temperature switching between stable states can be controlled by an external electric field (E-field). This is a mandatory requirement in order to cope with the quest for higher storage density, higher speeds, and lower power consumption.

The ultimate goal of the present thesis is to investigate memory/logic devices based on tunnel junctions which are characterized by (at least) two well defined remanent resistance states that can be controlled by an external E-field. To that purpose, two different strategies have been used: A) E-field control of the remanent resistance states of a magnetic tunnel junction (MTJ) by using magnetoelectric coupling (MEC) effects at multiferroic (Fe/$BaTiO_3$) interfaces; B) E-field control of the remanent resistance states of a tunnel junction with FE barrier (FTJ) displaying TER effect. By consequence, the thesis is structured in two different blocks.

In the first block the study of magnetoelectric coupling at the fully epitaxial Fe/$BaTiO_3$ (BTO) interface for the E-field control of MTJ is presented. We will show that in fully epitaxial Fe/BTO systems, while strain-mediated MEC is suppressed likely due to clamping of BTO to the substrate, there is evidence for an undisclosed physical mechanism for interfacial MEC: the magnetization of the interfacial ultrathin oxidized iron layer (FeOx) can be electrically and reversibly switched on-off at room-temperature by reversing

the BTO polarization thanks to the asymmetric effect that ionic displacements in BTO produces on the exchange coupling constants in the adjacent FeOx layer.

The second block is instead devoted to the fabrication and characterization of FTJs. The E-field control of the remanent resistance states of large area FTJs displaying record room temperature TER effect has been achieved. Moreover we will show that integration in FTJs of half-doped manganites, intrinsically highly sensitive to external perturbations, is very promising to obtain an overall further enhancement of the TER effect.

Preface

This Thesis covers most of the work done from the beginning of the Ph.D. project on January 1st, 2011 by the author, Greta Radaelli. The principal supervisor has been Prof. R. Bertacco from the Politecnico di Milano. The experimental activity was carried out in two research centers:

- Laboratory for Nanostructure Epitaxy and Spintronics on Silicon (L-NESS), part of Politecnico di Milano, Como (Italy), under the supervision of Prof. R. Bertacco.
- Institut de Ciència de Materials de Barcelona (ICMAB-CSIC), Campus UAB, Bellaterra, Catalonia (Spain), during nine months stage (November 1st, 2012 - July 31st, 2013) under the supervision of Prof. J. Fontcuberta.

List of publications

- D. Gutiérrez, G. Radaelli, F. Sànchez, R. Bertacco and J. Fontcuberta, *Bandwidth-limited control of orbital and magnetic orders in half-doped manganites by epitaxial strain*, submitted to Physical Review B

- G. Radaelli, D. Petti, E. Plekhanov, I. Fina, B. R. Salles, M. Cantoni, C. Rinaldi, D. Gutiérrez, G. Panaccione, M. Varela, S. Picozzi, J. Fontcuberta and R. Bertacco, *Electrical on-off switching of magnetism at the Fe/$BaTiO_3$ interface*, submitted to Nature Communications

- G. Radaelli, M. Cantoni, M. Espahbodi, Li Lijiun and R. Bertacco, *Two dimensional growth of ultrathin Fe films on $BaTiO_3$ with sharp chemical interface*, submitted to Journal of Applied Physics

- G. Radaelli, D. Petti, M. Cantoni, C. Rinaldi and R. Bertacco, *Absence of strain-mediated magnetoelectric coupling at fully epitaxial Fe/$BaTiO_3$ interfaces*, Journal of Applied Physics, proceedings of the 58th Annual Conference on MMM Session CE: Electric and strain effects on magnetism and transport. In print

- G. Radaelli, S. Brivio, I. Fina and R. Bertacco, *Correlation between growth dynamics and dielectric properties of epitaxial $BaTiO_3$ films*, Applied Physics Letters 100, 102904 (2012)

List of communications[1]

- *58th Annual Conference on Magnetism and Magnetic M*aterials *(MMM)*, November 4-8 2013, Denver, Colorado, USA. "Room-temperature reversible electrical switching of the magnetic order at the Fe/$BaTiO_3$ interface", G. Radaelli, D. Petti, P. Torelli, B. R. Salles, I. Fina, D. Gutiérrez, E. Plekhanov, C. Rinaldi, M. Cantoni, S. Picozzi, J. Fontcuberta, G. Panaccione and R. Bertacco. TYPE: INVITED ORAL.

- *58th Annual Conference on Magnetism and Magnetic M*aterials *(MMM)*, November 4-8 2013, Denver, Colorado, USA. "Phase control of half-doped manganite thin films and electroresistance in hybrid ferroelectric/manganite tunnel junctions", D. Gutiérrez, G. Radaelli, N. Dix, F. Sànchez, R. Bertacco and J. Fontcuberta. TYPE: ORAL.

- *Workshop on Oxide Electronics (WOE20)*, September 22-25 2013, University Town, National University of Singapore. "Electrical switching of the magnetic order at the Fe/$BaTiO_3$ interface", G. Radaelli, D. Petti, P. Torelli, B. R. Salles, I. Fina, D. Gutiérrez, E. Plekhanov, C. Rinaldi, M. Cantoni, S. Picozzi, J. Fontcuberta, G. Panaccione and R. Bertacco. TYPE: POSTER.

- *Workshop on Oxide Electronics (WOE20)*, September 22-25 2013, University Town, National University of Singapore. "Half-doped manganite thin films for tunable electroresistance tunnel junctions", D. Gutiérrez, G. Radaelli, N. Dix, F. Sànchez, R. Bertacco and J. Fontcuberta. TYPE: POSTER.

[1] As presenting author.

- *Workshop on Oxide Electronics (WOE20)*, September 22-25 2013, University Town, National University of Singapore. "Room temperature electroresistance in $BaTiO_3$-based tunnel junctions", G. Radaelli, D. Gutiérrez, N. Dix, F. Sànchez, R. Bertacco and J. Fontcuberta. TYPE: ORAL.

- *Joint European Magnetic Symposia (JEMS 2013)*, August 25-30 2013, Rhodes, Greece. "Electrical switching of the magnetic order at the Fe/$BaTiO_3$ interface", G. Radaelli, D. Petti, P. Torelli, B. R. Salles, I. Fina, D. Gutiérrez, E. Plekhanov, C. Rinaldi, M. Cantoni, S. Picozzi, J. Fontcuberta, G. Panaccione and R. Bertacco. TYPE: ORAL.

- *Joint European Magnetic Symposia (JEMS 2013)*, August 25-30 2013, Rhodes, Greece. "Half-doped manganite thin films for tunable electroresistance tunnel junctions", D. Gutiérrez, G. Radaelli, N. Dix, F. Sànchez, R. Bertacco and J. Fontcuberta. TYPE: POSTER.

- *NANOSELECT 2013*, July 14-16 2013, St. Feliu de Guixols, Spain. "Room temperature electroresistance in $BaTiO_3$-based ferroelectric tunnel junctions", G. Radaelli, D. Gutiérrez, N. Dix, F. Sànchez, R. Bertacco and J. Fontcuberta. TYPE: ORAL.

- *Joint European Magnetic Symposia (JEMS 2012)*, September 9-14 2012, Parma, Italy. "Magnetoelectric effects at Fe/$BaTiO_3$(001) interface for new magnetic memory devices", G. Radaelli, D. Petti, C. Rinaldi, M. Cantoni and R. Bertacco. TYPE: ORAL.

- *International Conference on Magnetism (ICM 2012)*, July 8-13 2012, Bexco, Busan, South Korea. "Epitaxial Fe/MgO/Fe tunneling junctions on $BaTiO_3$(001)", G. Radaelli, S. Brivio and R. Bertacco. TYPE: ORAL.

- *SuperFOx 2012*, June 19-22 2012, Como, Italy. "Correlation between growth dynamics and dielectric properties of epitaxial $BaTiO_3$ films", G. Radaelli, S. Brivio, I. Fina, D. Chrastina and R. Bertacco. TYPE: POSTER.

- *SuperFOx 2012*, June 19-22 2012, Como, Italy. "Epitaxial Fe/MgO/Fe tunneling junctions on $BaTiO_3$(001)", G. Radaelli, S. Brivio and R. Bertacco. TYPE: ORAL.

- *International School of Oxide Electronics 2011*, October 3-15 2011, Cargèse, Corsica, France. "Magnetoelectric effects at Fe/$BaTiO_3$(001) interfaces", G. Radaelli, S. Brivio, C. Rinaldi and R. Bertacco. TYPE: POSTER.

- *X National Conference "Nano-phase materials"*, September 6-8 2011, Bologna, Italy. "Epitaxial Fe/MgO/Fe tunneling junctions on $BaTiO_3$(001)", G. Radaelli, S. Brivio, C. Rinaldi and R. Bertacco. TYPE: ORAL.

- *MAGNET 2011*, February 23-25 2011, Torino, Italy. "Epitaxial Fe/MgO/Fe tunneling junctions on $BaTiO_3$(001)", S. Brivio, G. Radaelli, C. Rinaldi and R. Bertacco. TYPE: POSTER.

Acknowledgements

First of all I would like to express my gratitude to my supervisor, Prof. Riccardo Bertacco for giving me the possibility to pursue the PhD. I appreciate his vast scientific knowledge and skills.

I owe sincere and earnest thankfulness to Prof. Josep Fontcuberta, who welcomed me in Institut de Ciència de Materials de Barcelona (ICMAB-CSIC) for my internship. His knowledge, enthusiasm, patient, and willingness to teach and discuss added considerably to my PhD experience.

I would also like to thank all the people involved in the scientific activities of my PhD: P. Torelli, B.R. Salles and G. Panaccione from APE beamline at ELETTRA synchrotron radiation source (Italy); S. Picozzi and E. Plekhanov from Università de L'Aquila (Italy); M. Varela from Oak Ridge National Laboratory (USA).

For the same reason I thank all the collegues of my research group, in particular D. Petti and M. Cantoni, and of Prof. J. Fontcuberta's group in ICMAB, in particular I. Fina and D. Gutierrez. A special acknowledgement also to D. Chrastina from Si-Ge group at LNESS; to M. Bianchi from Graphene group at LNESS, and to X. Marti from ICMAB.

Finally, thanks to Marco Leone, his technical support has been fundamental.

Thanks to Scuola Interpolitecnica for the financial support that gave me the possibility to carry out the scientific activities in different research facilities and to participate to the most important international conferences.

Un enorme grazie alla Pettiz, Eli, Mariolino, Stefanocarlocecchi e tutti i membri di LNESS, passati e presenti, per l'aiuto, il sostegno e tutti i momenti

divertenti passati insieme. In particolare, grazie a Edo, Fabio, Max e Jacopo per aver condiviso con me il percorso minato di burocrazia, scadenze e corsi del PhD ma anche la soddisfazione di essere arrivati fin qui.

Quiero agradecer a Diego y Mr David, la russa (Katy) y Jessica, Laurita, Maria, Jacke, Kumy y todos los amigos de Barcelona por la ayuda, fraternidad y el calor humano con el que me acogieron. Nunca me olvidaré de los meses passado hay y de la gente maravillosa que he conocido. Un gracias especial a mi grupo de chicas locas y al viejo gordo Roque que me hizo descubrir la maravilla de la ciudad de Barcelona.

Gazie a Nico, Vale, S8 e Ila per il supporto e la sincera amicizia che nonostante la distanza geografica ci tiene ancora tutti uniti. E grazie ai miei amici di sempre, per esserci sempre nonostante la mia vita un pò nomade e per la fiducia e la stima che mi dimostrano sempre.

Infine un grazie speciale alla mia famiglia che con il suo sostegno mi ha permesso di arrivare sino a qui.

Contents

Parte I

Introduction

Chapter 1

Introduction

1.1 Background & Motivation

Tunnel junctions consist of two metal electrodes separated by a very thin insulating (e.g., Al_2O_3 or MgO) or vacuum barrier [1]. Although forbidden by classical physics, an electron is allowed to cross a potential barrier that exceeds its kinetic energy. The electron therefore has a finite probability of being found on the opposite side of the barrier. Many useful electronic devices are based on this phenomenon. For example, tunneling between two superconductors separated by a thin insulating layer is employed in Josephson junctions, which have found important practical applications in superconducting quantum interference devices (SQUIDs), integrated circuits, and particle detectors. Electron tunneling lies at the heart of scanning tunneling microscopy (STM), which has become a conventional tool for studying the arrangement of individual atoms and molecules on surfaces.

Significant interest in electron tunneling has been triggered in the 1970s by the advent of spintronics, a technology aiming to use the electron spin in data storage and processing. Magnetic tunnel junctions (MTJs) [3] for magnetic memories and sensor applications are nowadays relevant technological achievements. The basis of these devices is that electron tunneling from a ferromagnetic metal electrode through a thin insulating barrier is spin-dependent [4]. This observation led to the idea of a MTJ: a tunnel

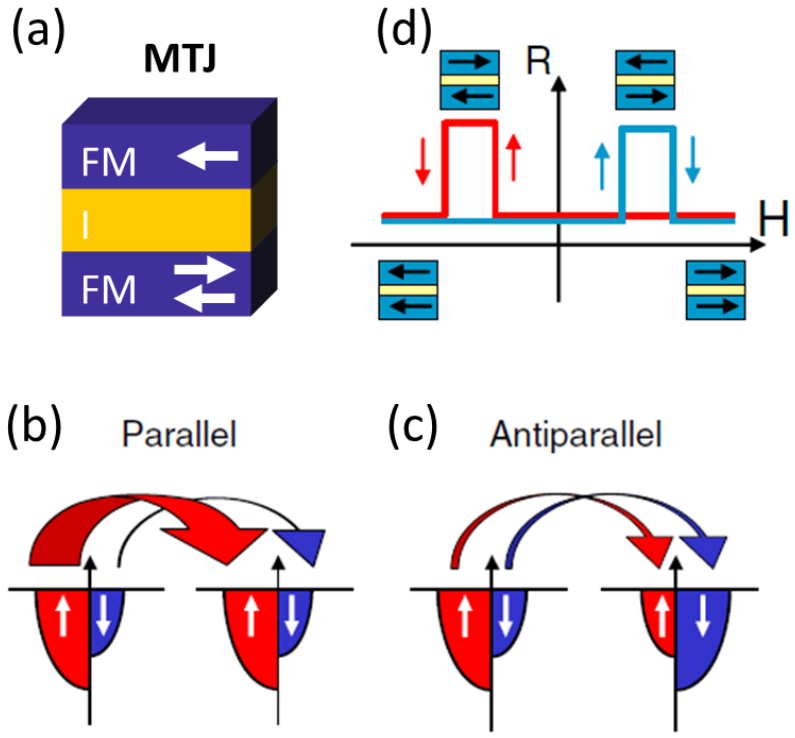

Figure 1.1.1: (a) Schematic view of a magnetic tunnel junction (MTJ). (b,c) Schematic description of the tunnel current in a MTJ with two identical, positively spin-polarized electrodes. In the parallel state (c), a strong current is carried by the spin-up channel, resulting in a large total current and a low resistance. In the antiparallel state (b), the current is rather weak in both spin channels, resulting in a weak total current and a high resistance. (d) Consequently, the junction resistance is expected to show two states as magnetic field is swept. Adapted from Bibes et al. [2].

junction with ferromagnetic metal electrodes. A schematic view of a MTJ is shown in Fig.1.1.1a. In the MTJ, the tunneling current depends on the relative orientation of the magnetizations of the two ferromagnetic electrodes, which can be changed by an applied magnetic field. This phenomenon is known as tunnel magnetoresistance (TMR) [5]. MTJs are thus characterized by two different and stable resistance states corresponding to parallel and anti-parallel magnetization orientation (Figure 1.1.1). The figure of merit of a MTJ is the relative change in resistance between these two states, known as the TMR ratio [3]:

$$TMR = \frac{R_{AP} - R_P}{R_P} = \frac{2P^1_{spin}P^2_{spin}}{1 - P^1_{spin}P^2_{spin}} \tag{1.1.1}$$

where P_{spin} is the spin polarization of the electrodes defined (in the simplest approach) as

$$P^i_{spin} = \frac{N_{i\uparrow} - N_{i\downarrow}}{N_{i\uparrow} + N_{i\downarrow}} \tag{1.1.2}$$

and $N_{i\uparrow(\downarrow)}$ is the density of states (DOS) of the *"i"* FM electrode at the Fermi level for majority spin electrons ($\uparrow$) (and minority spin electrons ($\downarrow$)). Since the first observation of large and reproducible TMR at room temperature [6], there has been an enormous increase of research in this field confirming the potential of MTJs for application in spin-electronic devices. Record TMR ratios are in the 1,000% range [7]. In terms of access time and endurance the characteristics of magnetic random access memories (MRAMs) based on MTJs equal or surpass those of alternative non-volatile memory technologies. However, they have a large handicap in the necessity of magnetic fields or large currents for the write operation. This implies high operating power and limited scaling.

The continuing quest for higher storage density, higher speeds, and lower power consumption drives vigorous exploration of new materials, physical principles and operation schemes that could be exploited in non-volatile memories. One of the key challenges is to develop a room temperature switch involving a significant bi-stable effect that can be controlled by an external electric field (E-field) stimulus and that can overcome scaling limitations of

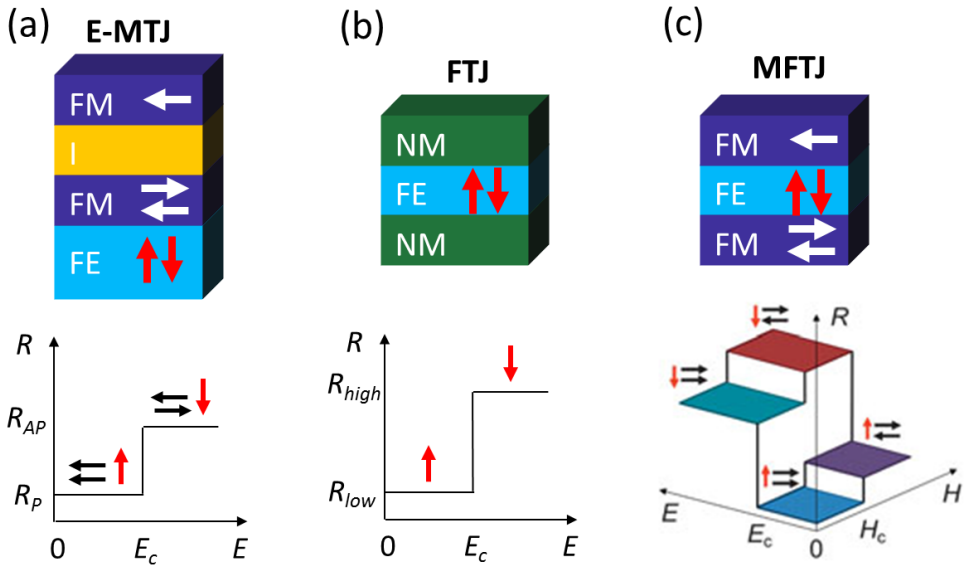

Figure 1.1.2: Schematic view of different types of E-field controlled memory/logic devices based on tunnel junctions: (a) E-field controlled MTJ (E-MTJ), (b) ferroelectric tunnel junction (FTJ) and (c) multiferroic tunnel junction (MFTJ). Ferromagnetic (FM), ferroelectric (FE), normal metal (NM), and insulating (I) layers are indicated where appropriate. Bottom panel show the resistance response of these junctions to magnetic (H) and electric (E) fields. Horizontal and vertical arrows indicate orientations of magnetization and electric polarization, respectively. Adapted from Tsymbal et al. [8].

conventional semiconductor technology based on charge storage. A dramatic improvement in materials fabrication techniques, especially thin film deposition, also played an important role in this search for new memory/logic devices. Recent advances on the nanoscale properties of ferroic materials, such as ferromagnets and ferroelectrics, and the coupling between several ferroic orders at the interfaces are offering much more versatile opportunities for next-generation nanoelectronics.

One of the most promising approach is the use of magnetoelectric coupling (MEC) to electrically control a MTJ. Magnetoelectric coupling is the coupling between magnetic and electric order. This coupling can be achieved at the interface between a ferroelectric (FE) layer and a ferromagnetic (FM)

one, thus allowing to control the magnetic properties of the FM layer by controlling the polarization of the FE one, and viceversa [9]. In a broad definition, magnetoelectric phenomena include not only the cross coupling between magnetic and electric order parameters but also involve related effects such as electrically controlled magneto-crystalline anisotropy, exchange bias, and spin transport. This offers a wealth of opportunity for information storage applications. In particular, it could provide the opportunity to use a write scheme based on the application of a voltage rather than large currents or magnetic fields in MRAMs, drastically reducing their operating power and removing the main hindrance in their miniaturization. The easiest geometry consists of an MTJ placed over a ferroelectric material. A schematic view of such an E-field controlled MTJ (E-MTJ) is shown in Fig.1.1.2b. Ferroelectrics possess a spontaneous electric polarization that can be switched by an applied E-field. Thus, application of an E-field to the ferroelectric may induce a change in the magnetization of the free FM layer, in contact with it, through interfacial magnetoelectric coupling. As a consequence, a change of the resistance of the MTJ can result thanks to the TMR effect, so that ultimately the resistance of the MTJ can be changed by the application of an E-field to the FE. Hence the described hybrid magnetoelectric device, proposed in 2009 by Pertsev at al. [10] even if in a slightly different geometry, may be employed as non volatile magnetic memory cell with nondestructive readout and electrical writing. In principle the ferroelectric could be placed also within the junction, acting as tunneling barrier sandwiched by the FM electrodes (Figure 1.1.2d). We will discuss this scheme at the end of the this section, but note that this is much more demanding in terms of the FE material, as it requires that a nanometer thick film displays good FE properties.

Another possibility is the ferroelectric tunnel junction (FTJ) [11] which consists of two metal electrodes separated by a nanometre-thick ferroelectric barrier that allows quantum-mechanical tunneling through it. A schematic view of FTJ is shown in Fig.1.1.2c. Polarization reversal in a FTJ leads to a change in resistance of the junction, a phenomenon known as the tunnel electroresistance (TER) effect. In FTJs the information is stored in the FE

polarization direction in the barrier, which is maintained in the absence of an electric field, thus providing the non-volatility. The write operation is obtained by application of an E-field able to switch the FE polarization of the tunnel barrier. Finally, as in the case of MTJs, information is read by measuring the tunneling resistance, which can be probed in a non-destructive way, thus overcoming the limitations of ferroelectric random access memories (FeRAMs) based on thick ferroelectric capacitors and opening the door for faster, denser and more energy-efficient RAMs [12, 13].

Functional properties of MTJs and FTJs can also be combined in a multiferroic tunnel junction (MFTJ). A schematic view of MFTJ is shown in Fig.1.1.2d. A MFTJ is a MTJ where a FE thin film acts as a tunneling barrier. Equivalently, MFTJ may be considered a particular kind of FTJ with FM metal electrodes. The key property of a MFTJ is the co-existence of the TMR and TER effects. Therefore, MFTJ represents a four-state device where resistance can be switched both by electric and magnetic fields. However, the interplay between FE and FM properties through interfacial magnetoelectric coupling makes these devices even more complex and promising. Switching of ferroelectric polarization in the barrier leads to a change in the resistance of the junction due to the sum of two contributions: the TER effect and the TMR effect driven by magnetoelectric coupling at the FE/FM interfaces In this sense a MFTJ can be considered an alternative geometry to E-MTJ (Fig.1.1.2b), as previously anticipated. Note that MFTJs on one side have to face all the problems related to nanometer thick ferroelectric films, but on the other side have the advantage of directly involving the FE/FM interface, where magnetoelectric coupling takes place, in the tunneling current path.

For reviews on E-MTJ, FTJ and MFTJ see [14, 8, 15, 9, 2].

1.2 The present thesis

1.2.1 Objectives

The goal of the present Thesis is to investigate memory/logic devices based on tunnel junctions which are characterized by (at least) two well defined

remanent resistance states that can be controlled by an external E-field. In particular, two different strategies have been used:

A) *E-field control of the remanent resistance states of a magnetic tunnel junction (MTJ) by using magnetoelectric coupling (MEC) effects at multiferroic (FE & FM) interfaces.*

B) *E-field control of the remanent resistance states of a tunnel junction with FE barrier (FTJ) displaying the TER effect.*

In this context, the main achievements of this Thesis are:

1. A deeper understanding of the physics of MEC at fully epitaxial Fe / $BaTiO_3$ (BTO) interfaces, as regards:
   (a) the chemical and structural properties of the Fe/BTO interface, as a function of the growth conditions;
   (b) the role of substrate clamping in strain mediated MEC in case of Fe films on BTO epitaxial layers;
   (c) the feasibility of the E-MTJ approach in case of fully epitaxial Fe/MgO/Fe/BTO tunneling junctions;
   (d) the origin of MEC in hybrid MTJs with BTO barrier and the demonstration of Giant MEC due to on-off switching of the magnetic order in the interfacial oxidized Fe layer.
2. The study and engineering of TER in FTJ devices:
   (a) fabrication of micron-sized FTJs with RT values up to 10^4%;
   (b) investigation of the effect of strain on the phase diagram of manganite thin films;
   (c) realization of FTJs integrating thin layers of half-doped manganites, aiming to exploit their E-field induced metal-insulator phase transition to enhance the TER.

1.2.2 Thesis structure & chapter description

Chapter 2 contains a detailed description of the physics and state of the art of magnetoelectric coupling mechanisms at FE/FM interfaces, in particular in the case of Fe/$BaTiO_3$(BTO) system, and of tunnel electroresistance effect in FTJs (section 2.1 and 2.2, respectively).

Chapter 3 contains a brief description of the experimental methods used in the contest of the present Thesis.

Chapter 4 describes the results of the study of magnetoelectric coupling at the interface between ferromagnetic Fe and ferroelectric $BaTiO_3$ films for the E-field control of the resistance of the MTJ in hybrid MTJ and FE heterostructures (E-MTJ). High-quality fully epitaxial Fe/$BaTiO_3$ bilayers are obtained. It is found that strain-mediated ME effects are suppressed in the case of epitaxial interfaces. Moreover no significant changes of the TMR are observed upon reversing the ferroelectric polarization of the $BaTiO_3$ in $Fe/MgO/Fe/BaTiO_3$ E-MTJs. These results give insight on the localized effect of the interface coupling in epitaxial $Fe/BaTiO_3$, which does not propagate from the bottom Fe/BTO interface to the top MgO/Fe one. In fact, we demonstrate that magnetic state of just the interfacial oxidized Fe layer in contact with $BaTiO_3$ can be dramatically changed upon reversing the ferroelectric polarization of $BaTiO_3$ at room temperature. Chapter 5 describes the results in the E-field control of tunnel resistance in FTJs. Extremely large, record TER values (above 10^4%) are obtained in large-area $Pt/BaTiO_3/La_{0.7}Sr_{0.3}MnO_3//SrTiO_3$(001) junctions. Moreover, aiming to develop barriers of adjustable width and thus further enhance the TER ratio, materials displaying E-field induced metal-insulator transition (half-doped manganites $La_{0.5}A_{0.5}MnO_3$, A = Ca/Sr) have been developed and integrated in epitaxial FE/half-doped manganite heterostructures. We have thus explored the strain role on half-doped manganites magnetic and transport properties, revealing a different sensitivity of the two manganites ($La_{0.5}A_{0.5}MnO_3$, A = Ca/Sr) to strain and E-field effects. Finally $Pt/La_{0.5}A_{0.5}MnO_3/BaTiO_3/La_{0.7}Sr_{0.3}MnO_3$ tunnel heterostructures have been grown and processed into devices for TER measurements. Preliminary

experiments performed at room temperature are presented.

Conclusions of the thesis are given at the end, in chapter 6.

Chapter 2

State of the art

2.1 Magnetoelectric coupling in Multiferroic (FE & FM) heterostructures

Multiferroics are materials in which two or more ferroic orders exist [16]. Among them, the most technologically appealing are those showing ferromagnetism (FM) and ferroelectricity (FE). But the coexistence of these two ferroic orders is not enough: even more relevant is the existence of a strong coupling interaction between them, the so called magnetoelectric coupling (MEC). In the presence of MEC, it is possible to control the magnetic properties by electric fields [17] and viceversa [18] (Figure 2.1.1). Magnetoelectric materials have recently emerged as a promising route to achieve electrical writing of magnetic information in spintronic devices. In fact, MEC could permit to build up a new generation of memory devices, as it would exploit the best aspects of ferroelectricity (low cost electric writing) and magnetism (robustness and durability of the stored information). In spite of recent progress in spin-torque [19], electric-field-assisted switching [20] or coherent magnetization switching [21], magnetoelectric coupling represents an advantageous route towards low-power electrical control, especially if reversible electric writing of the magnetic information, without need of auxiliary magnetic fields, could be achieved.

The development of multiferroics and magnetoelectric materials started

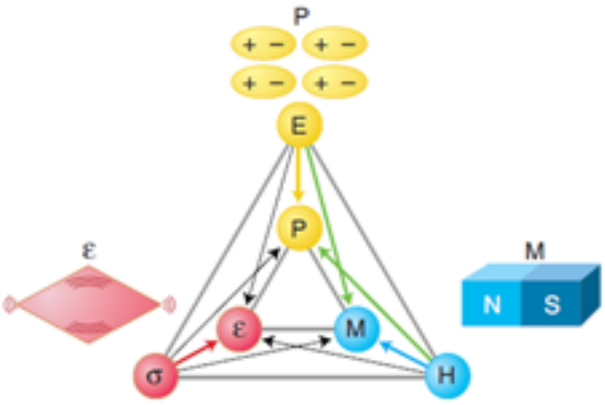

Figure 2.1.1: From Spaldin and Fiebig [22]. The electric field E, magnetic field H, and stress σ control the electric polarization P, magnetization M, and strain ε, respectively. In a ferroic material, P, M, or ε are spontaneously formed to produce ferromagnetism, ferroelectricity, or ferroelasticity, respectively. In a multiferroic, the coexistence of at least two ferroic forms of ordering leads to additional interactions. In a magnetoelectric multiferroic, a magnetic field may control P or an electric field may control M (green arrows).

in Russia in the late 1950s and continued intensively in the 1960s (see [23] for a review). However, the fact that large enough magnetoelectric effects were not found together with the lack of compounds that display such effects and the difficulties of growing them, resulted in decreasing interest on magnetoelectric coupling phenomenon. The revival of magnetoelectric materials started at the beginning of 00's decade. A representative paper of this renascence is "Why Are There so Few Magnetic Ferroelectrics?" by N. Hill [24], which shows that the usual atomic-level mechanisms driving ferromagnetism and ferroelectricity are mutually exclusive, because they require empty and partially filled transition metal orbitals, respectively. This recognition, at the same time both intriguing and stimulating for the nascent community investigating multiferroics, combined with advances in thin film growth techniques and the urgent necessity of novel multifunctional materials for next generation electronic devices, has generated a flurry of research activity on magnetoelectric multiferroics, so much that the field has grown exponentially since then.

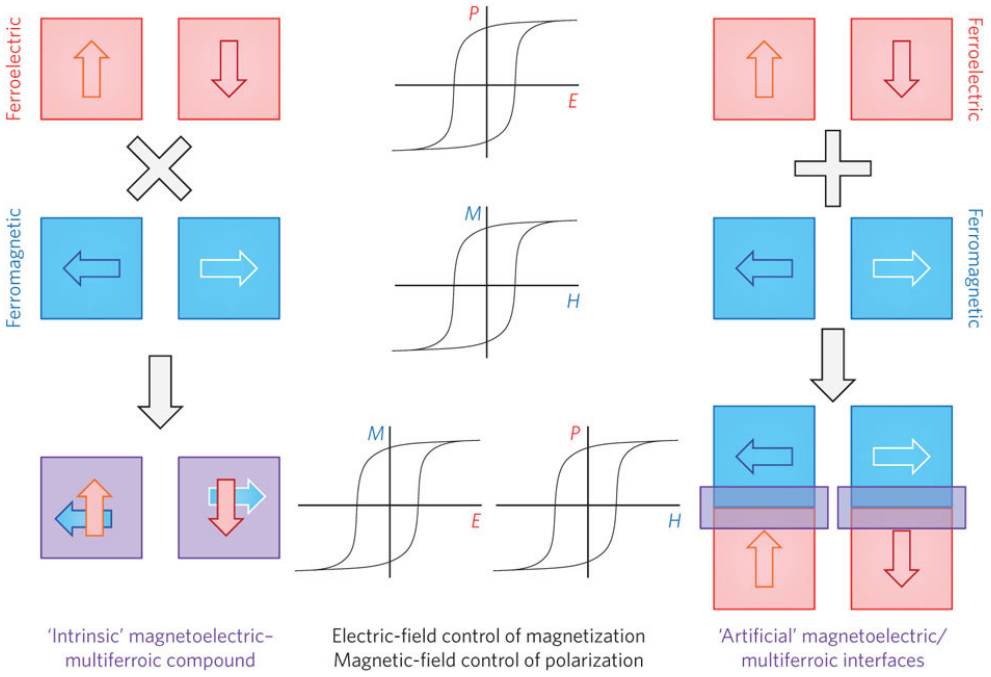

Figure 2.1.2: Reported from Bibes [14]. Schematic representation of an 'intrinsic' (that is, single phase) multiferroic compound (left) and an 'artificial' multiferroic interface (right). In both systems, ferromagnetic and ferroelectric orders may coexist and influence each other through a magnetoelectric coupling.

Despite this, a single-phase material showing a sizable coupling between ferromagnetism and ferroelectricity at room-temperature is still missing, thus hampering or limiting practical applications [25]. Aiming at a large technological impact, "artificial" multiferroic/magnetoelectric heterostructures, combining traditional ferroelectrics and conventional ferromagnetic materials with high Curie temperatures, seem much more promising. In fact, room temperature interfacial multiferroics can be designed, circumventing the lingering scarcity of single-phase room-temperature multiferroics. In these artificial systems it's possible to control the magnetic properties of the ferromagnetic layer by controlling the polarization of the ferroelectric one, and viceversa, exploiting magnetoelectric coupling mechanisms at the FM/FE interface, as shown in Fig. 2.1.2 (for reviews see [14, 9, 15]).

Among many FM/FE heterostructures, $Fe/BaTiO_3$ (BTO) has emerged

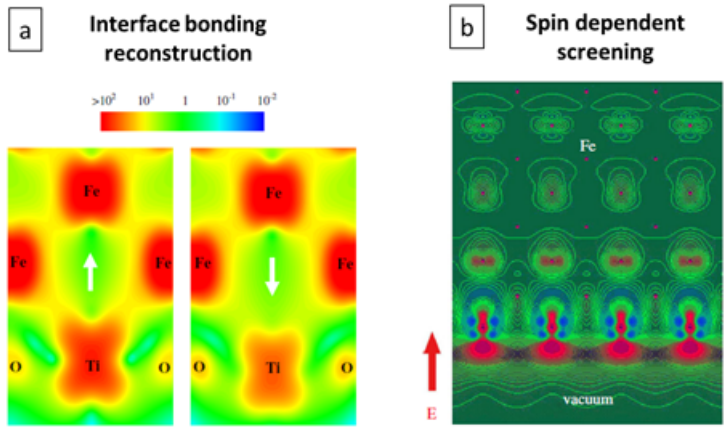

Figure 2.1.3: Direct coupling mechanisms. (a) Minority-spin charge density (in arbitrary units) at the Fe/BTO interface for two opposite polarization in BTO: net polarization pointing up (left panel) and down (right panel). From Duan et al. [26]. (b) Induced spin density on the Fe (001) surface owing to an applied electric field. From Velev et al. [9] adapted from Duan et al. [27].

as a prototypical system. These materials possess robust ferroic orders at room temperature and a negligible lattice mismatch (∼1.4%) which favors epitaxial growth of Fe/BTO interfaces. At the time when this thesis started, these factors, combined with the extreme simplicity of this system and the stimulating theoretical prediction of undisclosed electronically-driven interface magnetoelectric effects for this system, determined our decision to focus attention on Fe/BTO interface.

Two kinds of ME coupling have been predicted at Fe/BTO interface: (1) direct coupling, owing to interfacial electronic effects, and (2) indirect coupling, mediated by strain.

1. ***Direct coupling*** mechanisms, leading to changes in the Fe surface magnetization and surface magneto-crystalline anisotropy, have been theoretically predicted based on bond-reconfiguration driven by ionic displacement or spin dependent screening mechanisms:

   (a) *Interface bonding reconstruction:* It was predicted that displacements of atoms at the FM/FE interface caused by ferroelectric

instability alter the overlap between atomic orbitals at the interface which affects the interface magnetization. In particular, it has been proposed that interface cation displacements on BTO (see Fig. 2.1.3a) could give rise to a tiny variation of the Fe interfacial magnetic moment ($\sim 10\%$), both for sharp [26] and oxidized interfaces [28, 29], and/or to a sizable change in the surface magneto-crystalline anisotropy (MCA) energy of the Fe film [30]. This reflects in modifications of the spin polarization as well [26].

(b) *Spin dependent screening*: Another electronic mechanism for an interface magnetoelectric effect originates from spin-dependent screening [31, 27, 32]. In this case, the screening of the polarization charges appearing at the FE surface by majority and minority electrons, displaying different screening lengths, results in a change in the interface magnetization (see Fig. 2.1.3b).

2. ***Indirect (Strain-mediated) coupling*** arises from an elastic coupling between ferromagnetic and ferroelectric materials, when the materials are magnetostrictive and piezoelectric. In the case of Fe/BTO, an applied electric field to the BTO, which is also piezoelectric, induces a deformation of its unit cells which is mechanically transferred as strain to the magnetic Fe layer. Large magnetic anisotropy and coercitivity changes in the Fe layer are expected due to inverse magnetostriction. The effect is thus indirect since the coupling is the product of two distinct interaction: the applied E-field is translated into stress and strain is then converted into a change in magnetic properties of the Fe layer.

Experimentally, at the time when this thesis started it had already been clearly demonstrated that for Fe thin films deposited on BTO substrates the magnetoelectric coupling is dominated by the indirect strain-mediated mechanism [34, 33]. Large modifications of magnetic anisotropies and magnetic coercitivity in the Fe layer have been reported in response to application of electric fields to the BTO crystal. To go more in details, in Fig. 2.1.4 we

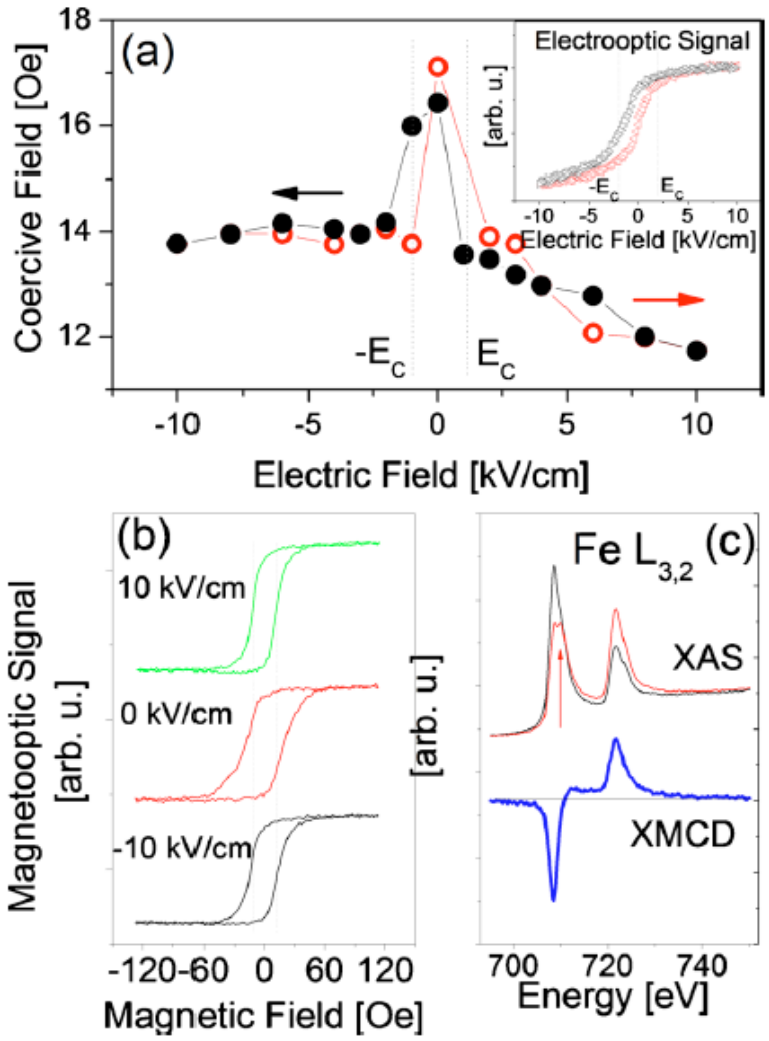

Figure 2.1.4: Reported from Brivio et al. [33]. (a) Coercitive field of an 8 nm thick Fe film as a function of the electric field applied to the BTO substrate and, in the inset, the ferroelectric hysteresis loop recorded as an electro-optical signal. (b) Ferromagnetic hysteresis loop at different BTO bias conditions indicating the evolution of the coercitive field. (c) Fe $L_{2,3}$ edge and XMCD of a 3 nm Fe thick film.

report results of magnetoelectric measurements performed by our group (S. Brivio et al. [33]) at room temperature on 2-8 nm thick Fe films epitaxially grown by Molecular Beam Epitaxy (MBE) on a BTO(001) crystal, using magneto-optical Kerr effect (MOKE) and X-ray magnetic circular dichroism (XMCD) techniques. Unpoled BTO substrates are a mixture of domains with polarization pointing out of plane (c-domains) and in plane (a-domains). Therefore the ferroelectric hysteresis loop can be viewed as the result of the expansion retraction of c-domains oriented in the direction of the external field (perpendicular to the interface) at the expense of a-domains, the latter reappearing when the electric field is removed. The authors, in Ref. [33], show that the magnetic coercitive field (H_C) of Fe as a function of the applied electric field to the BTO presents a maximum in the remanent state of BTO and drops symmetrically for E-fields above the ferroelectric coercitive field E_C (Fig. 2.1.4a). The drop of H_C is strictly related to the alignment of mixture of FE domains along the direction of the electric field. Expansion of c-domains at the expense of a-domains for $|E| > |E_C|$ induces a local strain in the Fe epitaxial film $\varepsilon = (c_{BTO} - a_{BTO})/a_{BTO} = 0.0125$, and finally harden the magnetic transition via the creation of stronger pinning sites for the magnetic domain-wall motion. On the contrary, no relevant influence of the electric field applied to the BTO was found on Fe magnetic anisotropies, at room temperature, (Fig. 2.1.4b) or on the Fe magnetization. Changes in the MOKE loops amplitude (Fig. 2.1.4b) are in fact essentially due to the electro-optic effect originating from the switch of the dielectric polarization of BTO, shown in inset of Fig. 2.1.4a, as confirmed by XMCD experiments (Fig. 2.1.4c). This was the state of the art at the time when this thesis started.

Despite the promising results obtained for Fe films on BTO substrates, fully epitaxial Fe overlayers on BTO films grown on other substrates are definitely more interesting in view of integration in devices. In this case mechanical clamping from the substrate, and the absence of the mixture of domains which characterized the BTO crystals, could largely suppress the strain-mediated magnetoelectric coupling [36, 37], but at the beginning of this thesis a clear experimental assessment of the impact of this clamping

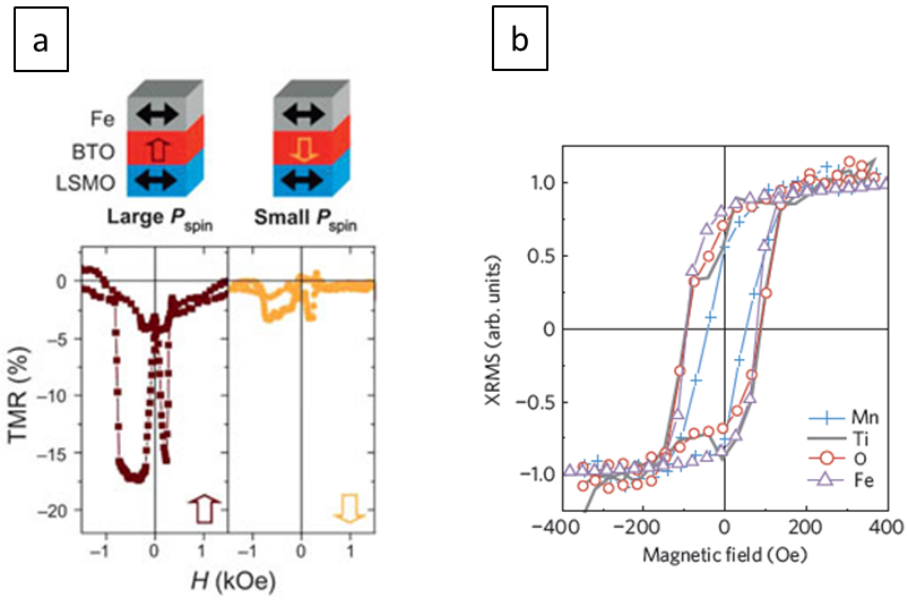

Figure 2.1.5: Fe/BTO/LSMO multiferroic junctions. (a) Adapted from Garcia et al. [35]. TMR curves after poling the BTO (1 nm) ferroelectric tunnel barrier up or down. A clear modulation of the TMR with the FE polarization orientation is seen. (b) Reported from Valencia et al. [29]. XRMS versus H for Mn, Fe, Ti and O for the Fe/BTO/LSMO heterostructure.

effect did not exist.

On the other hand, recent experimental reports suggest the presence of pure electronic interfacial MEC mechanisms in these systems. Garcia et al. [35] fabricated artificial multiferroic tunnel junction based on Fe/BTO(1 nm)/$La_{2/3}Sr_{1/3}MnO_3$ (LSMO). At 4 K, they observed large negative TMR, reflecting a negative spin polarization for the Fe/BTO interface. By applying short voltage pulses of ± 1 V, they observed reversible changes of the tunnel resistance linked to the variation of the ferroelectric polarization direction, with a TER of about 30%. More interestingly, the TMR was found to strongly depend on the direction of the ferroelectric polarization. As can be seen for a typical junction in Figure 2.1.5a, the TMR measured at an applied bias voltage of –50 mV varies from a high value (-17%) to a low value (-3%) when the electrical polarization points toward Fe or LSMO, respectively. Supposing that the half-metallic LSMO/BTO spin-polarization is poorly sensitive to the ferroelectric polarization direction, this suggests a modification of the Fe/BTO interfacial spin polarization by the ferroelectric polarization. The observed change in TMR is consistent with the predicted change of the spin polarization at the Fe/BTO interface [26] and with the even more recent experimental evidence of remanent induced magnetic moments on Ti and O atoms coupled with those of Fe (Figure 2.1.5b) observed in analogous Fe/BTO/LSMO MFTJs by means of X-ray resonant magnetic scattering measurements (XRMS) [29]. Despite these pioneering and brilliant results suggest the potential of magnetoelectric coupling at Fe/BTO interfaces for application in electrically controlled magnetic memory devices, so far a clear direct experimental demonstration of the MEC mechanisms dominating at fully epitaxial interface does not exist.

We strongly emphasize that a clear understanding of the mechanisms governing the coupling of magnetic and ferroelectric orders at the Fe/BTO interface is of fundamental scientific interest and should be valuable in view of the engineering of multiferroic (FM & FE) heterostructures for application in electrically controlled spintronic devices.

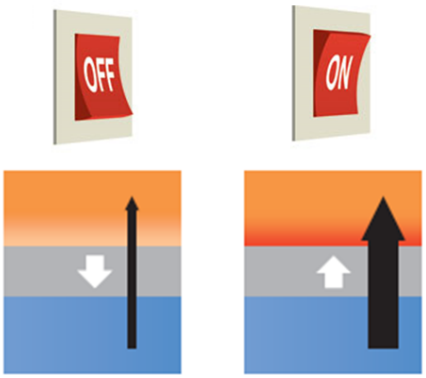

Figure 2.2.1: Adapted from Bibes [14]. Control of electronic transport by ferroelectricity in FTJ. The direction of polarization in the ferroelectric (white arrows) influences the charge current (black arrow).

2.2 Electroresistance in FE tunnel junctions

A ferroelectric tunnel junction (FTJ) consists of two electrodes separated by a nanometre-thick ferroelectric (FE) barrier that allows quantum-mechanical tunneling through it. The key property of an FTJ is tunneling electroresistance (TER), which is the change in resistance of an FTJ upon reversal of FE polarization of the barrier (Figure 2.2.1).

Esaki originally proposed the concept of a polar switch involving a switchable thin-film ferroelectric material in 1971 [38]. However, at that time, there were no experimental techniques and capabilities to fabricate thin-film ferroelectrics acting as a tunneling barrier. Moreover, it was believed that the critical thickness for ferroelectricity in thin films was much higher than the thickness necessary for tunneling to take place. The discovery of ferroelectricity in nanometer-thick films [39, 40, 41] opened up exciting prospects for FTJs.

The concept of a FTJ is illustrated in Fig. 2.2.2a, which shows the simplified band structure of a tunnel junction with a ferroelectric barrier. In a tunnel junction, the current is given by the integral of the product of the density of states (DOS) of the electrode/barrier interfaces at each kinetic energy, weighted by the occupancy probability, and of the tunneling transmission, that is an exponential function of the energy-barrier thickness and height.

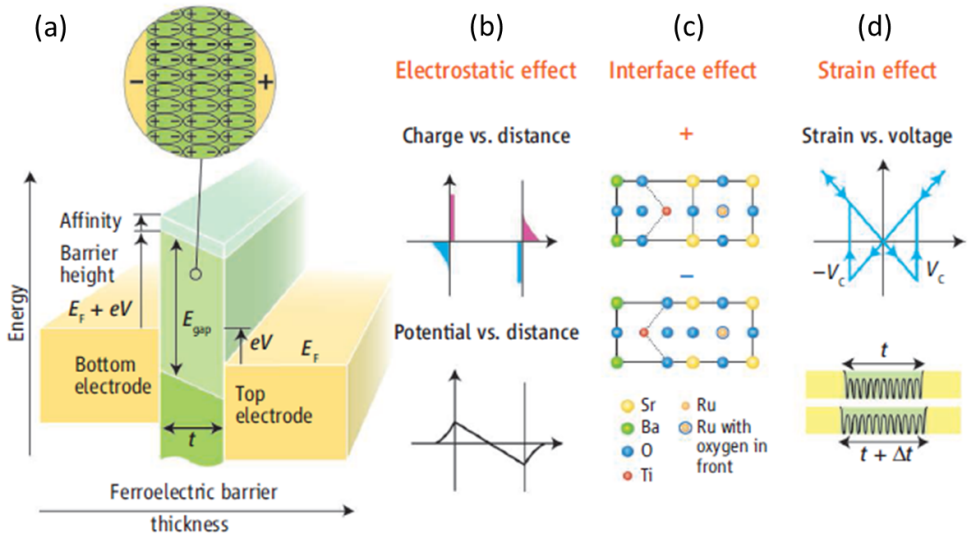

Figure 2.2.2: From Tsymbal and Kohlstedt [11]. (a) Schematic diagram of a tunnel junction, which consists of two electrodes separated by a nanometer-thick ferroelectric barrier layer. (E_{gap} is the energy gap, E_F is the Fermi energy, V is the applied voltage, V_C is the coercitive voltage, t is the barrier thickness, and $\triangle t$ is the thickness variation under an applied field). (b), (c) and (d) Mechanisms affecting tunneling in FTJs: electrostatic potential at the interface, interface bonding and strain effect, respectively.

In FTJs all these parameters can depend on the ferroelectric polarization direction, which results in a resistance switching associated with polarization reversal. The figure of merit of a FTJ is the relative change in resistance between these two states, known as the TER ratio:

$$TER = \frac{R_{OFF} - R_{ON}}{R_{ON}} \tag{2.2.1}$$

The origin of TER effect is illustrated in Figure 2.2.2b-d. Polarization affects the tunneling current by changing (1) the electrostatic potential at the interface, (2) interface bonding strength, and/or (3) strain associated with piezoelectric response [11].

1. The *electrostatic effect* results from the change of the electrostatic potential profile induced by the reversal of the electric polarization P in the ferroelectric. Indeed, if the ferroelectric film is sufficiently thin but

still maintains its ferroelectric properties, the surface charges in the ferroelectric are only partially compensated by the electrodes, depending on the Thomas-Fermi screening lengths of the metals and therefore the depolarizing electric field E in the ferroelectric is not zero [42]. This induces an asymmetric variation of the electrostatic potential across the tunnel barrier (see Fig. 2.2.2b). When the ferroelectric is connected by two different electrodes, the screening and hence the electrostatic variation are different at the interfaces. This can be described as a shift of the average barrier height when the ferroelectric polarization is flipped [43, 44].

2. The *interface effect* on TER follows from atomistic calculations [45]. The polarization switching alters positions of ions in the last atomic layer in the ferroelectric, that influence the atomic orbital hybridization at the interface and hence the interfacial DOS as well as the transmission probability (see Fig. 2.2.2c).

3. Finally, the piezoelectricity of a ferroelectric barrier under an applied voltage produces a *strain* (see Fig. 2.2.2d) that changes transport characteristics of the barrier such as the barrier thickness [44] and the attenuation constant [45].

We note that in FTJs with magnetic electrodes, in addition to the three mechanisms mentioned previously, an important contribution to the TER may arise from the interface magnetoelectric effect. An interesting prediction was made recently for the $La_{1-x}A_xMnO_3/BaTiO_3(001)$ interface, where A is a divalent cation [46]. First-principles calculations showed a possibility to switch a magnetic order at the interface, from ferromagnetic (FM) to anti-ferromagnetic (AFM), by reversing the polarization of the ferroelectric $BaTiO_3$ (BTO). In a FTJ with such a magnetoelectrically active interface in the path of the tunneling current, switching of the ferroelectric barrier is expected to change the tunneling barrier thickness, thus leading to a giant change in conductance (enhanced TER) [47].

Experimentally, since many oxides exhibit resistive switching behavior [48], the key problem to demonstrate that the electroresistance is controlled

by the FE state, was measuring both resistance and FE properties of the barrier. As FE switching in tunnel junctions is hindered by the tunneling current through the junction itself when the poling pulse is applied, scanning probe microscopy (SPM) techniques have been employed. These techniques allow the application of an electric field within nanometer resolution while simultaneously probing the polarization by piezoresponse force microscopy (PFM) [49] and the tunneling current by conducting atomic force microscopy (C-AFM). Moreover, SPM measurements can be done in two geometries: (i) with the conductive tip used as a top electrode in contact with the surface of the ferroelectric layer or (ii) with the tip contacting a deposited top electrode.

A first prototype FTJ has been demonstrated only in 2009 when three experimental groups independently reported experimental observations of the TER effect associated with the switching of ferroelectric polarization of BTO, $PbTiO_3$ (PTO), and $Pb(Zr,Ti)O_3$ (PZT) films thanks to the use of SPM techniques in geometry (i) [50, 51, 52, 53]. As en explicative example we report the main results obtained by Garcia et al. [50] for $BaTiO_3$/ $La_{0.67}Sr_{0.33}MnO_3$/ $NdGaO_3$(001) samples. Figure 2.2.3 illustrates the room temperature correlation between the ferroelectric polarization orientations of BTO films of different thicknesses, as is indicated by a different PFM contrast in Figure 2.2.3a-c, and the tunneling conductance across these films measured by C-AFM (Figure 2.2.3d-f). The resistance grows exponentially with the film thickness, indicating a tunneling transport regime (Figure 2.2.3j). TER also increases exponentially and reaches very large values up to 75,000% (Figure 2.2.3k), in agreement with theoretical predictions [43]. These experimental results, as the ones provided in the same period by the other groups [52, 53, 51], prove the concept of FTJ and show the capability of FE thin films to serve as a nanoscale material that can act as a switch to store binary information. This was the state of the art at the time when this thesis started.

Probing the TER effect through the top electrode emulates real device geometry, and for this reason is of more practical importance. Polarization stability of ultra thin ferroelectric barriers in this case becomes a serious issue. In the last two years different groups have fabricated FTJs with

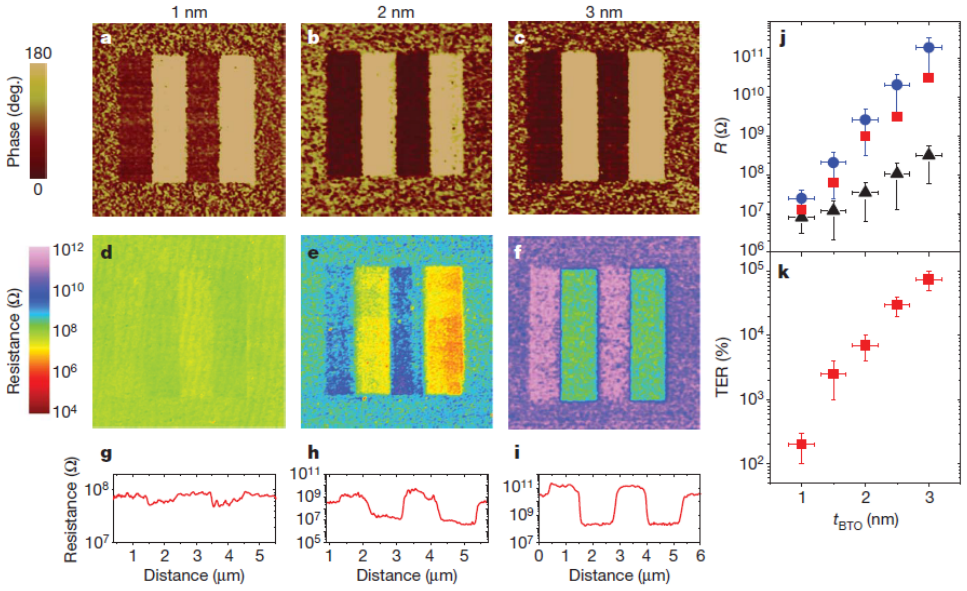

Figure 2.2.3: Reported from Garcia et al. [50]. Observation of the giant tunneling electroresistance (TER) effect in ultra-thin strained BTO films. PFM phase image (a-c) and C-AFM resistance mapping (d-f) of four written ferroelectric stripes (1 x 4 μm^2) for BTO films with a thickness of 1, 2, and 3 nm. (g-i) Corresponding resistance profiles of the poled area. (j) Thickness dependence of resistance (R) of unpoled (red squares), and positively (black triangles) and negatively (blue circles) poled regions. An exponential increase in R and TER (k) with BTO thickness is seen, as expected for direct tunneling.

top nano-electrodes using BTO, PZT and $BiFeO_3$(BFO) barriers and have demonstrated, by using SPM techniques in geometry (ii), that also in these devices it's possible to achieve giant room temperature TER effect. In particular, repetitive switching between two distinct resistance values (giant TER ratio up to 100,000%), good data retention for up to 10 yr and the memory programming with short (10 ns) voltage pulses, just few volts in amplitude have been reported [54, 55, 56]. These results reveal the significant potential utility of FTJs in nonvolatile memory applications with the advantages of non-destructive readout, simple device architecture, low power consumption, and high density data storage. Some authors also show that changes in resistance scale with the nucleation and growth of ferroelectric domains in the ultra-thin barrier layer, thereby suggesting potential as multilevel memory cells and memristors [57, 58].

An additional complication stems from increased leakage currents due to local defects in FTJs with a relatively large electrode area. It is well known that defects are present in ferroelectric thin films. These defects may also exist in ultra-thin ferroelectrics and, as a result, deteriorate resistance switching properties of FTJs. This problem is more evident in large area devices, where the probability to find defects in the barrier is higher. Recently, successful demonstration of room-temperature resistive switching in junctions with TER ratio of $\sim 10^3\%$ and lateral dimensions in the range of $10^3 \mu m^2$ have been reported [59, 60]. TER ratios, at room temperature, reported so far for FTJs have been collected in Figure 2.2.4. Data are grouped in: TER measured using SPM tip as top electrode (geometry (i)), TER measured using SPM tip to contact the top electrode (geometry (ii)) of the nanojunction, and TER measured using a probe station connected to the electrodes of the microjunction. From the graph is evident that TER ratios measured in microjunctions are lower than in nanojunctions.

Interestingly some very recent results [61, 62, 63] have suggested that by appropriately engineering the interfaces of FTJs it's possible to achieve a change in the barrier thickness by switching the ferroelectric polarization of the barrier layer, thus leading to enhanced TER effect. Record TER ratios up to $10^5 - 10^6\%$ at room-temperature have been achieved in BTO-based micro-

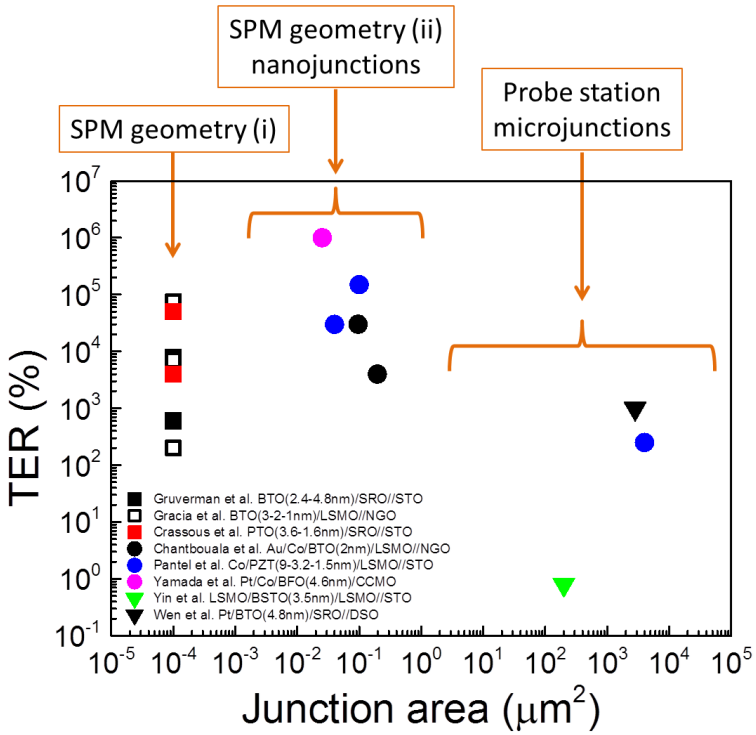

Figure 2.2.4: Room temperature TER ratios measured by SPM geometry (i) [52, 53, 50], SPM geometry (ii) [58, 56, 55, 54, 57], and probe station [64, 65, 60] as a function of electrodes area. For measurements performed using SPM tip as top electrode (geometry (i)), an approximate contact area of 100 nm^2 has been considered.

junctions [61, 63]. Nevertheless, the complex physical mechanisms playing a role in these junctions still ask for a deeper investigation.

Part II

Experimental methods

Chapter 3

Experimental techniques

This chapter is devoted to the description of the experimental techniques used in the present thesis. Firstly, the thin film growth equipments are described (section 3.1). Afterward, the devices design and lithographic process are described (section 3.2). Finally, the complementary investigation methods and techniques used throughout this thesis are presented: structural, morphological and chemical characterization techniques in section 3.3, dielectric and ferroelectric characterization techniques in section 3.4, transport measurements set up in section 3.5 and magnetic characterization techniques in section 3.6, respectively.

3.1 Growth techniques

The first section of this chapter is dedicated to the description of the experimental techniques used for thin films growth. $Fe/BaTiO_3$-based samples used to achieve objective 1 of the thesis (shedding light on the physics of MEC at fully epitaxial multiferroic interfaces (FE/FM) and fabricating possible hybrid MTJ and FE (E-MTJ) devices integrating multiferroic interfaces) have been prepared in L-NESS center with an UHV multichamber system (LASSE) [66], which allows the combined growth by Pulsed Laser Deposition (PLD) and Molecular Beam Epitaxy (MBE) as well as the use of many different in situ characterization techniques. Figure 3.0.1 shows a schematic view

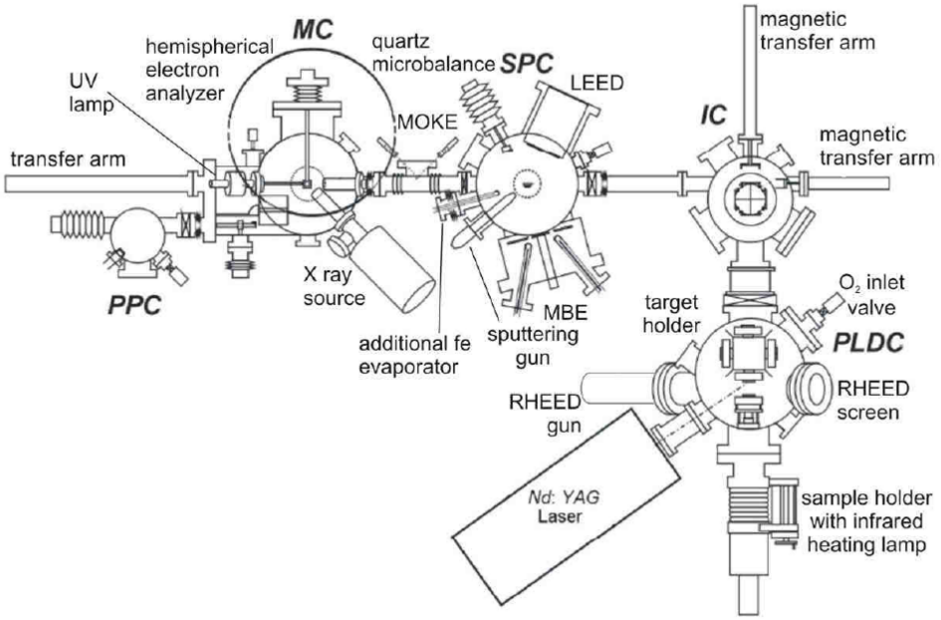

Figure 3.0.1: Schematic illustration of the multichamber LASSE system (top view) [66] located at L-NESS center. High and ultra-high vacuum chambers are interconnected by gauge valves and samples can be moved from one chamber to the others by means of magnetic transfer arms.

of the complete system, consisting of several vacuum chambers connected by gate valves. The Introduction Chamber (IC) serves as fast entry lock and as connection between the Pulsed Laser Deposition Chamber (PLDC) and the ultra high vacuum (UHV) chambers: the Sample Preparation Chamber (SPC) and the Measurements Chamber (MC). The SPC is devoted to: sample preparation via sputtering and annealing treatments; growth of thin films by means of a MBE system; first characterization of the surface quality by means of Low Energy Electron Diffraction (LEED). The MC is devoted to electron spectroscopies, while the Photocatode Preparation Chamber (PPC) is dedicated to the preparation of the polarized electrons source for Inverse Photoemission Spectroscopy.

$La_{0.5}A_{0.5}MnO_3/BaTiO_3$-based samples (A = Sr/Ca) used to achieve objective 2 of the thesis (fabricating room temperature FTJ devices and engineering the interfaces of these devices to try to enhance TER ratio) have been prepared by PLD at ICMAB.

3.1.1 Pulsed laser deposition

$BaTiO_3$ and $La_{0.67}Sr_{0.33}MnO_3$ thin films were deposited at L-NESS by pulsed laser deposition (PLD) in a multichamber system (LASSE) equipped also with molecular beam epitaxy system and different in situ characterization techniques. The technical support of M. Leone is acknowledged. $BaTiO_3$, $La_{0.67}Sr_{0.33}MnO_3$, $La_{0.5}Sr_{0.5}MnO_3$ and $La_{0.5}Ca_{0.5}MnO_3$ thin films were deposited by PLD by N. Dix in the facility of ICMAB.

Figure 3.1.1 shows a schematic diagram of a laser ablation system with the main components including the laser beam source, a spinning target stage and a heatable substrate stage. As a matter of fact, the most important aspect of PLD is the possibility of obtaining the correct stoichiometry also in very complex compounds. This is the advantage that still promotes the widespread use of this technique. PLD is based on vaporization induced by pulsed laser ablation of a target surface, giving rise to the formation of a plasma (the characteristic plume) which in turns deposits onto a suitable substrate. Many are the deposition parameters to be taken into account.

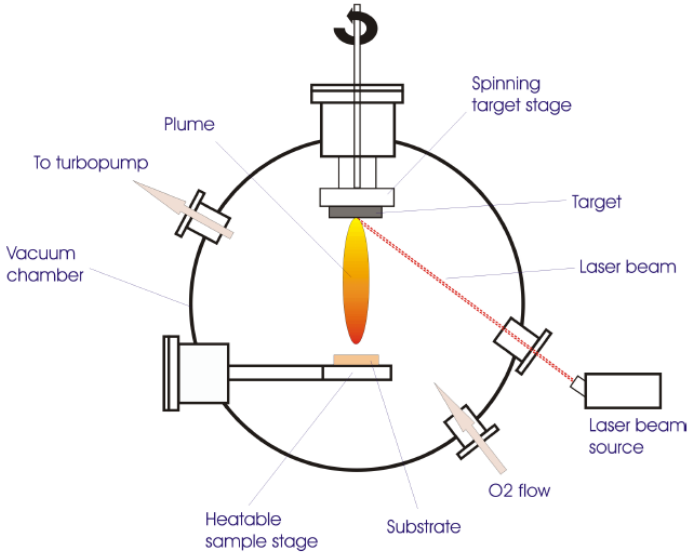

Figure 3.1.1: Schematic of a pulsed laser deposition system.

This makes PLD a very complex but also very versatile technique. The laser can be adjusted in energy, fluence, focalization and repetition rate of its pulses. All these parameters strongly affect the ablation process and the transport of the material, too. The material transport in the plume significantly depends also on the oxygen pressure in the deposition chamber, while the condensation process is regulated mainly by the temperature of the substrate, but it's also influenced by the kinetic energy of the species arriving at the surface.

The set up of the PLD system used in L-NESS is illustrated in Figure 3.0.1. From the introduction chamber (IC, which can be vented and pumped down to $1 \cdot 10^{-7}$ torr within 20 minutes) samples can be moved to the pulsed laser deposition chamber (PLDC, p_{base}=$1 \cdot 10^{-8}$ torr), equipped with PLD system and reflection high energy electron diffraction (RHEED), with a magnetic transfer-harm. The manipulator maintains the substrate in vertical position in front of the target, hold up by a motorized carousel. Up to four targets can be constantly lodged inside the chamber and selected in any time during the deposition process. The manipulator allows a manual regulation of the target-substrate distance, fundamental parameter of depo-

sition process. Behind the manipulator is placed an homemade water cooled infrared lamp (400 W) lodged in an Al coated reflector, capable of working in every pressure condition up to 800°C. Temperature is controlled by a pirometer *Marathon Series* ($\lambda = 1.6\mu m$). A step-by-step motor system, controlled by a PC, implements the following movements:

- substrate rotation around z axis (deposition axis), to guarantee good thickness uniformity of the deposited film;
- vertical translation of the carousel and rotation of the target around z axis, to guarantee good uniformity of target erosion;
- carousel rotation around vertical axis to select the target.

During deposition oxygen gas is fluxed in the chamber to help obtaining the correct stoichiometry in the deposited film. The flux of gas can be adjusted in entrance by a flow meter and, in exit, by a valve which opens a high impedance conduit towards a turbomolecular pump, so that the pressure on the pump doesn't reach 10^{-4} torr even when pressure in the chamber is around 0.1 torr.

A re-fused quartz window allows the transmission of the laser beam inside the chamber. The laser system, working in *Q-switching* regime [67], is a *Continuum Powerlight^{TM} Precision II 8000*. The active material of the rod and of the amplificator external to the cavity, Nd-YAG, is pumped by flash lamps. Four frequencies are available: natural of Nd (1064 nm), doubled (533 nm), tripled (533 nm) and quadrupled (266 nm). In this Thesis we have always used a wavelength of 266 nm and a repetition frequency of 2 Hz.

The chamber is also equipped with a RHEED apparatus, *STAIB RH 50^{TM}*. The electron beam, with energy adjustable between 30 keV and 50 keV, impinges the sample at grazing angle adjustable within ±7°. The sample can be rotated, round its surface normal, to reach glancing diffraction conditions along different crystallographic axis. The diffraction figure is collected on a fluorescent screen and recorded by a CCD camera for software aided dynamic analysis and manipulation. Differential pumping of the electron gun and the high mean free path of high energy electrons permit to work

in both UHV and poor vacuum (typically of the order of 0.1 torr during the deposition of oxide films), maintaining a small focus spot ($< 100\ \mu m$) and an extremely small beam divergence (< 2 mrad), under proper deflection and focusing conditions. The distance between electron gun, sample and fluorescent screen is big enough to allow the in situ use of RHEED for evaluating in real time the epitaxy of films grown by PLD.

3.1.2 Molecular beam epitaxy

Fe, Co, Au and MgO thin films were deposited in L-NESS by molecular beam epitaxy (MBE).

The set up is illustrated in Figure 3.0.1. Samples can be moved from introduction chamber (IC) to the sample preparation chamber (SPC, $p_{base}=1 \cdot 10^{-10}$torr). This is an UHV-based technique for producing high quality epitaxial structures with monolayer control. MBE is based on the thermal evaporation of atoms, achieved by heating up a solid source in a Knudsen cell. The beam of atoms freely propagating in UHV environment impinges on the substrate surface, where atoms can diffuse and eventually be incorporated into the growing film. The chamber has a cylindrical shape with vertical axis and internal diameter of 300 mm. The manipulator is inserted from above and can heat up the sample by Joule effect up to 700 °C. Moreover it has five degrees of freedom (three translations, two rotations): in this configuration the sample can be placed in the proper position for: (i) thin films deposition; (ii) substrate sputter-cleaning by means of a differentially pumped ion gun; (iii) surface quality control via Low Energy Electron Diffraction (LEED).

Thin film deposition by thermal evaporation is achieved by electron bombardment of high purity metal rods, for 3d metals like Fe or Co, or of Mo/Ta crucibles containing the low melting point noble metals (as Au). Such a kind of crucible is used as well for the evaporation of stoichiometric MgO (from pieces of stoichiometric MgO commercial substrates). The six evaporation cells, all pointing to a common position (the center of the chamber), are surrounded by a water cooled jacket to keep UHV pressure during operation. The deposition rates are calibrated through a quartz crystal micro-balance

which can be placed exactly in the same position of the sample. Typical growth rates are 0.3Å/min (MgO) and 3Å/min (Fe, Co) for deposition of ultra-thin films (up to some hundred Å).

In the SPC it is possible to probe the quality of the surface by means of LEED. An electron gun generates a beam with energies ranging from 20 to 300 eV. These energies are particularly suitable to study the order of the surface for two reasons: (i) the electron wavelength (in the order of few Angstrom) is compatible with the typical lattice parameter of crystal and a diffraction pattern related to the crystal lattice can be obtained; (ii) the mean free path of such slow electrons (in the order of 10 Å) permits to obtain a high surface sensitivity [68]. The diffraction pattern from back-scattered electrons is recorded on a fluorescent screen and the analysis of the spot positions yields information on the size, symmetry and rotational alignment of the surface lattice unit cell. Technically speaking, the LEED optics are retractile and protected by a movable shutter from possible damages during ion sputtering and evaporation.

3.1.3 Other depositions

Pt layers were deposited with the help of D. Gutierrez by sputtering in ICMAB. Top Cr/Au or Ti/Au electrodes were deposited by e-beam evaporation in L-NESS. SiO_2 insulating layers were deposited by sputtering by D. Petti in L-NESS.

3.2 Devices design and optical lithography

Optical lithography is a widely used technique used for the micro-fabrication of electronic devices. This technique is based on the transfer of a bidimensional image (the *pattern* drawn on a proper chromium mask) on a radiation sensitive polymeric material (called *photoresist*). This property is useful to differentiate the surface of a photoresist covered sample in different subsequent treatments.

A lithographic process is illustrated in Figure 3.2.1 and consists in several

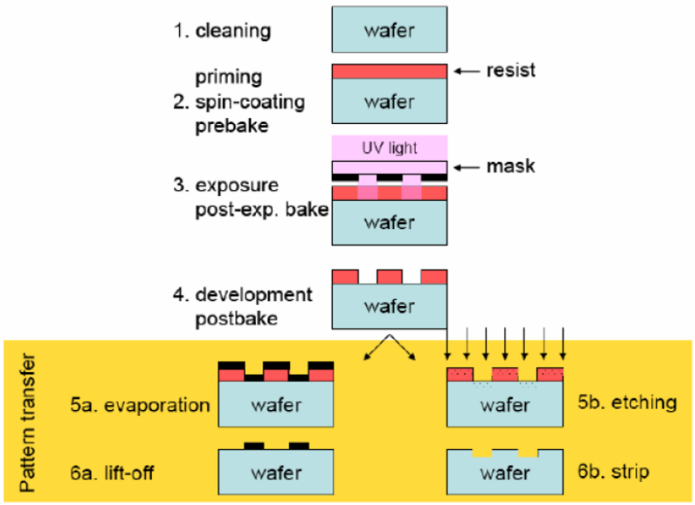

Figure 3.2.1: Schematic of an optolithographic process.

steps described in the following.

1. **Sample cleaning of the sample.** Superficial contamination has a bad influence on the resist adhesion and on the quality of the transferred image. The cleaning of the sample consists in general of an ultrasonic bath in acetone or a soft bake in order to desorb water. A better adhesion of the resist is achieved on hydrophobic surface, because the polymer is an apolar substance and the formation of polar bounds O-H prevent the resist from wetting the substrate. A promoter of the adhesion (*Primer*) makes the surfaces hydrophobic and is deposited in the same manner as the photoresist (see below).

2. **Deposition of the photoresist onto the sample.** The deposition of the resist occurs via *spin coating*. Some drops of resist are dispensed on the sample, which is put in rotation at high speed. The centrifuge force at about 1000 rpm spreads the resist, creating a uniform, thin (some microns thick) layer. The spin coating presents different advantages: firstly velocity of the process and high homogeneity of the layer. Moreover during the rotation the evaporation of the solvent containing

the polymer takes place. On the contrary, the spinning can give problems if the sample has not rotational symmetry: the resist becomes thicker in the corners and problems can arise during the development. After the photoresist deposition, a soft bake removes the solvent left and decreases the mechanical stress, introduced during the spinning and preparing the photoresist for the next step. The resist employed for the realization of the devices presented in this work is the image reversal positive photoresist AZ 5214E from MicroChemicals© GmbH.

3. **Exposure to UV light with a proper mask containing the pattern.** The exposure to light radiation modifies the chemical properties of the photo-resist, producing a different solubility in a proper solution (the developer) of the exposed and unexposed part of the film. In the case of the positive resist AZ 5214E, the exposed regions become more soluble and are thus easily removed in the development process. UV radiation has been used and the image transfer is realized through a mask patterned with Cr: where the metals is present on the mask, it adsorbs the radiation protecting the underlying resist from the exposure. In this way it's possible to transfer the Cr pattern into a resist pattern. To align the mask with respect to the sample and to expose the photo-resist, we employed the Karl Suss MA56 mask aligner, which allows to realize the exposure both in contact and proximity modes. It supports mask up to five inches and wafers up to four inches in diameter. The UV radiation is obtained from the Hg-I line (365 nm) of a mercury lamp that provide a power per unit area of about 10 mW/cm^2. The maximum achievable resolution is measured as critical dimension (CD), the linear dimension of the smallest object that is transferable from the mask to the resist. The resolution in terms of CD is limited by the diffraction limit, by the quality of the mask and by the properties (i.e. contrast) of the photoresist. In our case, the resolution is limited by the photoresist AZ 1215E and the CD is in the order of 1 μm.

4. **Development of the exposed photoresist.** During the developing process, an appropriate solvent (AZ100 DEV from MicroChemicals© GmbH) removes the part of resist not belonging to the image. In case of positive resist, the exposed part is dissolved, while the part protected by the Cr of the mask during the exposure remains on the substrate. For a negative resist the mechanism is opposite.

5. **Subtractive or additive process (etching or deposition of material).** In a subtractive process, the function of the resist is protecting the underlying material from the removal; the removal of the material from the sample is performed through ion beam etching. A plasma of ions Ar^+ is created, the ions are accelerated and impinge on the surface. The impact breaks the bonds between atoms, which are removed from the sample. On the contrary, an addictive process consists in a deposition of material by means of electronic evaporation or sputtering. In this case, the resist prevents the adhesion of new materials onto covered parts.

6. **Strip or lift-off .** After the ion beam etching a strip of the resist gives a pattern with some parts in relief, corresponding to the metallic zone of the mask. In the case of deposition the lift off of the resist removes also the overlying material: the pattern consists in deposited material in correspondence to the exposed part of the sample surface.

In the following paragraphs we describe the design of devices employed in this thesis and the details of the lithographic process employed for their fabrication. In particular, paragraph 3.2.1 is dedicated to the fabrication of capacitors used in chapter 4; and paragraph 3.2.2 to the fabrication of tunnel junction devices employed both in chapter 4 and 5. Fabrication processes have been performed in L-NESS center.

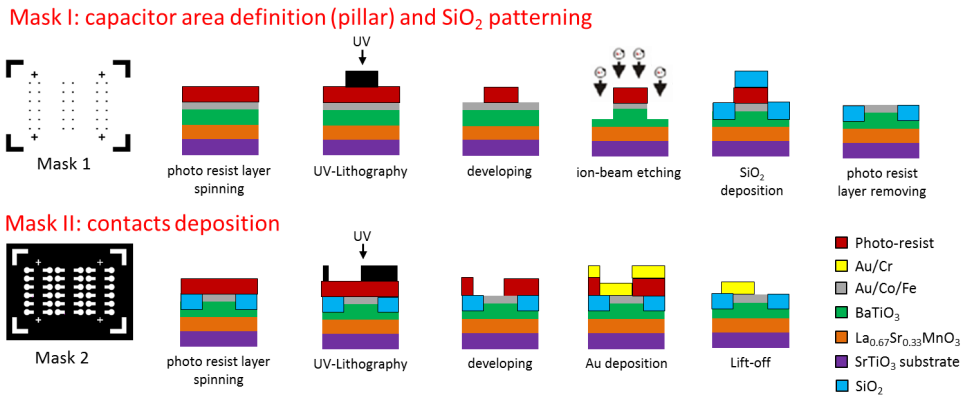

Figure 3.2.2: Schematic of the lithographic process employed to realize capacitors.

3.2.1 Capacitors

Rectangular capacitors with different dimensions have been produced with a two-steps process on $Au/Co/Fe/BaTiO_3/La_{0.67}Sr_{0.33}MnO_3/SrTiO_3(001)$ or $Au/Fe/BaTiO_3/La_{0.67}Sr_{0.33}MnO_3/SrTiO_3(001)$ heterostructures. The area of the devices can be $A_1 = 0.02mm^2$ or $A_2 = 1mm^2$, depending on the used mask. A single sample (7 x 5 mm^2) can arrange up to 36 capacitors of area A_1 or 6 capacitors of area A_2. The process flow is presented in Fig. 3.2.2.

1. Optical lithography of the capacitor structure:

   (a) Deposition of 1.25 μm thick AZ5214 photoresist, exposition to about 125 mJ/cm^2 dose of UV light with mask 1 (Fig. 3.2.2) and developing.

   (b) Ion beam etching for the definition of the capacitor structure till about half of the thickness of $BaTiO_3$ film. Etching time was calculated using the etching rates listed in the manual, in this step an error on the etching time is not crucial, since the $BaTiO_3$ film is quite thick (about 150 nm).

   (c) Deposition of SiO_2 insulating layer by sputtering to prevent from shortcuts between the top and bottom electrode (thickness set to

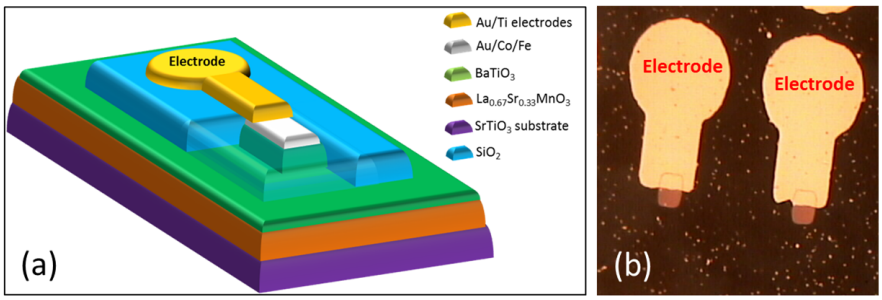

Figure 3.2.3: (a) 3D view of a capacitor. (b) Optical image of two capacitors at the end of the lithographic process.

obtain planarity of the device).

(d) Resist removal (AZ100 resist remover in an hot ultrasonic bath).

2. Optical lithography of the top contacts:

   (a) Deposition of 1.25 μm thick AZ5214 photoresist, exposition to about 125 mJ/cm^2 dose of UV light with mask 2 (Fig. 3.2.2) and developing.

   (b) Electronic evaporation of the contacts (15 nm of titanium as adhesive layer, 200 nm Au).

   (c) Lift off of the excess of metal on non-exposed areas (AZ100 resist remover in an ultrasonic bath).

The sketch of a capacitor is shown in Fig. 3.2.3(a) together with a photo acquired with a microscope on a lithographed sample (Fig. 3.2.3(b)).

3.2.2 Tunnel junctions

Tunnel junctions with different shapes and dimensions can be produced in a three-steps process. We will consider as starting point the general heterostructure: top layer/barrier/bottom layer/substrate. The area of the devices A ranges from 4 μm^2 to 1600 μm^2. A single sample (10x10 mm^2) can arrange up to 36 junctions. The process flow is presented in Fig. 3.2.4.

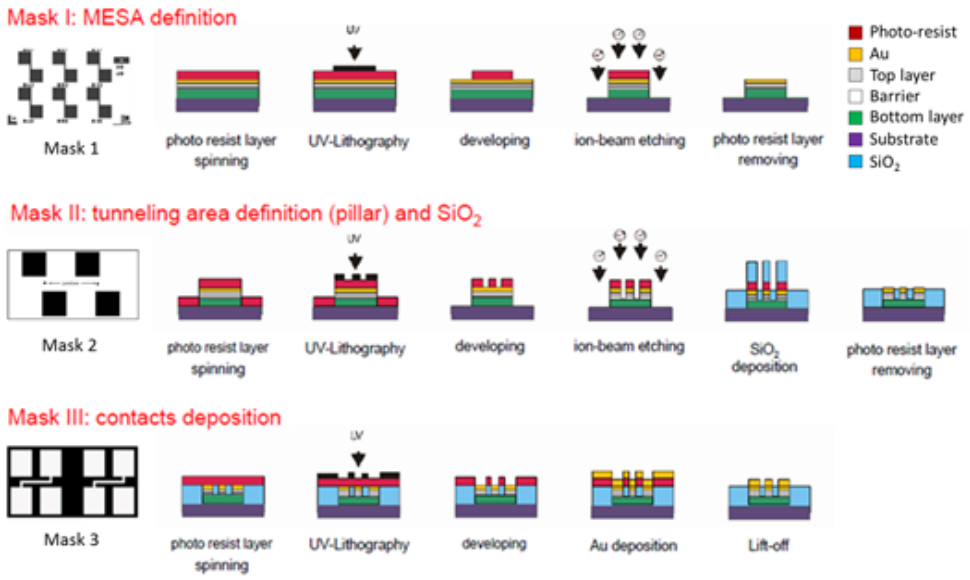

Figure 3.2.4: Schematic of the lithographic process employed to realize tunnel junctions. All the geometries involved in the process are patterned on the same lithographic chromium mask.

1. Optical lithography of mesa structure:

   (a) Deposition of 1.25 μm thick AZ5214 photoresist, exposition to about 125 mJ/cm^2 dose of UV light with mask 1 (Fig. 3.2.4) and developing.

   (b) Ion beam etching for the definition of the mesa structure till reaching the substrate. Etching time was calculated using the etching rates listed in the manual, in this step an error on the etching time is not crucial. An excessive etching leads to erosion of the insulating substrate without problematic consequences; a short etching leaves part of the bottom layer which cortocircuits the junctions but which can be easily recognized with an electrical measurement and solved with further etching of the sample.

   (c) Resist removal (AZ100 resist remover in an hot ultrasonic bath).

2. Optical lithography of the junction area and of the bottom electrode:

(a) Deposition of 1.25 μm thick AZ5214 photoresist, exposition to about 125 mJ/cm^2 dose of UV light with mask 2 (Fig. 3.2.4) and developing.

(b) Ion beam etching to define the pillar and bottom pads underneath the tunnel barrier. Note that in this step a *flag* is used as reference for the etching time which is crucial. An excessive etching leads to erosion of the bottom layer and consequent disconnection of the bottom electrodes from the junction; a short etching leaves part of the top layer which cortocircuits the junctions.

(c) Deposition of SiO_2 insulating layer by sputtering to prevent from shortcuts between the top and bottom electrode (thickness set to obtain planarity of the device).

(d) Resist removal (AZ100 resist remover in an hot ultrasonic bath).

3. Optical lithography of the top contacts:

(a) Deposition of 1.25 μm thick AZ5214 photoresist, exposition to about 125 mJ/cm^2 dose of UV light with mask 3 (Fig. 3.2.4) and developing.

(b) Electronic evaporation of the contacts (5 nm of chromium as adhesive layer, 150 nm Au).

(c) Lift off of the excess of metal on exposed areas (AZ100 resist remover in an ultrasonic bath).

A sketch of a tunneling junction device is shown in Fig. 3.2.5(a) together with a picture acquired with a microscope on a lithographed sample (Fig. 3.2.5(b)). Note that the bottom electrode is a tunneling junction itself but its dimension is such that its resistance is negligible with respect to that of the junction for two reasons: (i) the area of the bottom contact (500 x 500 μm^2) is huge with respect to that of a junction (the maximum area is 1600 μm^2); (ii) on such a large area, the presence of pinholes in the barrier layer makes the bottom contact ohmic.

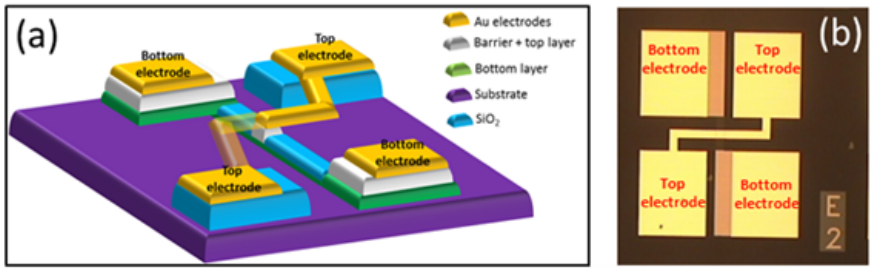

Figure 3.2.5: (a) 3D view of the complete junction. (b) Optical image of a tunneling junction at the end of the lithographic process.

3.3 Structural, morphological and chemical characterization techniques

This part will describe various structural, morphological and chemical characterization techniques used in this thesis, including x-ray diffraction (subsection 3.3.1), x-ray reflection (subsection 3.3.2), atomic force microscopy (subsection 3.3.3), X-ray photoemission spectroscopy (subsection 3.3.4) and scanning transmission electron microscope and electron energy-loss spectroscopy (STEM-EELS, subsection 3.3.5).

3.3.1 X-ray diffraction

The X-ray diffraction (XRD) experiments were carried out at ICMAB using a Siemens D-500 diffractometer. Reciprocal space maps (RSM) were collected using a Bruker lT8 Advance diffractometer equipped with a bidimensional detector. Some measurements have been performed at L-NESS with the help of D. Chrastina using a PANalytical PRO-MRD high-resolution triple-crystal diffractometer.

Diffraction from X rays (XRD) is a non-destructive standard technique for the characterization of the crystal structure of the materials. It allows identifying phases, the symmetry of the unit cell, its lattice parameters and the atomic positions. XRD is based on the interpretation of the interference pattern created when an ideally monochromatic beam of light is directed on

a periodic structure. In crystalline materials the periodic arrangement of atoms acts as this periodic structure. X rays have wavelengths (λ) of the order of the atomic lattice spacing (d_l) and, when impinging at an angle $\omega = \theta_l$ respect to the plane of the sample (see Fig. 3.3.1), give diffraction in agreement with the Bragg's law:

$$d_l = \frac{n\lambda}{2sin\theta_l} \tag{3.3.1}$$

where l is the order of diffraction.

The intensity recorded at the detector while scanning the θ angle with the detector kept at 2θ angle respect to the incoming beam is known as a $\theta/2\theta$ scan. This procedure allows identifying the interplanar spacings present in the sample in the direction perpendicular to the sample plane. In polycrystalline samples (for instance, target powder) the grains are randomly oriented so all the interplanar distances of one particular phase and compound can be observed in the spectra. Since these distances are characteristic of each compound and phase, the $\theta/2\theta$ pattern allows identifying which phases and compounds are present. In the case of epitaxial thin films, only a family of planes will be expected to be exactly oriented perpendicular to the sample plane and thus observed in the $\theta/2\theta$ scan. This family of planes is the texture of the film. From the angular location of the peaks the interplanar distance can be inferred so providing information on the epitaxial strain along the out-of-plane direction.

The first figure of merit of the crystal quality of the film is monitored via the rocking curves. These are based on relatively small range scan of the ω motor around the nominal position of a diffraction peak keeping the detector fixed. A Voigt-type profile of intensity is obtained which its full width at half maximum accounts for the mosaicity in the out-of-plane direction of the sample.

The reflections not contained in the plane of the sample (so-called "asymmetrical reflections") can be explored by rotating the sample using the following angles as shown in Figure 3.3.1:

- φ, around the normal of the samples

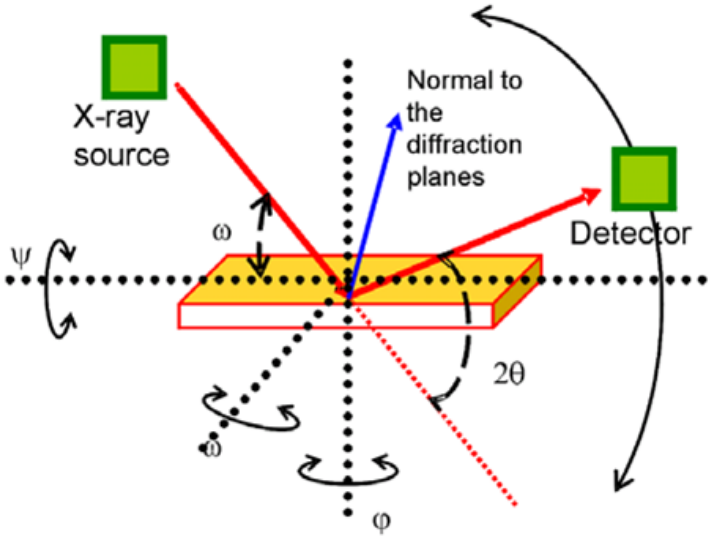

Figure 3.3.1: Sketch of the angles involved in XRD experiments.

- ψ, around in-plane axis of the film not contained in the diffraction plane

In present thesis the analysis of asymmetric reflections were performed collecting reciprocal space maps (RSM, q-plots). In RSMs several $\omega-2\theta$ coupled scans are collected for different values of ω (that is, for different tiltings of the sample), around a reflection of the sample. RSM gives information of the in-plane and out-of-plane parameters of the sample, of possible structural distortions, relaxation in the films or the presence of defects. The result is a 2-D map (2θ,ω) which display intensity peaks. Then, the positions in the reciprocal space for the chosen reflection are given by:

$$q_{\parallel} = \frac{2}{\lambda} sin(\theta) sin(\theta - \omega) \tag{3.3.2}$$

$$q_{\perp} = \frac{2}{\lambda} sin(\theta) cos(\theta - \omega) \tag{3.3.3}$$

From the values of the wave vectors $q_{\parallel}$ and $q_{\perp}$ ($\parallel$ and $\perp$ to the plane of the sample surface) obtained for the film reflections, one can calulate the distances in the real space, by knowing the relationship between the lattice in the real and reciprocal spaces. As an example, in a tetragonal system, with lattice parameters $a = b \neq c$, the reflection $[hkl]$, in-plane lattice parameter

can be calculated as

$$a = \frac{\sqrt{h^2 + k^2}2}{q_{\parallel}} \tag{3.3.4}$$

and out-of-plane parameter

$$c = \frac{l}{q_{\perp}} \tag{3.3.5}$$

Further information can be obtained by examining the obtained maps. In general, if a film grown fully strained on a single crystal substrate, the $q_{\parallel}$ coordinates of film and substrate coincide for both symmetrical and asymmetrical reflections. Some indicatives of relaxation can be found if a gradient of intensity towards the bulk expected position of the film material is observed. Also compositional gradients can be found along the relaxation line of the film (linking substrate and bulk position of the film).

3.3.2 X-ray reflection

The X-ray reflection (XRR) experiments were carried out at ICMAB using a Rigaku RU-200B diffractometer.

X-ray reflectivity (XRR) is used to determine the film's thickness in monolayers or multilayers if the thicknesses are in the 10-100 nm range and the roughness of top-most surface and interfaces is not too large. In an XRR experiment an incoming X-ray beam impinges on the film surface at very low incident angle θ_i as shown in Figure 3.3.2. The detector is placed always at the right side, at an angle $\theta_o = \theta_i$. If the incident angle surpass the critical angle of the film's material, part of the incident beam is reflected (o_1) and some part is diffracted inside and out again (o_2). Both beams are parallel and may present interference fringes depending on the optical path traveled by o_2 inside the film. In contrast to X-ray diffraction experiments, it is now critical to take into account the refractive effects which are relevant at low angles (XRR) but can be neglected at higher angles. The extra path can be derived using trigonometry and Snell's law. The final interference condition is given by:

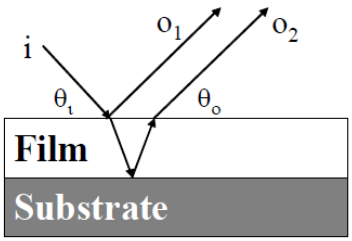

Figure 3.3.2: Sketch of the XRR experiment with the incident rays "i", the directly reflected light "o_1", the rays that reflect inside the films and goes out again "o_2". Note that $o_1$and o_2 are parallel.

$$2d\sqrt{sin^2(\theta) - sin^2(\theta_c)} = n\lambda \tag{3.3.6}$$

Where d accounts for the thickness of the film, θ for the incident and outgoing angle, θ_c for the critical angle, λ for the wavelength of the X-rays source, and n for the index of refraction. The previous equation corresponds to the Bragg's law with the corrections for refraction effects.

To perform the analysis, θ_i is scanned (note that $\theta_o = \theta_i$ moves accordingly) in the range of 0.5 - 5°. Data presents the decay of reflectivity as expected by Fresnel equations with the overlapped oscillations due to the interference between o_1 and o_2. The position of the maxima must be fitted versus the order of the oscillation n. The slope contains d which is the thickness of the film. It is more convenient to deal with the square of Eq 3.3.2:

$$\left(\frac{2d}{\lambda}\right)^2 sin^2(\theta) - \left(\frac{2d}{\lambda}\right)^2 sin^2(\theta_c) = n^2 \tag{3.3.7}$$

In this case the linear fitting allows determining the thickness and, from the independent term, the critical angle which, as a crosscheck, must be consistent with the obtained value by inspection of the derivative of the data and of the same order of the predicted and/or tabulated one. By this, the eventual error in the assignation of n (the order of the oscillation) is prevented.

3.3.3 Atomic force microscopy

The topographic Atomic Force Microscopy (AFM) images in the present work were obtained by an Agilent 5100 system at ICMAB. Some measurements were performed at L-NESS using an Innova Veeco system. The scans were performed in tapping mode. The treatment of the data was done by Gwyddion 2.22 software.

The atomic force microscope (AFM) is a tool allowing to determine direct images of solid state material surfaces as well as details about film roughness. To obtain the topography images the AFM uses the interaction between a small tip and the sample surface. The advantage of AFM is the fast and simple measurement with a high resolution. In contrast to the scanning tunneling microscope (STM) vacuum is not necessary and measurements can be carried out on every solid state material. Figure 3.3.3 shows the design of a standard AFM system. The sample is mounted on a piezoscanner responsible for the movements in the x, y and z directions. The tip is attached on a cantilever and it is generally made out of silicon or silicon nitride with a nominal radius of 5-10 nm. During the measurement, the tip moves a few hundred angstroms over the surface or even slightly touches it. An interaction force between the tip and the surface leads to a deflection of the cantilever. This deflection of the cantilever is detected optically. A laser beam is reflected on the tip surface and hits the photodetector which consists of a four-section split photodiode able to detect displacements of the laser beam of 10Å. Monitoring the difference between opposite diodes, the knowledge of the distance proportion between the tip and the detector and the length of the cantilever allows a quantification of movements at the Angstrom scale. The difference of the top and bottom diodes identifies the torsion of the tip. These mechanical movements are transformed into electric signals. The use of appropriate software allows real topography images of the sample surface to be created.

There are two basic modes of operation: the contact or the non-contact mode (tapping mode). Each mode uses different physical effects for surface analysis. In the contact mode, the tip actually makes physical contact

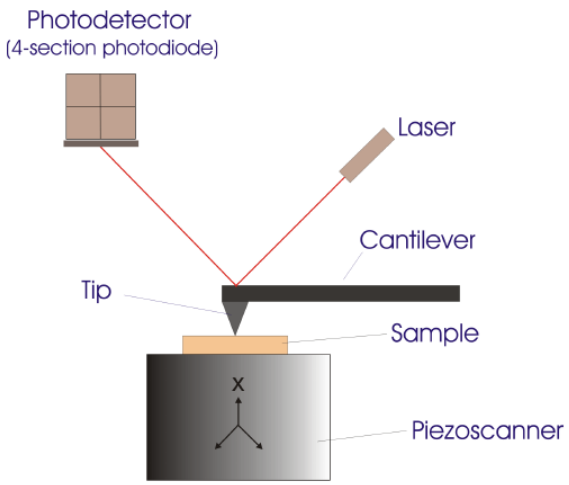

Figure 3.3.3: Sketch of an atomic force microscope.

with the surface. The tip is approached to the sample until the interactions between the tip and the sample cause the bending of the cantilever. This bending (also called deflection) is registered by detecting the reflection of a laser inciding in the cantilever head. This way, as the tip is scanned though the sample, the cantilever deflection is measured. In the non-contact mode (tapping mode), an oscillation of the cantilever is produced near the sample's surface (typically 10-100 Angstroms). This mode has the advantage of lowering the possible sample contamination and reducing the tip damage. On the other hand, the force registered will be some orders of magnitude lower than in contact mode. The cantilever is vibrated at a frequency close to its resonance (on the order of hundreds of kHz); when it is approached to the sample, changes in the resonance frequency or in the oscillation amplitude are registered. At the same time, the phase lag between the input oscillation signal and the cantilever output can be recorded. This phase lag is used to monitor changes in the mechanical properties of the sample surface, detecting regions with different adhesion or friction. This information can, in some cases, be conected to chemical changes in the sample surface.

3.3.4 X-ray photoemission spectroscopy

X-ray photoemission spectroscopy (XPS) experiments were carried out in-situ in the measurement chamber of LASSE system (MC p_{base}=$1 \cdot 10^{-10}$torr, Fig. 3.0.1) in LNESS. In MC the (x, y, z, θ, ϕ) manipulator lies horizontally, i.e., along a diameter of the chamber central body. The source of photons is an X-ray tube. Mg or Al anodes, bombarded with 13.5 keV electrons, emit radiations corresponding to the Mg-$K\alpha_{1,2}$ (E = 1253.67 eV, $\Delta E = 0.84$ eV) or Al-$K\alpha_{1,2}$ (E = 1486.67 eV, $\Delta E = 1.03$ eV) lines, respectively. The anode is cooled down in order to maximize the emission intensity. The chamber is equipped with a hemispherical energy analyzer (HEA PHOIBOS 150-SPECS), with variable acceptance angle and field of view. The hemispherical energy analyzer, inserted from the top, is constituted of two hemi-spheres implementing a capacitor. Electrons follow different trajectories between the spheres depending on their energy and on the electric field in the hemispherical capacitor, so that only the electrons with a fixed energy (pass energy, E_0) are focalized on the exit slit. Here 9 channeltron constitute a first step of amplification of the signal which is successively electronically treated and sent to a PC which shows in real time, and records, the emission spectra.

Photoemission spectroscopy is based on the photoelectric effect: when a solid is irradiated by monochromatic light, photons excite the electrons into unoccupied states and, if their energy exceed the solid work function, they can escape from the sample and be detected by the analyzer. The detected electrons have a kinetic energy with respect to the analyzer electrodes, given by:

$$E_k = \hbar\omega - E_i - \psi \tag{3.3.8}$$

where $\hbar\omega$ is the energy of the incoming photons, E_i is the binding energy of the initial state and ψ is the analyzer work function. The E_i energies are a fingerprint of the different atomic species and also reflect their chemical environment, so that the detected photoelectrons allow identifying the species present in the sample. The measured distribution of the sharp peaks is superimposed on the secondary background, which arises from electrons that have lost quasi-continuous amounts of energy due to multiple inelastic

scattering events in the crystal. As the mean free path of the photoelectrons excited with standard Al or Mg-kα radiation (1486.6 and 1253.6 eV, respectively) in the solid is of the order of a few tens of Angstroms and, therefore, XPS remains as a surface-sensitive technique. Within this range, the probing depth can be tuned by selecting the incident angle of the incoming photons.

3.3.5 STEM-EELS

Scanning transmission electron microscope (STEM) and electron energy-loss spectroscopy (EELS) analysis were carried out by M. Varela at Oak Ridge National Laboratory (USA). Samples for STEM-EELS were prepared by conventional methods: polishing and Ar ion milling. The samples were studied in a Nion UltraSTEM200 operated at 200 kV and equipped with a 5^{th} order Nion aberration corrector and a Gatan Enfinium spectrometer, and also in a Nion UltraSTEM100 operated at 100 kV equipped with a Nion aberration corrector and a Gatan Enfina spectrometer. In some cases, random noise was removed by using principal component analysis.

Electron Microscopes work exactly as their optical counterparts except that they use a focused beam of electrons instead of light to 'image' the specimen and gain information as to its structure and composition. A stream of electrons is formed by an electron source and accelerated toward the specimen using a electrical potential. This stream is confined and focused using metal apertures and magnetic lenses into a thin, focused, monochromatic beam, which is focused onto the sample using a magnetic lens. Interactions occurring inside the irradiated sample are affecting the transmitted electrons. The transmitted electrons are detected and transformed into an image. With TEM, information on microstructure is gained, but in the case of a high resolution TEM, also on crystallographic properties like lattice parameter or on atomic-scale defects.

In Electron Energy Loss Spectroscopy (EELS) the electrons with a known kinetic energy undergo inelastic scattering because of interactions with phonon, plasmons and, most important, because of inner shell ionization processes. This latter mechanism is sensitive to the chemical element and its environ-

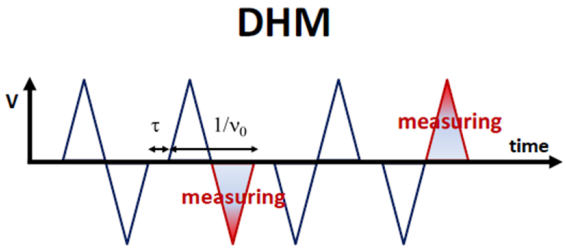

Figure 3.4.1: Voltage train pulses that are applied in DHM, shaded areas correspond to the pulses at which the current measurement is performed. ν_0 is the measurements frequency and τ the delay time between pulses [69].

ment and allows element sensitive imaging and chemical analysis of the sample with high spatial resolution.

3.4 Dielectric & ferroelectric characterization techniques

Dielectric characterization has been performed in ICMAB with the help of D. Gutierrez and I. Fina using an impedancemeter HP4192A LF (Agilent Co.), which measures the impedance and the phase of the connected circuit (which includes the sample and the wiring). The available measuring frequency range is between 5 Hz - 13 MHz and the oscillating voltage has been set to 300 mV. With the impedancemeter we have performed impedance spectroscopy (IS), i.e. analysis of ε-ν and ε-E measurements. IS and C-V measurements have been performed also in L-NESS with a LCR meter (the support of Prof. Bertuccio is acknowledged) to investigate the dielectric properties of the films. The available measuring frequency range is between 10 Hz - 1 MHz and the oscillating voltage has been set to 200 mV. Real impedance spectra ($\vec{Z}$) have been fitted with a suitable equivalent circuit using the Zview software, which does a simultaneous fit of Z' and Z" dependence on ν by using a least-squares algorithm. From the fitting results, the intrinsic values for the dielectric permittivity and conductivity of the film can be extracted.

Ferroelectric loops have been performed in ICMAB with the help of D. Gutierrez and I. Fina using a TFAnalyser2000 (AixACCT System GmbH. Co.), which measures the current versus the applied voltages up to 25 V at frequencies between 5 x10^{-4} Hz and 2 x10^{6} Hz. *I-V* characteristics are measured, which provide an abrupt current peak where the ferroelectric switching (switching between P^+ and P^- at coercive field) occurs, and allows to easily disclose the extrinsic ferroelectric effects. Charge is afterwards obtained integrating the current through the time. When a plano-parallel capacitor with known geometry (area, A, and thickness, t) is used, the polarization and electric field can be obtained. Polarization is the charge per unit surface, and the electric field is obtained by dividing the applied voltage (V) by the thickness.

$$P = \frac{\int I(t)dt}{A} \tag{3.4.1}$$

$$E = \frac{V}{t} \tag{3.4.2}$$

The measurement of an *I-V* loop consists in applying a time-dependent electric field on the sample while recording the current. *I-V* loops in the present work have been recorded using the so-called Dynamic Hysteresis Mode (DHM): four bipolar triangular excitation signals of frequency ν_0 are applied with a delay time τ between them (Figure 3.4.1). The final *I-V* loop is obtained from the combination of the currents measured while applying the negative voltage during the second pulse and the positive voltage during the fourth pulse (negative and positive voltages, respectively). The first and the third pulses are necessary in order to obtain the same measurement conditions while recording the positive and the negative part of the final loop. This method is specially convenient because it does not continuously cycle the sample, avoiding the aging (fatigue).

The I-V curves obtained by DHM can be corrected for leakage effects using the Dielectric Leakage Current Compensation (DLCC) method. This method is based on two assumptions: that the leakage current $I_{leakage}$ is independent of frequency and that the dielectric current I_ε and the current due to the

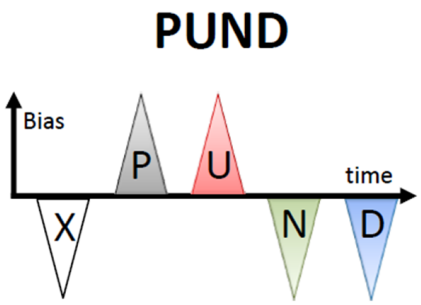

Figure 3.4.2: Voltage train pulses during PUND (Positive-Up-Negative-Down) [69].

ferroelectric switching I_{FE} are both linearly depending on frequency. Under these hypotheses, measuring the DHM cycles at two frequencies (ν_0 and $\nu_0/2$) allows subtraction of $I_{leakage}$, and thus only the displacement current remains.

Positive-Up-Negative-Down (PUND) technique has been used instead to obtain reliable values for remanent polarization. In the used PUND measurement five voltage pulses are applied to the sample (Figure 3.4.2). The first is negative and pre-polarizes the sample to a negative polar state. The second and the third pulses are positive: the second (P) polarizes the sample and therefore the corresponding current contains the ferroelectric and non-ferroelectric contributions, while current during the third (U) pulse only contains the non-ferroelectric contributions; therefore, their subtraction allows to obtain, in principle, only the ferroelectric contribution. The same applies for the fourth (N) and the fifth pulses (D), for the negative state, so that the current loop $I_{PUND} - V$ is obtained from $I_P - I_U$ for the positive voltages and from $I_N - I_D$ for the negative voltages. Consequently, PUND current only contains the switchable ferroelectric contribution and all the other contributions are excluded, $I_{PUND} = I_{FE}$.

Dielectric and ferroelectric characterizations have been performed using two measurements configuration: the bottom-top and the top-top (Figure 3.4.3). In the bottom-top configuration the bottom and top electrodes are contacted. This is an asymmetric configuration, because bottom electrode-insulator and insulator-top electrode interfaces can be different, owing to the

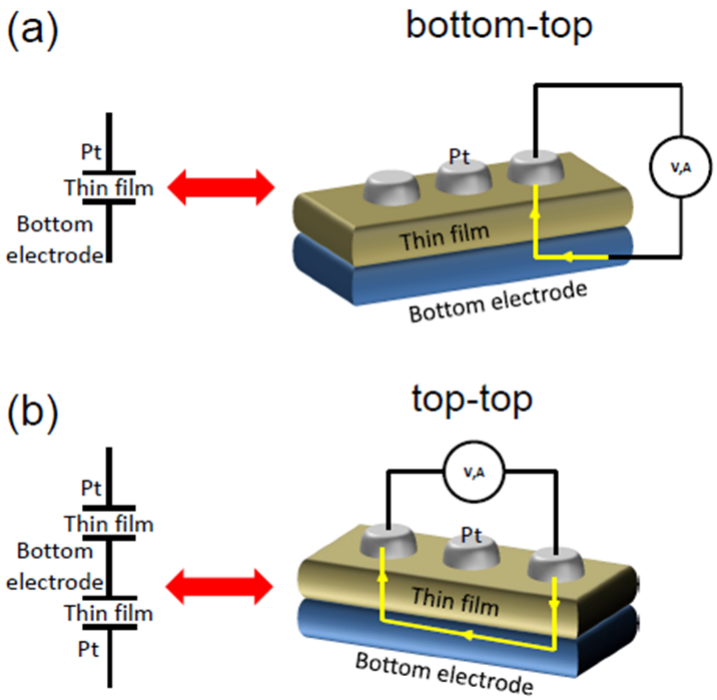

Figure 3.4.3: Schemes (left) and sketches (right) of bottom-top (a) and top-bottom (b) measurement configuration [69].

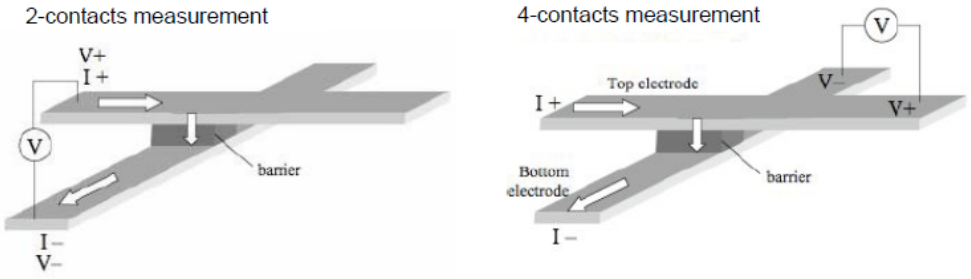

Figure 3.5.1: 2-contacts and 4-contacts configurations for I(V) measurements of tunnel junctions.

fact that top and bottom electrode materials are different. In the top-top configuration two top electrodes are contacted. Therefore, the measured capacitance should correspond to a series of two identical capacitors contacted through the bottom electrode. This is equivalent to the measurement of a single thin film capacitors with double thickness. With this configuration, the asymmetries due to the different metal-insulator interfaces cancel out.

3.5 Transport measurements set-up

The I(V) characteristic studies have been carried out in a 2-contacts or 4-contacts configuration. Four probes allow to overcome the problem of voltage drop on contacts and cables.

I(V) characteristic studies of tunnel junctions were performed both at ICMAB and L-NESS either in the four or two contacts configuration, according to the scheme of figure 3.5.1. The 4-contacts system permits a precise measurement of the voltage drop across the tunnel junction ($V = I\ R_{junction}$), while in a 2-contacts configuration the voltage drop is measured across both the electrodes and the junction ($V = I\ (R_{junction} + R_{top} + R_{bottom})$). The geometry of the junctions (see subsection 3.2.2 for more details), with two contacts for both the bottom and the top electrode, allows both the configurations. Room temperature measurements were performed using a probe station connected to a Keithley 2611. Temperature dependent measurements were performed using a Physical PPMS from QD in ICMAB and an helium

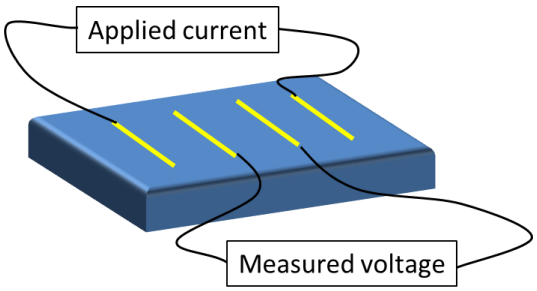

Figure 3.5.2: Scheme of the four probes configuration used for the measurements of electrical resistivity of half-doped manganite films.

cryostat connected to a Keithley 2611 in L-NESS. In this case the contacts are performed through wire bonding, which permits to arrange the sample inside the PPMS/cryostat.

Electrical resistivity of half-doped manganite ($La_{0.5}A_{0.5}MnO_3$, A = Ca/Sr) films was measured in ICMAB either in the four or two probes configuration, using a Physical PPMS from QD. Contacts are performed through wire bonding, which permits to arrange the sample inside the PPMS. Scheme of the four probes configuration is shown in figure 3.5.2.

3.6 Magnetic and transport characterization techniques

3.6.1 X-ray Magnetic Circular Dichroism

X-ray magnetic circular dichroism (XMCD) experiments were carried out at APE beamline of the ELETTRA synchrotron radiation source in Trieste (Italy) with the help of P. Torelli, B. R. Salles and G. Panaccione. X-ray absorption spectra (XAS) of the $L_{2,3}$ edge of Fe and Co have been collected in total electron yield (TEY) with fast scan mode, i.e. by changing the incoming photon energy in a continuous way while measuring the sample drain current by means of a picoammeter inserted between the surface of the sample and ground, for a fixed light helicity (σ^+ and σ^-) and magnetization direction (m^+ and m^-). Four XAS spectra have been collected for the different

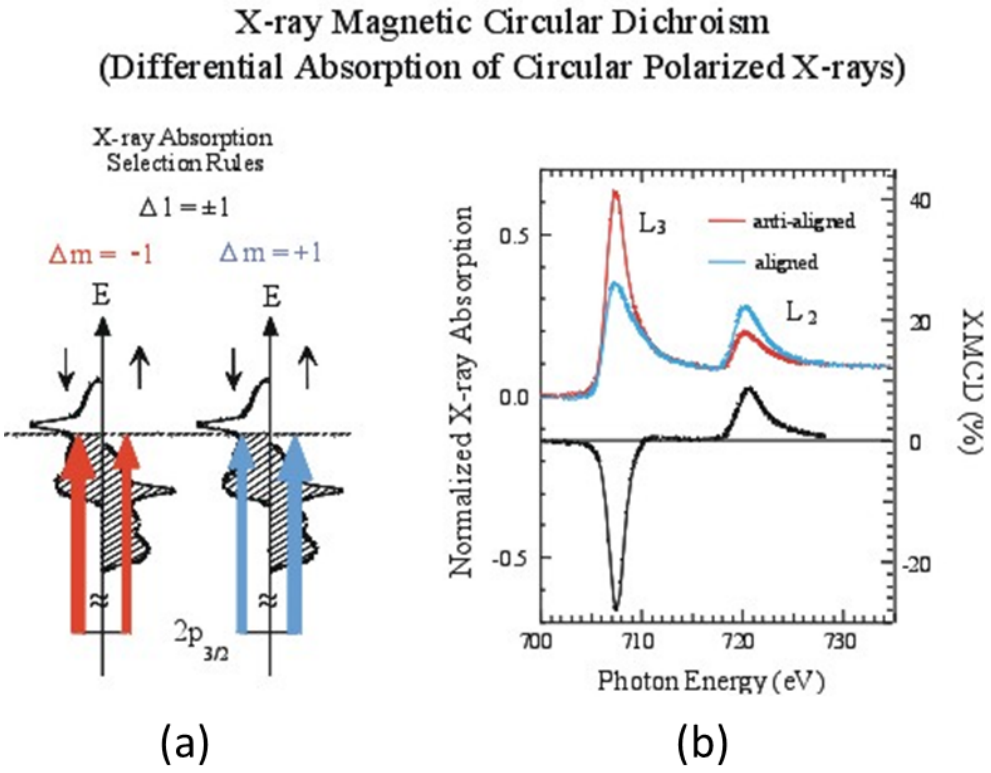

Figure 3.6.1: (a) Spin resolved density of states of a half-metallic ferromagnet. (b) On the top part is the XAS spectra acquired with each of the light polarizations and on the bottom is the "difference" spectrum, the XMCD [70].

combinations of light helicity and sample magnetization ($\sigma^{+/-}$ and $m^{+/-}$) in order to get rid of instrumental asymmetries. The polar angle of incidence of the incoming light was kept fixed at 45° with respect to the direction of the magnetizing field. In the XAS measurement, data have been taken in magnetic remanence, upon application of magnetic pulses of 200 Oe.

XMCD is a variant of XAS in which circular polarized light is used. Two spectra are acquired, one with right circular polarized light and one with left circular polarized light. When electrons absorb a photon they are promoted from a core level just above the Fermi level. According to the dipole selection rules, for each magnetization direction, electrons of one spin direction will preferentially be promoted to the Fermi level according to whether right

or left circular polarization is used. With the other polarization, the other spin direction electrons will be promoted to the Fermi level. However, in a magnetic material the density of states at the Fermi level differs for the two spin orientations. For instance, in case of a half-metallic ferromagnet, whose spin resolved density of states is shown in Figure 3.6.1, the density of states of one of the two spin orientations is zero at the Fermi level. The absorption observed will then be different for the two light polarizations used and we effectively measure the spin populations at the Fermi level for majority and minority electrons. By subtracting the two spectra taken with opposite light helicity, a signal proportional to the sample magnetization is obtained. Typically the asymmetry of these spectra is shown, corresponding to the common definition of the X-ray magnetic dichroism signal. Because the technique is element sensitive, the XMCD signature is characteristic of a particular element.

3.6.2 Magneto Optic Kerr Effect technique

Magneto Optic Kerr Effect (MOKE) measurements were performed at L-NESS in longitudinal configuration and using the polarization modulation technique: a photoelastic modulator, working at a frequency of 50 kHz, has been employed in order to increase the signal-to-noise ratio.

MOKE consists in the analysis of the reflected light from a ferromagnetic sample. The incident light (usually generated by a laser diode) is linearly polarized, in (p polarization) or out (s polarization) of the plane of scattering . The reflected light is analyzed through a polarizer placed before a photodiode. As we will see a modulation-demodulation technique is necessary in order to extract a low signal from an intense background (some volts).

In general MOKE is sensitive to the measurement of the three components of the magnetization vector, but in the contest of this thesis we performed only measurement of the x component of the magnetization vector (longitudinal MOKE), which is the most used configuration. The geometry of the system is defined in Fig. 3.6.2a.

The measurement scheme is the standard MOKE configuration as de-

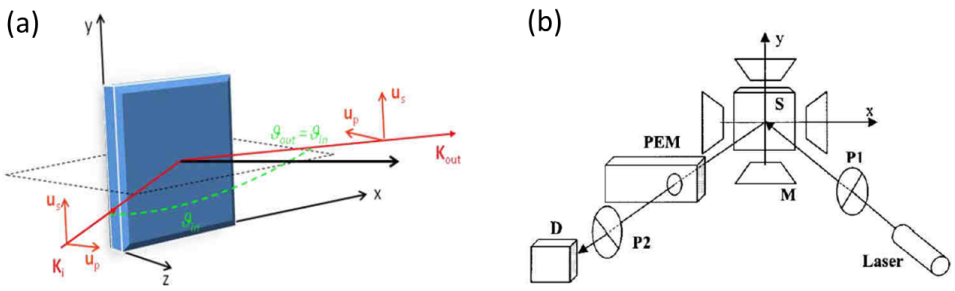

Figure 3.6.2: Scheme of the geometry (a) and apparatus [71] (b) of the MOKE experiment.

scribed by Vavassori [71] and reported in Fig. 3.6.2b. A laser diode generates a collimated light beam that is linearly polarized by polarizer (P1 at 0° or 90° with respect to the optical plane for p or s polarizations) before it's reflected from the sample. After the reflection, it crosses a photoelastic modulator PEM that introduces a controlled oscillation of the phase between p and s components at 50 kHz. After the PEM, a second polarizer (P2 at 45°) is placed as an analyzer before the beam reaches the photodiode. Hence the incident linearly polarized light, formally $E = \begin{pmatrix} p \\ s \end{pmatrix}$, can be seen as the sum of a right circular polarize (RCP) light and a left circular polarized light (LCP) with the same amplitude and phase. When reflected by a magnetized magnetic material the linearly polarized light acquires a Kerr rotation or a Kerr ellipticity which can be measured using the PEM and proper signal demodulation (f or 2f). Magnetic hysteresis loop can be recorded by measuring the Kerr rotation or ellipticity as a function of an external magnetic field applied to the sample. The Kerr amplitude is just the signal difference between positive and negative values at saturation and it's proportional to the magnetization at saturation.

3.6.3 SQUID magnetometry

Measurements of magnetization were performed at the ICMAB with a Superconducting Quantum Interference Device (SQUID) system of Quantum Design. A maximum field of 9 T could be applied and the accessible temper-

atures ranged between 5 K and 300 K. The measurement is carried out by displacing at low frequency the sample along the vertical axis around which two pick-up coils capture the flux variations. These are coupled to a SQUID detector to determine the magnetization up to a resolution of order 10^{-7} emu. It is therefore suitable to study thin films whose signal is at least one order of magnitude higher. However several precautions have to be taken into account to remove the substrate contribution and eventual ferromagnetic impurities.

3.7 Other techniques

3.7.1 First-principles calculations

Theoretical calculations have been performed by S. Picozzi and E. Plekhanov in L'Aquila (Italy).

Density functional theory simulations were performed by using the Vienna Ab initio Simulation Package (VASP) [72]. The ion-electron interaction was treated by means of the projector augmented wave (PAW) potentials. The exchange and correlation terms were considered within the Generalized Gradient Approximation (GGA) in the Perdew–Burke–Ernzerhof (PBE) formalism [73]. We have used an energy cutoff for the plane wave basis as large as 500 eV, a Brillouin zone sampled over the 10x10x1 Monkhorst-Pack k-point mesh [74], while the internal coordinates have been optimized until the forces on all atoms became smaller than 0.02 eV/Å. Finally, GGA+U calculations were performed following Dudarev's formulation [75]. The in-plane lattice constant has been fixed at the experimental value for BTO (a = b = 3.991 Å), while the out of plane one (c) has been chosen in a way so as to minimize the supercell total energy.

Part III

Results

Chapter 4

Magneto-electric coupling at Fe/BTO interface for the E-field control of MTJs

In this chapter we focus on objective 1 of the present thesis: give a contribution to strategy A) (*E-field control of the remanent resistance states of a magnetic tunnel junction (MTJ) by using magnetoelectric coupling (MEC) effects at multiferroic (FE & FM) interfaces*) by shedding light on the physics of MEC at the $Fe/BaTiO_3$ (BTO) fully epitaxial multiferroic interface. In this contest, a possible hybrid MTJ and FE (E-MTJ, Fe/MgO/Fe/BTO) device integrating a multiferroic interface has been fabricated and characterized, too. This knowledge, is of fundamental scientific interest and should be valuable in view of the engineering of multiferroic heterostructures for application in electrically controlled spintronic devices.

In the first part of the chapter the growth and characterization of fully epitaxial Fe/BTO bilayers, subsequently used for MEC studies, are presented (section 4.1). Ferroelectric and structural characterization of BTO films reveal their good ferroelectric properties and high quality of their surfaces, which is fundamental starting point for the growth and the study of epitaxial Fe/BTO interfaces. Structural and chemical characterization of Fe films indicate that Fe grows epitaxially on BTO. However, ultrathin Fe films

(thickness $\leq$ 1 nm) appears to grow on BTO in a three dimensional mode while 2D growth can be achieved only in optimized conditions. This is consistent with the characteristic tendency of metals to form nanoislands at the early stage of growth onto oxides. The Fe/BTO interface is sharp and Fe oxidation is limited to the first atomic layer (FeOx) in chemical contact with the BTO.

In the two following sections we focus on the magnetic and magnetoelectric characterization of the fully epitaxial Fe/BTO system. In particular, in section 4.2 MEC is investigated by Magneto-Optical Kerr Effect and magnetoresistance measurements on magnetic tunnel junctions fabricated on BTO. We find no evidence for strain-mediated MEC mechanism in epitaxial systems, likely due to clamping of BTO to the substrate. Moreover, our results demonstrate the strong localization at the Fe/BTO interface of predicted pure-electronic MEC. In this contest, the hybrid E-MTJ device, Fe/MgO/Fe/BTO, fabricated in geometry MTJ on FE reveals its limits.

In section 4.3 pure electronic MEC is investigated by using ultrathin Fe films in combination with X-ray magnetic circular dichroism and first principles calculations. We find evidence for an undisclosed physical mechanism for interfacial MEC in the Fe/BTO system: magnetization of the interfacial ultrathin oxidized iron layer (FeOx) can be electrically and reversibly switched on-off at room-temperature by reversing the BTO polarization. The suppression / recovery of interfacial ferromagnetism results from the asymmetric effect that ionic displacements in BTO produces on the exchange coupling constants in the adjacent FeOx layer. These results shed light on the physics of MEC at fully epitaxial Fe/BTO interface and holds potential for optimizing interfacial MEC in view of efficient, low-power spintronic devices.

4.1 Growth & characterization of fully epitaxial Fe/BTO

Present section describes the growth and characterization of Fe/BTO bilayers, subsequently used for the study of interfacial magnetoelectric cou-

pling mechanisms. Fully epitaxial Fe/BTO bilayers have been grown on $La_{0.67}Sr_{0.33}MnO_3//SrTiO_3(001)$ (LSMO//STO) or $Nb:SrTiO_3(001)$ (Nb:STO, which stands for conductive 1.0% wt. Nb doped STO single-crystal substrates) in L-NESS in a multichamber system equipped with both PLD and MBE. For more details on the sample preparation system see section 3.1.

Subsection 4.1.1 presents ferroelectric and structural characterization of BTO films. Their good ferroelectric properties and high quality of their surfaces are fundamental starting point for the growth and the study of epitaxial Fe/BTO interfaces. Subsection 4.1.2 focus on the structural and chemical characterization of Fe films grown on BTO. Fe grows epitaxially on BTO. However, ultrathin Fe films (thickness $\leq$ 1 nm) appears to grow on BTO in a three dimensional mode. This is consistent with the characteristic tendency of metals to form nanoislands at the early stage of growth onto oxides. The Fe/BTO interface is sharp and Fe oxidation is limited to the first atomic layer (FeOx) in chemical contact with the BTO.

4.1.1 BTO

BTO films, with thicknesses in the 50 - 150 nm range, have been grown by PLD. Growth conditions are those optimized to obtain epitaxial ferroelectric films with low surface roughness, which is a fundamental requirement in order to obtain high quality Fe/BTO interface. A quadrupled Q-Switched Nd:YAG laser (266 nm), providing pulses 7 ns long with a fluence of 2.2 J/cm^2, has been operated at a repetition frequency of 2 Hz to generate a plasma from a stoichiometric target placed in front of the substrate at a distance of 30 mm. During the growth oxygen pressure in the chamber has been kept at 0.02 Torr and substrate temperature at 640°C. The deposition rate in these conditions is 0.18 Å/pulse, as deduced from RHEED oscillations and confirmed by measuring, by XRR, the thickness of some on-purpose prepared films. After deposition, a post-annealing of 30 min at 600°C in a high oxygen pressure (760 Torr) has been performed in order to avoid oxygen vacancies in the BTO and to improve the surface structural quality.

In order to obtain room temperature high-quality ferroelectric epitaxial

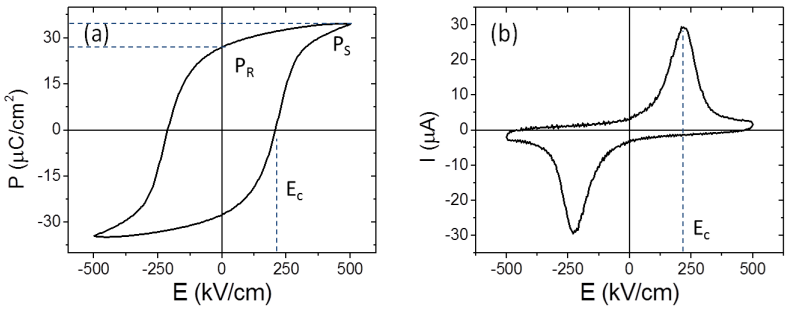

Figure 4.1.1: Ferroelectric loop P-E (a) and I-E (b) for BTO(150 nm)/LSMO(50 nm)//STO(001) sample measured at a frequency of 10 kHz. DLCC compensation technique has been used to subtract the leakage current contribution. BTO shows quite high saturation polarization (P_S is about 35 $\mu C/cm^2$) and remanent polarization (P_R is about 28 $\mu C/cm^2$). The ferroelectric coercive field E_C is about 240 kV/cm.

BTO films, in a first step of this Thesis we have focus on the study and optimization of the growth by PLD of BTO films. In particular we have studied the effect of the substrate temperature on the growth dynamics and dielectric properties of epitaxial BTO films. Extensive details are reported in Ref. [76]. Here we only report the main results. We observed that the optimum growth temperature in order to have ferroelectric BTO films results from a compromise between the need of favoring epitaxy, by promoting the surface diffusion of adatoms (estimated by real-time RHEED analysis), and that of minimizing the re-evaporation of Ba (measured by XPS analysis), which is the most volatile species in BTO. The established correlation between growth dynamics and dielectric properties is a key point for a better understanding of the driving forces relevant in the synthesis of high quality BTO films.

In the following we present the more relevant results of the ferroelectric and structural characterization of the optimized BTO films used subsequently for the Fe/BTO studies.

In Fig. 4.1.1, the results of ferroelectric characterization performed by using top-top configuration on 150 nm thick BTO film grown on LSMO(50 nm)//STO(001) are shown. Extensive details on ferroelectric characterization techniques are given in section 3.4. To perform these measurements Pt

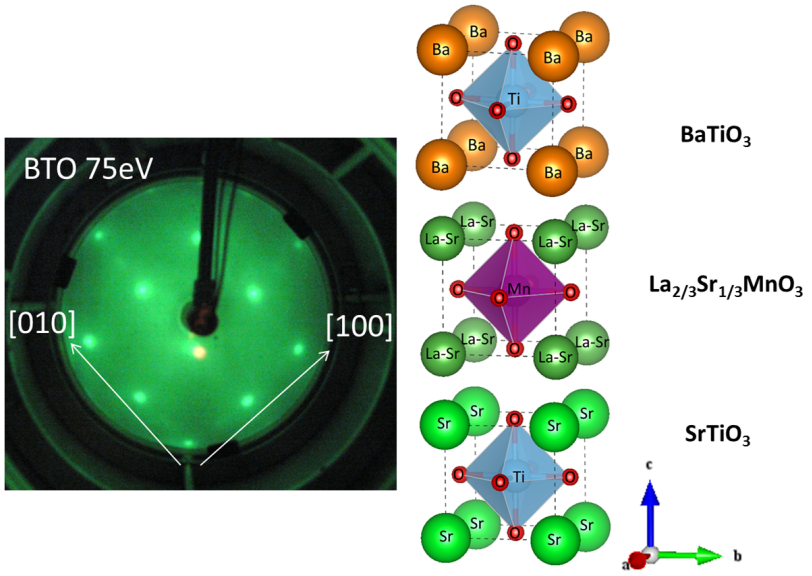

Figure 4.1.2: LEED pattern taken with electron energy of 75 eV on a 150 nm thick BTO film grown on LSMO(50 nm)//STO(001). The (100) and (010) spots correspond to the two side of the STO substrate, so that the epitaxial relationship between BTO and STO is BTO[100]//STO[100], as expected according to the lattice mismatch. On the right, the resulting crystal structure for the full BTO/LSMO/STO stack is shown. The a, b and c axes correspond to the directions STO(100), STO(010) and STO(001), respectively.

contacts (thickness 60 μm; area 0.035 mm^2) have been deposited on the BTO surface ex-situ by sputtering. Ferroelectric loop P-E (panel a) and I-E (panel b) at 10 kHz shows that BTO film is ferroelectric, with quite high saturation polarization (P_S about 35 $\mu C/cm^2$) and remanent polarization (P_R about 28 $\mu C/cm^2$) values. Ferroelectricity of the BTO films represents the starting point for the occurrence of magnetoelectric coupling at Fe/BTO interface.

Moreover, high quality surface is obtained for the BTO films grown with our optimized recipe. Fig. 4.1.2 shows a LEED pattern taken with electron energy of 75 eV on a 150 nm BTO film grown on LSMO(50 nm)//STO(001). The BTO/LSMO bilayer appears to grow epitaxially with cube on cube mode on STO(001) substrates. Note that the (100) and (010) spots in the LEED pattern of BTO (Fig. 4.1.2) lay along the (100) and (010) axis of the

STO substrate, so that the epitaxial relationship between BTO and STO is BTO[100]//STO[100], as expected from the minimization of the elastic energy due to the lattice mismatch and shown in the sketch of Fig. 4.1.2, right panel.

The good ferroelectric properties of BTO films and high quality of their surfaces are a fundamental starting point for the growth and the study of epitaxial Fe/BTO interfaces.

4.1.2 Fe on BTO

Fe films, with thicknesses ranging from 2MLs to 6 nm, have been grown by MBE in UHV conditions, while keeping the substrate at room-temperature. The Fe deposition rate was 0.15 nm/minute, as measured with a quartz microbalance and then checked by in situ XPS. After deposition, the sample has been annealed for 20 minutes at 200 °C in order to improve the structural quality of Fe.

Fe thin films (few nm thick) grow epitaxially on BTO with a well defined cubic structure presenting a 45° rotation with respect to the BTO lattice [77]. Here we only present the more relevant results concerning the structural and chemical characterization of the optimized ultrathin Fe films used subsequently for the study of interfacial magnetoelectric coupling mechanisms.

High quality in our Fe/BTO samples has been proved by electron microscopy observations, performed by M. Varela in Oak Ridge National Laboratory (USA). For more technical details on electron microscopies see subsection 3.3.5. A high-angle annular dark field (HAADF) image, obtained in an aberration corrected scanning transmission electron microscope (STEM), from a [100] oriented slice from a Au(4 nm)/Fe(1 nm)/BTO(150 nm)/LSMO(50 nm)//STO(001) sample, is shown in Fig. 4.1.3a. Brighter spots in the BTO region represent Ba-O columns and indicate that the BTO film is TiO_2 terminated. This can also be appreciated in the chemical color maps in Fig. 4.1.3b, obtained from the electron energy-loss spectroscopy (EELS) analysis of the same interface. The enhanced red signal at the interface in Fig. 4.1.3e confirms the prevalence of the TiO_2 termination. The interfacial chemical

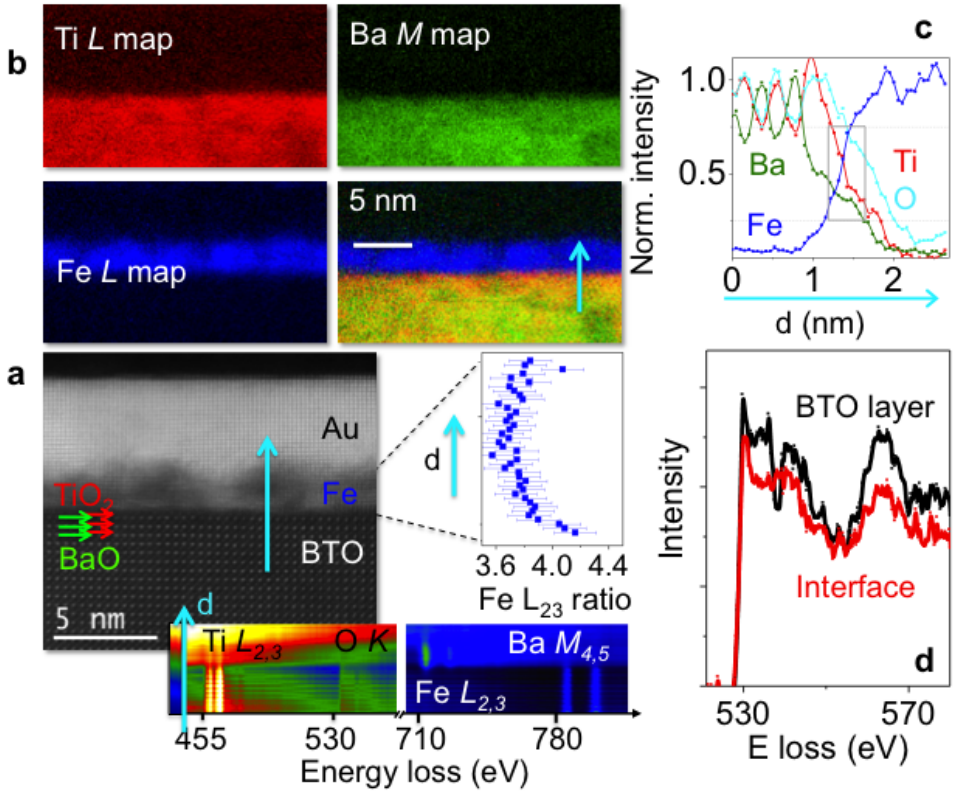

Figure 4.1.3: Electron microscopy analysis of an Au(4 nm)/Fe(1 nm)/BTO(150 nm)/LSMO(50 nm)//STO(001) heterostructure. (a) The atomic resolution Z-contrast image shows the BTO/Fe/Au stacking, with BTO[001]//Fe[001] and Fe[110]//BTO[100]. The BaO (TiO_2) atomic planes near the BTO/Fe interface are marked with green (red) arrows. The EELS linescan acquired along the direction of the blue arrow, including the Ti-$L_{2,3}$, O-K, Fe-$L_{2,3}$ and Ba-$M_{4,5}$ edges across the heterostructure, are shown in the bottom inset. The corresponding Fe-$L_{2,3}$ intensity ratio across the Fe layer (obtained through the second derivative method) are shown in the right panel. Principal component analysis has been used to remove random noise from the linesman. (b) Elemental maps for the BTO/Fe/Au stacking: Fe-$L_{2,3}$ (blue), Ti-$L_{2,3}$ (red), and Ba-$M_{4,5}$ (green). The maps were obtained by integrating a 30 eV wide window under the respective edges of interest after background subtraction using a power law. The RGB overlay of the three maps is also shown (R=Ti, G=Ba, B=Fe). (c) Normalized, elemental profiles obtained from an EELS linescan across the BTO/Fe interface (same color code as in b, O-K (cyan)). The interface is TiO_2 terminated. The signal from the Ti and Fe planes, facing each other, goes down from 75% to 25% of the bulk value within a unit cell (marked with a gray rectangle), when moving across the interface, thus indicating an atomically sharp interface. (d) O-K edge from EELS spectra taken in the BTO bulk (black line) and in the interfacial Fe plane (red).

sharpness can be better appreciated looking at the chemical profiles presented in Fig. 4.1.3c, which shows the normalized integrated intensities corresponding to the O-K (cyan), Ti-$L_{2,3}$ (red), Fe-$L_{2,3}$ (blue) and Ba-$M_{4,5}$ (green) edges. Apart from the evident TiO_2 termination, the signals from Ti and Fe fall down from 75% to 25% of the bulk value within a BTO unit cell, sign of an atomically sharp interface. Interestingly, we detect a significant amount of O beyond the BTO, into the interfacial Fe atomic plane, suggesting some degree of Fe oxidation at the interface plane. Unfortunately, the presence of beam broadening and dechanneling prevent us from being able of accurately determining the stoichiometry of the FeOx interfacial layer, thus we simply refer to it as "oxidized iron" layer (FeOx). But its fingerprints are also present in the fine structure. In the right panel of Fig. 4.1.3a we show the intensity ratio between the L_2 and L_3 components obtained from Fe-$L_{2,3}$ EEL spectra collected when scanning the sample along d, the growth direction (marked with a cyan arrow). It can be appreciated that the $L_{2,3}$ intensity ratio is $\approx$ 3.7 away from the interface but it increases up to ≈ 4.2 at the interface. The $L_{2,3}$ ratio being a measure of the oxidation state of Fe ions, its enhancement signals the formation of an oxide layer confined at the Fe/TiO_2 interface, as reported earlier [78]. Further confirmation of the fact that the increase of $L_{2,3}$ ratio at surface indicates oxidation and not charge accumulation due to screening of BTO surface charges, comes from the analysis of the O-K edge presented in Fig. 4.1.3d. The red curve corresponds to the spectrum taken on the interface, while the black curve has been recorded within the BTO layer. The fine structure of the O-K edge depends directly on the transition metal bonding to the first neighbors. The features corresponding to the perovskite-like fine structure of the black spectrum are smeared on the interface layer, and the appearance of the characteristic peak at $\sim$ 540 eV in the O-K spectrum from the interfacial Fe layer is consistent with the formation of a Fe oxide [79].

Noteworthy, images in Fig. 4.1.3a and Fig. 4.1.3b reveal that even a 1 nm thick Fe layer grows on BTO in a Volmer-Weber, three dimensional mode. This is better seen in the EELS elemental maps of a Au(4 nm)/Co(1 nm)/Fe(2 ML)/BTO(150 nm)/LSMO(50 nm)//STO(001) sample shown in

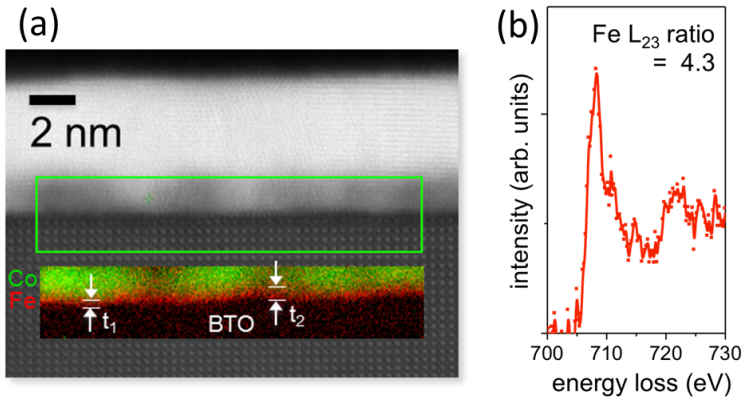

Figure 4.1.4: (a) STEM HAADF image (atomic resolution Z-contrast) and chemical color map in a RG overlay, (Co-$L_{2,3}$ map in green and the Fe-$L_{2,3}$ map in red) from the area marked with a green rectangle, acquired on the actual stack used for experiments: Co(1 nm)/Fe(2 ML)/BTO(150 nm). The island growth mode of the Fe layer on BTO reflects in different thickness for the Fe layer, from ~1 ML (t_1) to ~3-4 ML (t_2). (b) Electron energy loss spectrum taken from interfacial Fe atoms.

Fig. 4.1.4a, where the nominal Fe thickness is 2 ML. The Fe film appears non-uniform, with local thickness ranging from 1 to 4 Fe ML. As TEM averages over the slice thickness, this is consistent with the characteristic tendency of metals to form nanoislands at the early stage of growth onto oxides. Moreover, note that the EEL spectrum taken from the interfacial Fe displays a Fe $L_{2,3}$ intensity ratio of about 4.3 (Figure 4.1.4b). This is fully consistent with the ratio found in the 1 nm thick Fe sample just at the interface with BTO (Figure 4.1.3a) and confirms that in case of just 2 Fe ML samples, Fe atoms strongly interact with BTO and present a clear signature of oxidation.

These results are confirmed and supplemented by recent investigation, by X-ray photoemission spectroscopy and photoelectron diffraction, of the MBE growth of ultrathin Fe films (about 1 nm) on BTO//STO(001) template. This study has been perfomed in order to evidence the influence on morphology, structural order and oxidation of the growth and post-annealing temperatures (T_G and T_{PA}, respectively). No trace of chemical interdiffusion is seen up to the highest post-annealing temperature investigated (400 °C), while a minor Fe oxidation (just one ML confined at the interface) is present,

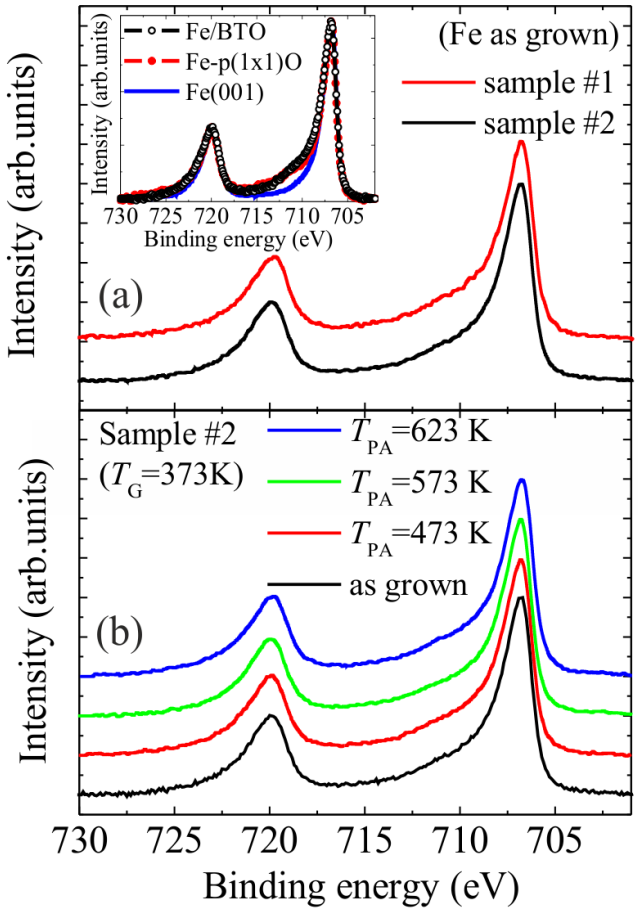

Figure 4.1.5: Fe2p spectrum measured by XPS: a) samples #1 (red line) and #2 (black line) as-grown (at RT and $T_G = 100$°C, respectively); b) sample #2 as-grown (black line) and post-annealed at different temperatures (red, green and blue line). In the inset of panel (a) we report the Fe2p spectrum from sample #2 annealed at 200°C (black empty dots) and two reference spectra obtained from clean Fe(001) (blue curve) and Fe(001)-p(1x1)O surfaces (red full dots), respectively. A Shirley background has been subtracted to all the spectra and the vertical scale has been renormalized in order to have the same peak height for all the spectra.

not affected neither by the growth nor by the post-annealing temperatures (Figure 4.1.5). Our results clearly point to the high robustness and chemical stability of the Fe/BTO interface, intrinsically including one ML of oxidized Fe, which is an essential ingredient for its exploitation within devices based on interfacial magneto-electric coupling effects. Moreover, we found that the optimal conditions for obtaining 2D films are: i) keeping the substrate at 100°C during Fe deposition; ii) performing a post-annealing of the sample for 20 minutes at 200°C. Larger post-annealing temperatures lead instead to film roughening, but the local ordering, as checked by XPD, improves when the post-annealing temperature increases and clustering takes place.

Summarizing, Fe grows epitaxially on BTO with a well defined cubic structure presenting a 45° rotation with respect to the BTO lattice. However, ultrathin Fe films (thickness $\leq$ 1 nm) appears to grow on BTO in a three dimensional mode while 2D growth can be achieved only in optimized conditions. This is consistent with the characteristic tendency of metals to form nanoislands at the early stage of growth onto oxides. The Fe/BTO interface is sharp and Fe oxidation is limited to the first atomic layer (FeOx) in chemical contact with the BTO. Our results clearly point to the high robustness and chemical stability of the Fe/BTO interface. This knowledge is of fundamental importance in view of the studying of magnetoelectric coupling mechanisms taking place at this same interface.

4.2 Absence of strain mediated MEC and failure of the hybrid "MTJ on FE" E-MTJ geometry

In this section, interfacial MEC in the fully epitaxial Fe/BTO system described in previous section is investigated by MOKE and magnetoresistance measurements on magnetic tunnel junctions fabricated on BTO. In particular, in first subsection (4.2.1) by means of MOKE technique we show that, in case of fully epitaxial Fe/BTO heterostructures grown on crystalline templates, no coercivity or magnetic anisotropy changes are detected. This

demonstrates that strain-mediated MEC, previously seen on Fe films grown on BTO single crystal, are suppressed most probably by clamping to the substrate. In the following subsection (4.2.2), magnetoresistance measurements of a E-MTJ multiferroic device (Fe/MgO/Fe magnetic tunnel junction on BTO film) also do not display any sizable ME effect taking place in the Fe film (3 nm thick) in contact with BTO. This is coherent with the absence of strain-mediated coupling but also confirms that predicted direct MEC mechanisms at the Fe/BTO interface are strongly localized and cannot propagate to the upper interface with MgO, which is the relevant one for spin dependent tunneling. This results give a first experimental evidence of the absence of strain-mediated MEC at fully epitaxial Fe/BTO interface and reveal the limits of the hybrid "MTJ on FE" E-MTJ multiferroic device geometry.

4.2.1 MOKE

MOKE experiments have been performed on epitaxial Au(3 nm)/Fe(6 nm)/BTO(50 nm)/LSMO(50 nm)//STO(001) heterostructures. A shadow mask has been used during Au/Fe deposition in order to define macroscopic circular areas with 1 mm diameter. This structure, schematized in figure 4.2.1, allows to perform MOKE experiments under electric-bias conditions. The bias voltage to control the BTO dielectric polarization has been applied between the Au/Fe electrode and the conductive LSMO layer. The laser beam was focused on the same Fe area. In-plane magnetic hysteresis loops have been collected in the longitudinal configuration for different angles (θ) between the applied magnetic field and the BTO[100] direction. Note that this corresponds to the Fe[110] axis since Fe epitaxially grows on BTO with 45° rotation of its cubic lattice with respect to that of BTO, in order to reduce the lattice mismatch (see section 4.1 fro more details). MOKE measurements have been performed using the polarization modulation technique: a photoelastic modulator, working at a frequency of 50 kHz, has been employed in order to increase the signal-to-noise ratio. For each value of θ, loops have been collected under different electric-bias conditions: from -7.5 V up to +7.5 V. Polar plots of the coercive fields collected at RT have thus been obtained

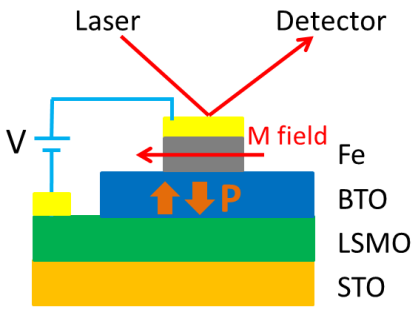

Figure 4.2.1: Layout of the device used for MOKE experiments under electric bias.

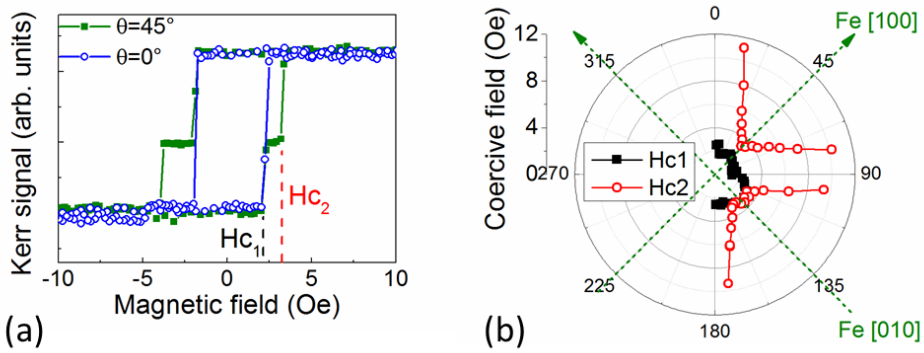

Figure 4.2.2: (a) Magnetization loops measured by MOKE for $\theta = 45°$ and $0°$. (b) Polar plot of the coercive field of LSMO bottom layer (Hc_1) and 6 nm thick Fe top layer (Hc_2) as a function for magnetic field orientation (θ) respect to the [100] axis of BTO, corresponding to the [110] axis of Fe.

for each poling conditions of the FE BTO layer. For more details on MOKE technique see subsection 3.6.2.

In figure 4.2.2(a) we report the characteristic RT MOKE loops obtained for $\theta = 0°$ (empty blue circles in) and $\theta = 45°$ (green full squares). The loop is square for $\theta = 0°$ and becomes stepped at $\theta = 45°$, where two characteristic coercive fields (Hc_1 and Hc_2 for positive fields) appear. Despite the absolute values of Hc_1 and Hc_2 are both compatible with the coercive field of thin single crystal Fe films and the stepped loops could indicate the presence of some uniaxial anisotropy the analysis of the angular dependence of MOKE loops reveals a different scenario. In Figure 4.2.2(b) we present the polar plot

of the two coercive fields (Hc_1 and Hc_2) versus magnetic field orientation θ. The values of Hc_1 are found to be almost constant along all θ directions. On the contrary Hc_2 is strongly dependent on θ: it is minimum at 45° and 135°, and then rapidly increases going toward $\theta = 0°$ (or 180°) and 90°. Surprisingly enough, however, loops at 0° and 90° become squares again, so that Hc_2 cannot be defined. This suggests that our loops can be interpreted as the superposition of two loops. The first one comes from the LSMO bottom electrode; is connected to the coercive field Hc_1 and presents very small anisotropy as expected for manganites [80]. The second loop, instead, arises from the outer Fe electrode and displays the expected fourfold anisotropy, as seen from the evolution of Hc_2. In fact Hc_2 is minimum for 45° and 135°, i.e. for the external field applied along the [100] and [0-10] easy axes of the Fe layer, while it increases when going towards 0° or 90° which would correspond to the Fe hard axes. At 0° and 90°, however, the loop from the Fe layer is no more detectable in this kind of MOKE experiments where we sweep the external field from -10 and +10 Oe. By consequence the loops taken at 0° and 90° simply reflect the LSMO magnetic behavior. From this analysis we can then conclude that the Fe films epitaxially grown on BTO display the expected fourfold anisotropy [81, 77], with easy axes rotated by 45° with respect to the BTO[100] direction, according to the previously established epitaxial relationship.

After investigation of the sample micromagnetic properties for un-poled BTO, we are ready to examine the effect of strain-mediated MEC at the Fe/BTO interface on the Fe magnetic anisotropy and coercivity. Figure 4.2.3 represents the in-plane magnetic hysteresis loops collected at $\theta = 68°$ (where the Fe loop is visible) for un-poled BTO (V^0, black full squares) and BTO polarized up (V^- = -7.5 V, red empty circles) or down (V^+ = +7.5 V, blue empty triangles). No variations in the loops can be detected. The same result is obtained for loops collected along all others investigated θ directions, from 0° to 180°. The absence of any influence of the application of electric fields to the BTO layer on the magnetic anisotropy and coercivity of the Fe layer clearly indicates that strain-mediated ME coupling, previously seen on Fe films grown on BTO crystals [33, 34], is suppressed in the case of fully

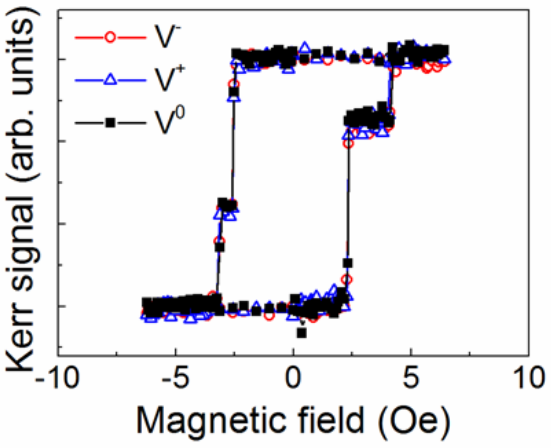

Figure 4.2.3: Magnetization loops, measured by MOKE at $\theta = 68°$, at different BTO bias conditions.

epitaxial Fe/BTO systems clamped by the substrate.

In conclusion, MOKE experiments under electric-bias conditions show no appreciable changes of Fe thin films magnetic anisotropy and coercivity upon reversal of the BTO polarization. This finding indicates that strain-mediated ME coupling is suppressed in fully epitaxial Fe/BTO systems.

4.2.2 Fe/MgO/Fe tunnel junctions on BTO

E-MTJ devices combining magnetic tunnel junction (MTJ) and FE BTO layer have been fabricated using Au(3 nm)/Co(20 nm)/Fe(5 nm)/MgO(3 nm)/Fe(3 nm)/BTO(150 nm)//Nb:STO(001) samples. Note that for this sample an annealing of 40 min at 200°C has been performed after the deposition of the second Fe layer in order to favor the crystallization of the MgO barrier layer. After deposition of the stack, micrometric tunneling junctions (Fe/MgO/Fe), with area ranging from 16 to 1600 μm^2, have been fabricated using optical lithography and ion milling, as described in subsection 3.2.2. This device, schematized in Figure 4.2.4, allows measuring the MTJ for different BTO electric-bias conditions. The voltage to control the FE polarization in the BTO layer has been applied between the bottom Fe layer and the conductive Nb:STO substrate. Tunneling magnetoresistance (TMR) has been

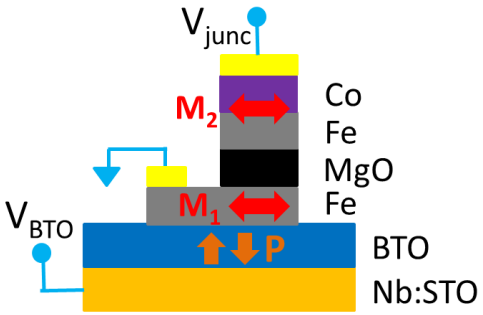

Figure 4.2.4: Layout of a hybrid E-MTJ multiferroic device: a Fe/MgO/Fe MTJ is grown on a FE BTO film.

measured between the top Co/Fe electrode and the bottom Fe layer, which is connected to ground. TMR measurements have been carried out at various temperatures from 50 to 350 K, with the dc four-probe method (for details see section 3.5) and magnetic field applied along both the Fe [100] and [110] axes. TMR curves have been collected for different voltages applied across BTO: from -10 V up to +10 V in ascending steps and then descending back to -10 V.

The basic idea of these devices is that MEC at the interface between the FE layer and one of the FM layers in the MTJ, could be exploited to implement the electric control of the magnetization of said electrode, which correspond to the "electric writing" of the information. The TMR curves shown in Fig. 4.2.5 have been recorded at 150 K for applied field along the [110] Fe and different BTO bias conditions. Curves taken with the field along the [100] Fe direction have been also measured but they are not reported here, because the best magnetization decoupling between the top and bottom layers has been found for field applied along the [110] direction. The low- and high-resistance states are those with parallel (P) and antiparallel (AP) magnetizations with the switching fields corresponding to the different coercivities of the two ferromagnetic electrodes. The top electrode switches at a higher magnetic field than the bottom one, because of the presence of the Co layer. For un-poled BTO (black full squares), the top and bottom Fe electrodes switch at 134 Oe and 28 Oe, respectively, and the TMR, defined as $\frac{R_{AP}-R_P}{R_P} * 100\%$, is about

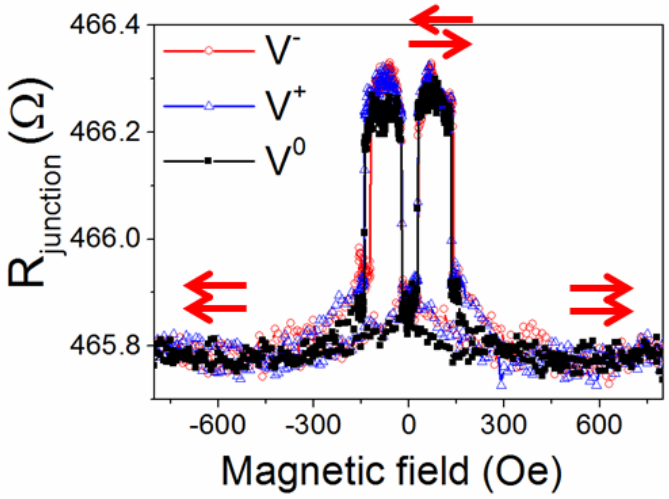

Figure 4.2.5: MR curves measured at 150 K for the Fe/MgO/Fe MTJs at different BTO electric-bias conditions. Magnetic field is applied along the Fe [110] axis.

0.1%. This value, very small if compared with giant TMR ratios experimentally found in fully epitaxial Fe(001)/MgO(001)/Fe(001) MTJs [82], arises from the very low thickness of the bottom Fe layer (just 3 nm thick) in contact with oxides (BTO and MgO). This thickness was chosen to maximize the possibility to propagate the perturbation from the bottom BTO/Fe interface to the Fe/MgO interface of the same film. However this limited thickness revealed particularly challenging for the lithographic process. Furthermore, to avoid possible oxidation and interdiffusion at the Fe/BTO interface, we have lowered the annealing temperature required for the MgO crystallization down to 200°C, which is well below the optimized temperature for this system [83]. Despite the limited value of TMR obtained in these prototypical devices, the TMR value was quite constant from 150K to 300K, and the signal to noise ration good enough to investigate any possible variation of the TMR upon BTO polarization.

The magnetic coercive fields corresponding to the jumps in the resistance seen in Fig. 4.2.5 do not become significantly different once BTO is polarized. In particular the coercive field of the bottom Fe electrode in contact with BTO (that corresponding to the inner jumps in Fig. 4.2.5) does not change

at all. It stay fixes at 28 Oe both for V^- = -10 V and V^+ = +10 V. The minor changes seen on the switching magnetic fields for the top Fe layer hardened by the Co overlayer (140 Oe for V^- = -10 V (red empty circles) and 134 Oe for V^+ = +10 V (blue empty triangles) are not reproducible and can be ascribed to some instability of the micromagnetic configuration. This confirms the absence of any change in the bottom Fe layer magnetic anisotropy or coercivity induced by BTO polarization reversal. In agreement with MOKE experiments shown in previous subsection, our TMR data show that strain-mediated ME coupling is suppressed in the case of fully epitaxial Fe/BTO systems clamped by the substrate. On the contrary, TMR becomes slightly bigger once the BTO is polarized. An increase of $\sim$ 13% (calculated as $\frac{TMR_{V\pm}-TMR_{V0}}{TMR_{V0}} * 100\%$) is observed at both V^- and V^+, as shown in fig. 4.2.5. However, as the observed phenomenon does not depend on the sign of the applied voltage (i.e. on the direction of the BTO polarization), we cannot rule out spurious effect, such as heating due to the application of static voltages across the BTO during TMR measurements. At any rate, the limited entity of the effect we measured is in good agreement with the picture of pure-electronic MEC occurring at the Fe/BTO interface. Indeed, theoretical studies predicted a variation of the magnetic properties of the Fe within just the first atomic layers in contact with BTO (see chapter 2.1 for more details). Our results confirm that any possible MEC, such as that experimentally seen by Garcia et al. [35], cannot propagate up to the upper Fe/MgO interface which plays a crucial role in the spin dependent tunneling.

In conclusion, no sizable variations of the magnetic coercive fields or of the TMR have been detected upon reversal of the polarization on the BTO layer in contact with the Fe bottom electrode of the tunneling junctions. Magnetoresistance measurements demonstrate the absence of sizable strain-mediated effect and also the strong localization at the Fe/BTO interface of predicted pure-electronic MEC. These results thus indicate that pure electronic MEC is the route of choice to be explored for achieving the electrical writing of information in epitaxial ferromagnet-ferroelectric heterostructures. Moreover, the device geometry must be compatible with the strong interfacial localization of these effects, as in the case of Fe/BTO/LSMO MTJs [35],

where the Fe layer in contact with BTO is that directly involved in tunneling.

4.3 Electrical on-off switching of magnetism at the Fe/BTO interface

In order to probe pure electronic (direct) MEC mechanisms at the Fe/BTO interface we used ultrathin Fe films in combination with X-ray magnetic circular dichroism (XMCD) and first principles calculations. We fabricated some capacitors on epitaxial Au(4 nm)/Co(1 nm)/Fe(2 ML)/BTO(150 nm)/LSMO(50 nm)//STO(001) (Au/Co/Fe/BTO) heterostructures, where the limited thickness of the Fe layer allows XMCD probing just the Fe interfacial properties and Co is intended to stabilize ferromagnetism at room temperature. STEM-EELS analysis of these very same samples (shown in section 4.1, Fig. 4.1.4), in fact, indicate that such thin Fe layers (2 ML) appear non-uniform. This observation is of relevance as these Fe nanoislands are expected to be superparamagnetic and justifies the use of a thin Co capping to stabilize the ferromagnetic behavior of thin Fe layers (2 ML), as required for subsequent XMCD experiments. Capacitors were fabricated according to a layout suitable for top-top FE measurements and XMCD under electric-bias condition (Fig. 4.3.1a, for more details on device design and fabrication process see chapter 3.2.1). In the top-top configuration two BTO capacitors are connected in series through the conducting LSMO electrode.

Figure 4.3.1b shows the RT P(E) loop (black line) using positive up negative down (PUND) technique (black line) with delay time of 1 ms, which indicates a coercive field $E_C \approx$150 kV/cm and a remanent polarization of $\sim$ 10 $\mu C/cm^2$. In the same figure the loop "in remanence" made of the blue and red curves corresponds to distinct positive-up (PU) and negative-down (ND) measurements, each of them carried out after pre-polarization by a -5 V and +5 V pulse (1 s), respectively, and a waiting time of 100 s (for more details on FE characterization techniques see chapter 3.4). The fact that the two loops are almost identical indicates that the remanent switchable charge is still 10 $\mu C/cm^2$ 100 s after application of the pre-polarization pulse, while

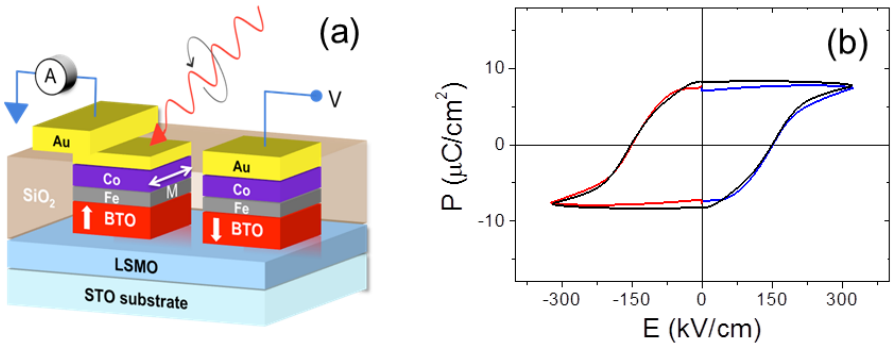

Figure 4.3.1: (a) Layout of the capacitors used for FE characterization and XMCD measurements under electric-bias condition. (b) Characteristic P(E) loops of Au/Co/Fe(2 ML)/BTO/LSMO//STO microcapacitors with $A_1 = 0.02\ mm^2$ area recorded at room temperature in top-top configuration in "standard" PUND measurements (black line) and distinct PU–ND measurements carried out 100 s after application of the same negative and positive pre-pulses used in XMCD measurements (blue-red line).

sizable depolarization takes place over much longer times. Dielectric characterization data have been collected also at 80 K, showing the expected increase of the coercive field. These informations are extremely usefull for the full comprehension of the experimental results.

XAS and XMCD experiments have been performed at APE beamline in ELETTRA synchrotron radiation source in Trieste (Italy) both at room temperature and at 80 K. XAS spectra of the $L_{2,3}$ edge of Fe and Co have been collected in total electron yield (TEY), for a fixed light helicity (σ^+ and σ^-) and magnetization direction (m^+ and m^-) as sketched in Fig. 4.3.1. For more details on XAS and XMCD experiments see subsection 3.6.1. A single photon-energy sweep took about 100 s, which is compatible with an almost full retention of polarization (see above). An observed decrease of the XMCD signals has been observed only over longer times, on the order of tens of minutes, so that our procedure of poling the sample before each scan ensures that experiments are performed at constant dielectric polarization of BTO.

In Fig. 4.3.2a we show the XAS Fe-$L_{2,3}$ spectra taken at RT on Au/Co/Fe/BTO capacitors after polarizing BTO with $V^+ = +5$V (E = 170kV/cm) (P_{up}).

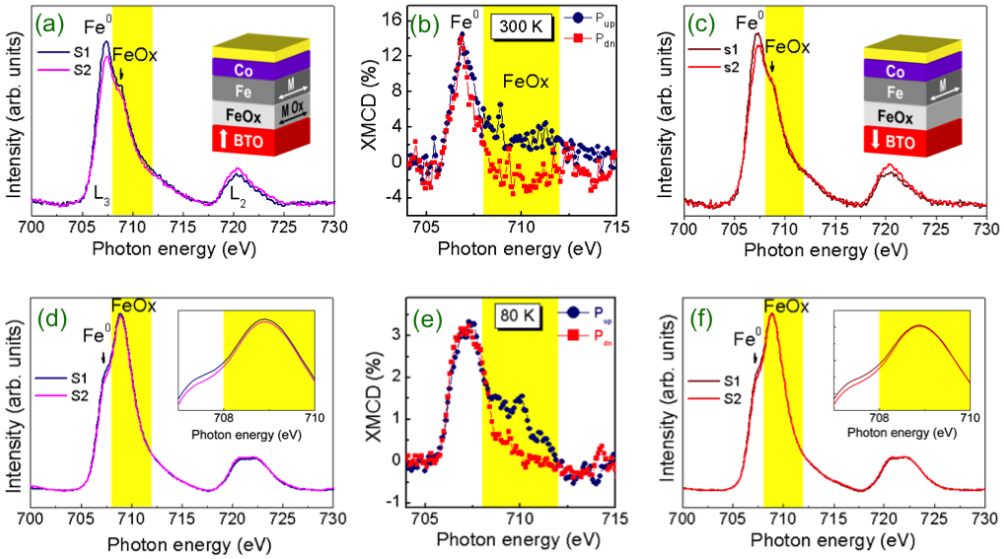

Figure 4.3.2: (a,c) [d,f] XAS Fe-$L_{2,3}$ spectra taken at room temperature on Au/Co/Fe(2ML)/BTO/LSMO//STO capacitors with $A_1 = 0.02\ mm^2$ area at 300 K [$A_2 = 1\ mm^2$, at 80 K] after polarization of BTO with $V^+ = +5$V (E = +170 kV/cm) (P_{up}) and $V^- =$ -5V (P_{dn}) respectively. Insets in (a) and (c) are visual schemes of the Fe/BTO interface for P_{up} and P_{dn}: white vertical arrows correspond to BTO polarization direction, while M and MOx indicate the net magnetization in metallic Fe and in the FeOx layer at the Fe/BTO interface. Insets in d) and f) are zooms of the Fe-L_3 energy region. (b,e) XMCD signal in the Fe-L_3 energy region for BTO polarization P_{up} (blue circles) or P_{dn} (red squares) taken on capacitors with area A_1 at 300 K and area A_2 at 80K, respectively.

Spectrum labeled S1 (S2) corresponds to the addition of spectra collected with (σ^+, m^+) and (σ^-, m^-) ((σ^+, m^-) and (σ^-, m^+)). The prominent L_3 edge is constituted by a main component at 707.4 eV, corresponding to metallic Fe^0, and a shoulder appearing at higher energy ($\sim$ 709 eV, vertical arrow) indicating a distinguishable oxidized Fe^{m+} state [84, 85]. XAS data fully confirm the EELS data of subsection 4.1.2 and assess the existence of an interfacial oxidized iron layer, corresponding to Fe atoms in chemical interaction with BTO. Note that as the crystal field and atomic environment of Fe atoms in this oxidized layer, sandwiched between BTO and metallic iron, are completely different from any of the well known bulk Fe oxides, we simply refer to it as "oxidized iron" layer (FeOx). We will focus on the L_3 edge where the intensity is higher and background subtraction less critical. The difference of S1 and S2 spectra (Figure 4.3.2b), normalized to the sum of their maximum at L_3, is the XMCD, which shows the expected prominent dichroic signal at the Fe^0 edge at 707.4 eV, but also a perceptible dichroism at the FeOx feature ($\sim$ 709 eV). It is clear that both Fe^0 and FeOx edges contribute to the XMCD thus signaling the presence of some net magnetization also in the FeOx layer, as indicated in the sketch in Fig. 4.3.2a(inset).

In Fig. 4.3.2c we show the corresponding XAS Fe-$L_{2,3}$ spectra taken on the same sample after polarization of BTO with V^- = -5 V (P_{dn}). Whereas S1 and S2 spectra largely differ at the Fe0 edge, this difference disappears at the FeOx edge ($\sim$ 709 eV, black arrow). This is better seen in Fig. 4.3.2b, where the XMCD data for P_{dn} (red squares) are plotted. The comparison between XMCD for P_{up} and P_{dn} in Fig. 4.3.2b clearly shows that the dichroic signal of FeOx has been suppressed for P_{dn}. It thus follows that whereas for P_{up} the FeOx interface has a remanent magnetization, this is not the case for P_{dn} which induces the transition of FeOx into either a non-magnetic or antiferromagnetic state, as sketched in Fig. 4.3.2c(inset). This switching is fully reversible, as we repeatedly measured similar spectra by subsequently switching the BTO polarization. Furthermore, the differences of XMCD between P_{up} and P_{dn} become negligible when the samples are allowed to depolarize before XAS measurements, thus confirming that the magnetic switching is related to the dielectric polarization. Finally, note that XMCD

signal is proportional to the projection of the magnetization $\vec{M}$ along the direction of the incoming photon wave vector $\vec{k}$. Therefore XMCD = 0 would occur also in magnetic materials, if $\vec{M}$ were perpendicular to $\vec{k}$. However, in the used experimental set-up, $\vec{k}$ was set at 45^{o} from the sample normal, and we don't expect $\vec{M}$ to be at 90^{o} from $\vec{k}$, due to shape and magneto-crystalline anisotropy.

In Fig. 4.3.2d and 4.3.2f we show the XAS Fe-$L_{2,3}$ spectra taken at 80 K on a different Au/Co/Fe/BTO sample after polarizing BTO with V^+ (P_{up}) and V^- (P_{dn}) respectively. In these large area capacitors ($A_2 = 1\ mm^2$), measurements at RT were prevented by the large leakage current in BTO. The FE coercive filed is higher at 80 K than at RT, but the application of $\pm$ 5 V still results in a sizable enough switching of BTO charges to detect the magnetic ordering switching. The relative weight of the Fe^0 and FeOx components differs, compared to sample of Figs. 4.3.2(a-c), most probably due to a slightly different actual coverage which results in a different degree of interfacial oxidation. However, of relevance here are the differences of XMCD obtained for P_{up} and P_{dn}, as emphasized in Fig. 4.3.2e. In full agreement with data collected at room temperature on sample of Fig. 4.3.2(a-c), the dichroic signal of FeOx is largely suppressed for P_{dn}.

Being the XMCD proportional to the magnetization, data in Figs. 4.3.2(a-f) demonstrate that the magnetization of the interfacial FeOx can be electrically switched on and off by reversing the polarization of BTO. Whereas electro-induced $Fe^{0/m+}$ redox-oxidation process and concomitant changes of the relative weight of the FM (Fe^0) portion of the film at interfaces between metallic alloys and oxide surfaces have been reported [86], we stress that in the present case magnetization switching occurs at FeOx layer without noticeable change of the oxidation state within the Fe film.

We are facing a completely new mechanism for MEC, where the magnetic ordering of just interfacial Fe atoms is deeply affected while "bulk" metallic Fe atoms preserve their FM behavior. This is in analogy with other recent findings on peculiar interfacial magnetic properties at Fe/oxides interfaces [87]. To shed light on this dramatic magnetic reordering, S. Picozzi and E. Plekhanov in L'Aquila (Italy) performed first principles density functional

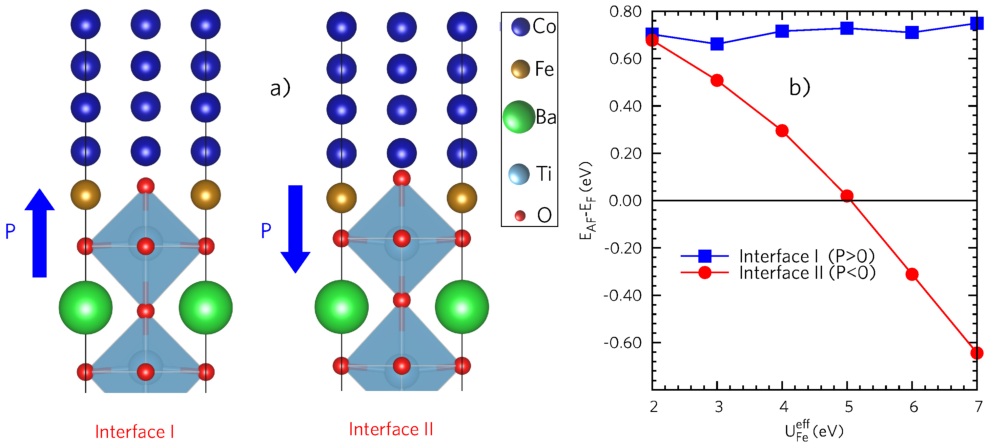

Figure 4.3.3: (a) Schematic plots of the simulated interface regions. From top to bottom: Co layer (blue spheres), FeO layer (light brown and red spheres for Fe and O, respectively) and BTO layer (green, light blue and red spheres denote Ba, Ti and O respectively). The left (right) panel shows interface I (II), in which the polarization P_{up} (P_{dn}) is pointing away from (towards) the BTO layer, respectively. b) Total energy changes (in eV and per unit cell) for FM and AF spin configurations of the interface Fe atoms, as a function of the Hubbard U parameter within the DFT+U approach. Spin flips are carried out at interface I and II (see blue squares and red circles, respectively).

calculations (see section 3.7.1 for technical details). We simulated a supercell built by aligning the [100] axis of the TiO_2-terminated BTO and the [110] axis of bct cobalt sandwiching (i) a single interfacial FeO layer and (ii) 1 FeO ML in contact with BTO, covered by 1 ML of "metallic" Fe in contact with Co. Due to the higher complexity of the analysis of exchange coupling constants in case (ii) and to the fact that case (i) is not unrealistic in our system, we mainly present here results obtained for a single monolayer of FeO. The case (ii) of 2 Fe ML, corresponding to the nominal coverage used for the XMCD experiments,can be found elsewhere. However, we anticipate that the main results presented here for 1 ML hold true also for the 2 ML case. We used a Co(9 ML) overlayer and the thickness of BTO (8,5 ML) was chosen to ensure a bulk-like P in the middle of the layer. In Fig. 4.3.3a we show the reconstructed Co/FeO/TiO_2 interfaces for P_{up} (interface I) and P_{dn} (interface II). For comparison, we also performed calculations for a "non-oxidized" Fe-layer, i.e. using a Co/Fe/BTO supercell stacking (similar to Fe/BTO interface considered by Duan et al. [26]) aiming to consider the two limiting extreme cases: a "fully oxidized" case (FeO layer) and a "fully metallic" (or "non-oxidized") case (Fe layer). The GGA+U scheme was adopted to describe the d-electrons in Fe and Co. Since the optimal value of U is in general unknown, we allowed $U \equiv U_{Fe} - J_{Fe}$ in the FeO layer to change in a wide range (U$\in$[2:7] eV), while we kept $U_{Co} - J_{Co}$ fixed at 2 eV for Co metallic layers. In Fig. 4.3.3b, we plot the energy difference of the FeO interface with ferromagnetic (FM) and antiferromagnetic (AF) spin order, the latter corresponding to reversing the spin direction of one of the two non-equivalent Fe atoms at the interface. As shown in Fig. 4.3.3b, at U$\sim$5 eV, the FeO interface corresponding to P_{dn} turns to be AF, while the FeO interface for P_{up} remains FM; this effect is enhanced by further increasing U. These results show the tendency of the system towards a change in the magnetic order according to the sign of the BTO polarization. For the metallic Fe layer in Co/Fe/BTO, a strong FM exchange interaction stabilizes the FM order and precludes any switch to an AF ground-state upon polarization inversion. For Co/FeO/BTO heterostructures, we estimated the exchange coupling constants J_{FeFe} for nearest neighbor Fe spins as function

of U, by mapping our DFT total energies to a simplified Heisenberg model. Consistent with data in Fig. 4.3.3b, we found that J_{FeFe} (U) weakens and has a sign inversion from FM to AF at U $\sim$ 3 eV, becoming more AF upon increasing U. The modulation of the magnetic properties of the FeO layer, namely the switch from FM to AF character when switching the polarization of the BTO, results from the polarization-induced atomic-position shifts and subsequent modifications of the Fe-O bond topology when interfaced with the TiO_2 surface of BTO. The major bond reconfiguration concerns the coupling between the two non-equivalent Fe atoms, which is indeed mediated by the oxygen atom in the underlying TiO_2 plane. As shown in Figure 4.3.4, the position of the latter is severely affected when switching polarization, thus leading to a large increase in the Fe-O(TiO_2)-Fe angle (from 96.7 up to 112.3 degrees) at interface II (P_{dn}) with respect to interface I (P_{up}). Correspondingly, also the Fe-O(TiO_2) bond length suffers from a sizable reduction (from 2.67 to 2.40 Å). As superexchange Fe-O-Fe interactions are known to be extremely sensitive to bond angle and bond distances, it is quite reasonable to guess that one of the two interfaces can develop a different magnetic order, in agreement with total energy DFT calculations. The presence of the FM Co layer tends to favor a FM order of the neighboring FeOx layer, thus explaining why the AF order is only achieved at relatively large U. Indeed, the transition towards antiferromagnetism at interface II in the exchange coupling J_{FeFe} occurs at smaller values of U with respect to the total energy (U $>$ 3 eV). As for the local electronic structure, we do not observe sizable changes within the FeO layer upon polarization reversal. The Fe magnetic moments are always around 3.5 Bohr magnetons, and only a slight increase of the exchange splitting in the PDOS of the flipped Fe atoms is seen in the AF configuration for interface II (P_{dn}), in agreement with the total energy decrease stabilizing AF in this case.

As anticipated above, simulations performed on 2 ML of Fe on BTO display the same trend, i.e. the stabilization of the AF order at high U for interface II accompanied by a major bond reconfiguration driven by polarization reversal. This is a strong indication of the robustness of the DFT analysis as well as of the proposed mechanism for the switching of the magnetic order.

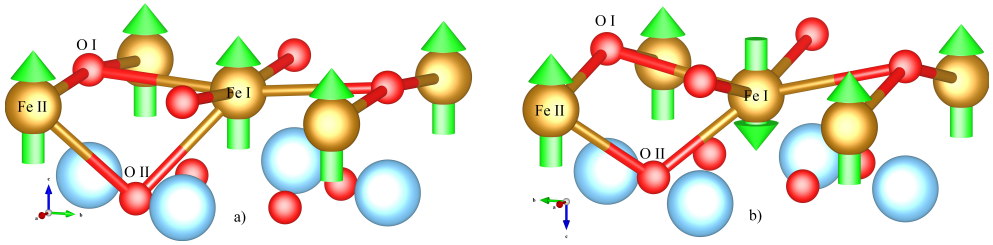

Figure 4.3.4: Details of the interface for the Ferromagnetic (a – Interface I) and Antiferromagnetic (b – Interface II) configurations of 1 ML system. The FE polarization points in the direction of c-axis, upwards and downwards for the (a) and (b) configurations, respectively.

Note that our results represent a step forward with respect to pioneering calculations performed by Fechner et al. [88] for an oxidized ultrathin Fe-layer on BTO. Although in a rather different geometry (i.e. without Co-capping layer) and in different interfacial atomic configurations, those calculations showed FM coupling in the absence of electronic correlations (i.e. within a bare local-spin-density approximation, LSDA). We here demonstrated that the inclusion of "beyond-LSDA/GGA" approaches (such as DFT+U) dramatically affects the magnetic coupling and it is therefore required to achieve an accurate description of magnetoelectricity at the Fe/BTO interface. The weakening of the ferromagnetic interaction at high U for interface II (P_{dn}) is fully coherent with the disappearance of XMCD from the interfacial FeOx layer for P_{dn}. Depending on the strength of correlation effects, we could expect AF coupling or simply a weakening of exchange constants leading to a lowering of the interfacial Curie temperature below the minimum temperature of our experiments (80K). A more detailed investigation of the magnetic ordering of the “off” magnetic state, for instance by X-ray linear dichroism, would be needed in order to elucidate if the “non-magnetic” state is either paramagnetic or AF, but this is definitely beyond the scope of this work.

To summarize, we have demonstrated a novel physical mechanism for interfacial MEC leading to a RT electrical and reversible on/off switching of the interfacial Fe magnetization in the Fe/BTO heterostructure. DFT+U calculations have shown that the FeO/BTO interfaces are dramatically asymmetric with respect to the polarization of BTO: whereas the interface with P_{dn}

can undergo a magnetic transition towards an antiferromagnetic (or paramagnetic) state, the P_{up} interface remains robustly FM. At variance with previous works dealing with MEC driven by bond reconfiguration [26], we propose here a completely new mechanism based on the induced change of magnetic order, not simply on the change of the interfacial magnetic moments. As the magnetization of the FM layers corresponds to about 3.5 $\mu_B/atom$, switching on/off the magnetization at E_C leads to a record value of the surface magnetoelectric coefficient $\alpha_s \approx 2x10^{-9} Gcm^2/V$. This value exceeds previous predictions of MEC at Fe interfaces based on bond-reconfiguration [26] and the spin-dependent screening mechanism [27] by one and four orders of magnitude respectively. Finally let us estimate the energy consumption for the switching of the magnetic ordering via reversal of the polarization. For a device constituted by a FM electrode of 50 nm diameter and BTO thickness of 15 nm, the switching of the polarization at E_C would require about $0.7x10^{-16}$ J. This is of the same order of magnitude of the energy consumption reported in the case of inducing coherent magnetization switching via voltage pulses assisted by external magnetic fields [20, 21] and 1/500 times lower than that required for writing information via spin-current-injection [19]. This confirms the great potential of the peculiar mechanism for MEC here disclosed to achieve a reversible, fully electrical writing of the magnetic information in spintronic devices, such as MTJs, where the surface magnetization plays a major role. However the device geometry must be compatible with the strong interfacial localization of these effects, as in the case of Fe/BTO/LSMO MFTJs [35], where the Fe layer in contact with BTO is that directly involved in tunneling.

Chapter 5

FTJs displaying TER effect

In this chapter we focus on objective 2 of the present thesis: give a contribution to strategy B) (*E-field control of the remanent resistance states of a tunnel junction with FE barrier (FTJ) displaying TER effect*).

In the first part of the chapter (section 5.1) fabrication and characterization of micron-sized Pt / $BaTiO_3$ / $La_{0.7}Sr_{0.3}MnO_3$ FTJs is presented. In these pure FE TJs (without engineered interfaces) we demonstrate the room temperature E-field control of the remanent resistance states, with TER ratio up to 10^4%.

In the second part of the chapter (5.2), aiming to develop barriers of adjustable width and thus enhance the TER ratio, materials displaying E-field induced metal-insulator transition (half-doped manganites $La_{0.5}A_{0.5}MnO_3$, A = Ca/Sr) have been developed and integrated in epitaxial FE/half-doped manganite heterostructures. We have thus firstly explored the role of strain on half-doped manganites magnetic and transport properties, revealing a different sensitivity of the two manganites ($La_{0.5}A_{0.5}MnO_3$, A = Ca/Sr) to strain and E-field effects (subsection 5.2.2). Finally Pt / $La_{0.5}A_{0.5}MnO_3$ / $BaTiO_3$ / $La_{0.7}Sr_{0.3}MnO_3$ tunnel heterostructures have been grown and processed into devices for TER measurements. Preliminary experiments performed at room temperature are presented in subsection 5.2.3.

5.1 Electroresistance in pure FE TJs: Pt / BTO / LSMO

In this first section we fabricate and characterize micron-sized pure FE tunnel junctions intended to be reference devices for the study of the engineered ferroelectric tunnel junctions (FTJs) employing half-doped manganites.

FTJs were fabricated on Pt(22 nm)/BTO(2-4 nm)/LSMO(30 nm) (LSMO stays for $La_{0.67}Sr_{0.33}MnO_3$) heterostructures grown on (001) - oriented $SrTiO_3$ (STO) single crystal substrates. The oxide bilayers were epitaxially grown by pulsed laser deposition at ICMAB. LSMO3 films were deposited at 725°C in 0.2 mbar oxygen pressure, BTO films at 700°C in 0.02 mbar oxygen pressure, with subsequent free cooling in 100 mbar oxygen pressure. The growth rate, for both films, was calibrated by measuring, by X-ray Reflectivity (XRR), the thickness of some on-purpose prepared films. Laser fluence was verified to be constant for all growth processes. Three samples were grown with BTO barrier layer thickness 2 nm, 3 nm and 4 nm, respectively. The metallic Pt layers were deposited ex-situ at room temperature by sputtering. After deposition of the stacks, micrometric tunneling junctions, with area A ranging from 4 to 900 μm^2, were fabricated at LNESS using optical lithography, as described in subsection 3.2.2. A schematic diagram of the FTJ device geometry is shown in Figure 5.1.1.

The electrical measurements of the junctions were performed in two-probe geometry (for details see section 3.5). Positive bias corresponds to current flow from the top to the bottom electrode. The ferroelectric polarization of the BTO barrier layer was switched by manually applying poling voltages V_{write} about 0.5 s long with a Keithley 2611. All resistances reported here are resistance values (R= V/I) at V = 100 mV extracted from I-V curves (from -0.2 V to 0.2 V, step 0.002 V) recorded with the same Keithley 2611 after the poling voltage pulse V_{write} was removed. All the measurements were performed at room temperature.

I-V curves were collected upon polarizing BTO barrier layer with positive or negative V_{write} pulses, corresponding to the ferroelectric polarization of BTO pointing down (P_{dn}) or up (P_{up}) respectively. Figures 5.1.2a and 5.1.2b

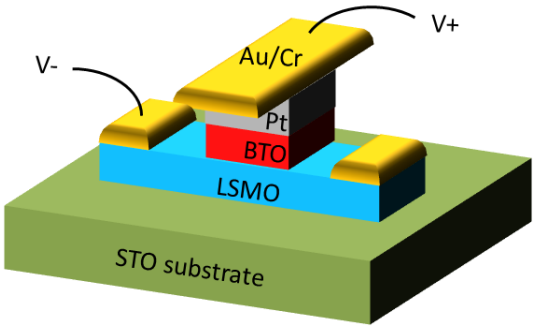

Figure 5.1.1: A schematic diagram of the FTJ device geometry.

show I-V curves in P_{up} and P_{dn} states (violet and orange lines, respectively) of two representative Pt/BTO/LSMO FTJs with BTO ferroelectric barrier layer thickness of 2 nm and 4 nm, respectively. I-V characteristics are highly nonlinear in both P_{up} and P_{dn} states, as expected for tunneling transport regime. Moreover, the junction resistance per area product (R*A) increases exponentially with BTO barrier thickness (Figure 5.1.2d), as expected for tunneling through BTO. These results indicate that transport in our micron-sized BTO-based junctions at RT is dominated by tunneling. Note that R*A values displayed in figure 5.1.2d are average values obtained considering all the measured junctions for each sample (up to 36); and that R*A values of the single junctions do not show any dependence on the junction area A.

Figure 5.1.2 also suggests that electrons tunneling through the ferroelectric BTO barrier are transmitted differently depending on the direction of the polarization. I-V curves measured upon poling FE BTO barrier reveal a resistance difference between the positively (P_{dn}) or negatively (P_{up}) poled junctions. The junctions are in a high-resistance state (OFF) when large enough positive V_{write} is applied to polarize the BTO downward (P_{dn}), and switches to a low-resistance state (ON) when ferroelectric polarization is reversed by large enough negative V_{write} (P_{up}). As shown in Fig. 5.1.2d the resistance contrast increases dramatically by increasing the BTO thickness. The non-volatile resistance switching in Pt/BTO/LSMO//STO is demonstrated by the clear hysteretic variation of the tunneling resistance obtained for all the junctions and shown in figures 5.1.3b and 5.1.3c for the same two

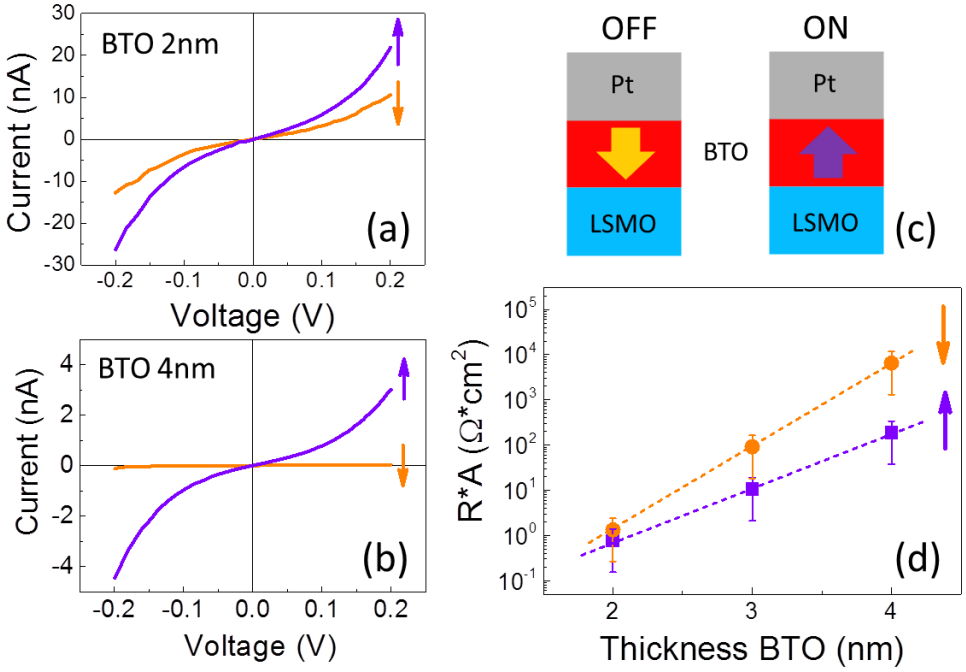

Figure 5.1.2: (a) ((b)) ON and OFF room temperature I-V curves (violet and orange lines, respectively) of a Pt/BTO/LSMO FTJ with BTO thickness 2 nm (4 nm) and junction area A = 25 μm^2 (60 μm^2). (c) Schematic representation of the ferroelectric polarization state of the BTO barrier (P_{dn} and P_{up}) corresponding to the OFF and ON state of the FTJ, respectively. (d) Average junction resistance (at 100 mV) per area product R*A as a function of BTO barrier thickness. An exponential increase is found, as expected for direct tunneling.

representative junctions of figure 5.1.2 with BTO barrier thickness 2 and 4 nm, respectively. To obtain these loops a testing pulse train (Figure 5.1.3a) composed of V_{write} pulses (black rectangles, about 0.5 s long) following a triangular profile was applied to the junctions. After each writing pulse, an I(V) curve (represented by red circles) was recorded to read the corresponding resistance R of the junctions. Positive pulses set the device to the high-resistance (OFF) state by driving the polarization to point towards the LSMO bottom electrode, whereas negative pulses switch the device into the low-resistance (ON) state by polarization reversal. We note that the switching from the ON (OFF) state to the OFF (ON) state is relatively sharp, consistent with the observation that the ON (OFF) state resistance is not sensitive to the value of the writing pulses, until the polarization is switched upward (downward). Finally note that V_{write} pulses needed to switch from ON to OFF state (and viceversa) are consistent with ferroelectric coercitive fields of thin BTO films previously reported [61, 60], in agreement with association of the junction resistance switching with the FE polarization switching of the BTO barrier. Indeed, the R loops reported in panels b and c of Fig. 5.1.3 are very similar to FE loops recorded on BTO films.

To quantify the resistance change we define the tunnel electroresistance (TER) ratio, $TER = \frac{R_{OFF}-R_{ON}}{R_{ON}} * 100\%$, where R_{OFF} is the junction resistance in the high resistance state corresponding to BTO ferroelectric polarization pointing towards the LSMO bottom electrode and R_{ON} is the junction resistance in the low resistance state corresponding to BTO ferroelectric polarization pointing towards Pt top electrode. TER ratios of the junctions with different BTO thicknesses are summarized in figure 5.1.4; as can be appreciated, the TER increases exponentially with the BTO film thickness. The ferroelectric polarization has been proposed to influence the tunnel current through changes either in the density of states (DOS) of electrode-barrier interfaces [11] or in the physical parameters of the tunnel barrier (height, thickness, tunneling mass) [43, 44]. As the tunnel transmission depends exponentially on the latter, the observed thickness dependence of the TER suggests that the polarization direction primarily affects the tunnel barrier characteristics rather than the DOS. This result is in agreement with previ-

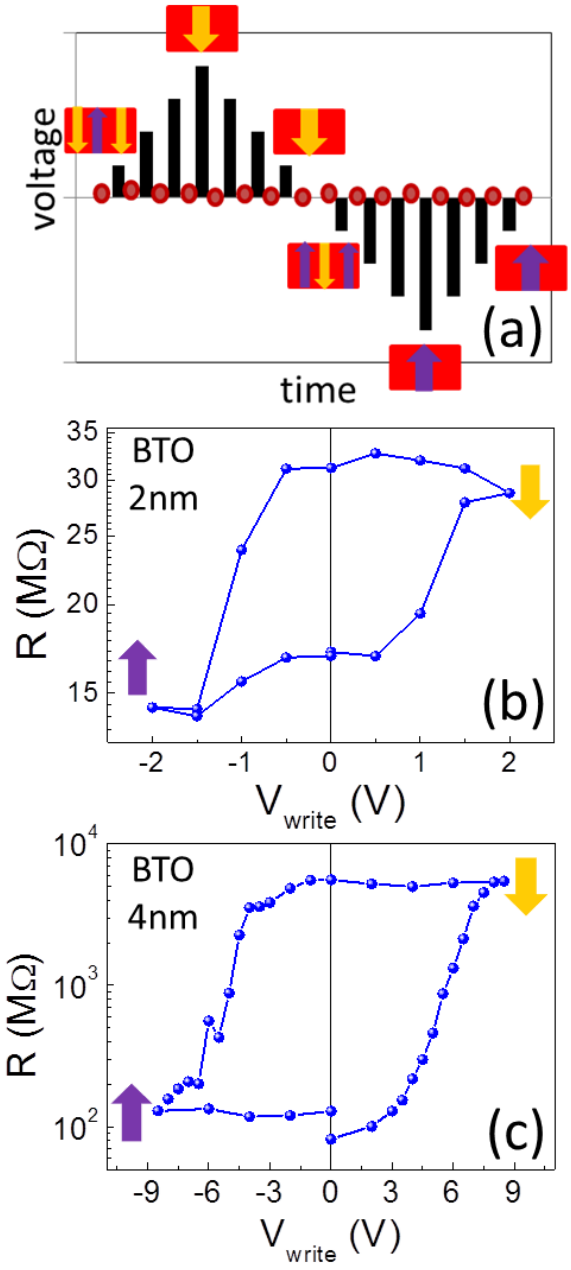

Figure 5.1.3: (a) Testing pulse train composed of V_{write} pulses (black rectangles, about 0.5 s long) following a triangular profile. An I-V curve (red circles), to read the resistance of the junction, follows each V_{write} pulse. (b) ((c)) Resistance hysteresis loop measured using the pulse train shown in (a) for a Pt/BTO/LSMO//STO junction with BTO thickness 2 nm (4 nm) and junction area A = 25 μm^2 (60 μm^2).

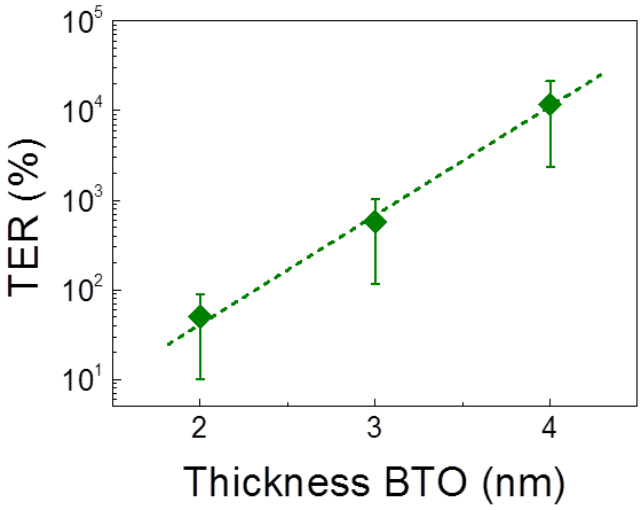

Figure 5.1.4: Average TER ratios as a function of BTO barrier thickness. An exponential increase is found.

ous experimental reports [50] for non-lithographed samples measured using SPM techniques with the conductive tip used as a top electrode in contact with the surface of the ferroelectric layer, thus suggesting that mechanisms governing TER are not influenced neither by lithographic process nor by junctions dimensions. Finally, note that TER ratios achieved in our junctions (up to 10^4%) represent up to now record values for room temperature TER in micron-sized pure FE FTJs without engineered interfaces (Figure 5.1.5), quite one order of magnitude higher than TER ratios (up 10^3%) achieved at room temperature in Pt/BTO/SRO//DSO (SRO stays for $SrRuO_3$) and Co/PZT/LSMO//STO (PZT stays for $PbZr_{0.2}Ti_{0.8}O_3$) FTJs of lateral dimensions in the range of $10^3 \mu m^2$ by Z. Wen et al. [60] and D. Pantel et al. [59], respectively.

Summarizing, we have fabricated micron-sized BTO-based FTJ devices. In these large area devices transport at room temperature is dominated by tunneling. Moreover, FTJs display two remanent resistance states that can be controlled electrically switching FE polarization of the BTO barrier. Mechanisms governing the TER in these micron-sized junctions seem to be the same reported previously for non-lithographed samples measured using SPM techniques with the conductive tip used as a top electrode in contact

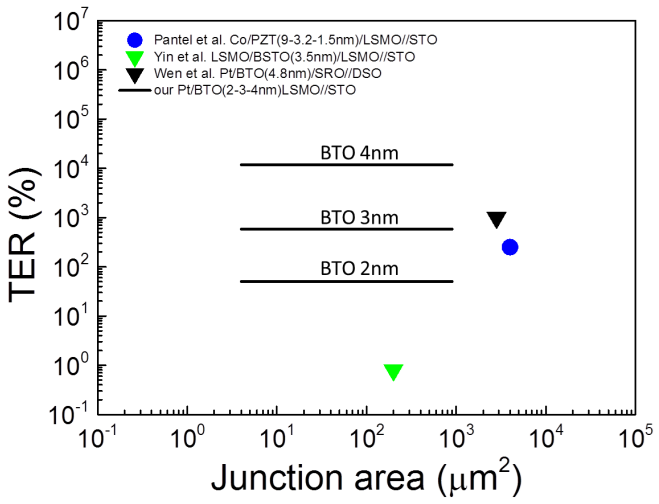

Figure 5.1.5: Comparison between TER ratios, at room temperature, reported so far for micron-sized FTJs [64, 65, 60] and our results (black lines) for Pt/BTO/LSMO junctions with BTO thickness of 2, 3 and 4 nm, respectively.

with the surface of the ferroelectric layer. Finally we underline that TER ratios achieved in our pure FE junctions (up to 10^4%) represent up to now record values for room temperature TER in micron-sized FTJs without engineered interfaces.

5.2 Development of engineered FTJs: Pt / HD / BTO / LSMO

5.2.1 Introduction & materials selection

In this second section, aiming to develop engineered barriers of tunable width and thus enhance the TER ratio, materials displaying E-field induced metal-insulator transition (half-doped manganites $La_{0.5}A_{0.5}MnO_3$, A = Ca/Sr) have been developed and integrated in epitaxial FE/half-doped manganite heterostructures.

Half-doped (HD) manganites $La_{0.5}A_{0.5}MnO_3$ (A = Sr/Ca), due to their position close to the ferromagnetic-metallic (FM-M) / antiferromagnetic-

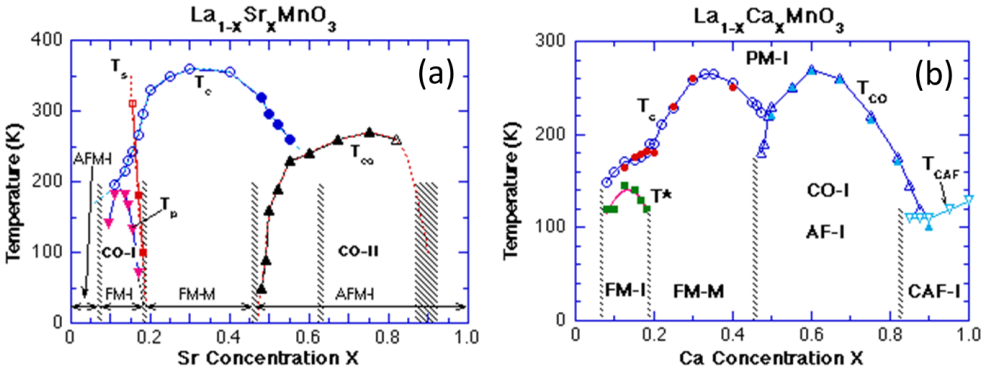

Figure 5.2.1: Phase diagram of $La_{1-x}Sr_xMnO_3$ (a) and $La_{1-x}Ca_xMnO_3$ (b) [89, 90].

insulating (AF-I) transition in the phase diagram of $La_xA_{1-x}MnO_3$ manganites (Figure 5.2.1), are intrinsically highly sensitive to external perturbations, such as electric and magnetic fields or strain. This makes them very appealing for the realization of devices, such as tunneling junctions, where the externally induced phase transition can result in giant variation of macroscopic magnetic or transport properties.

In addition to explicit chemical doping, carrier concentration can also be modulated electrostatically, opening the possibility to dramatically alter the electronic properties [91], and hence complex oxides such as $La_{1-x}Sr_xMnO_3$ have been the subject of intense investigation in regard to the ferroelectric control of magnetism (see Ref. [15] for a review). At the interface of $La_{1-x}A_xMnO_3$ (A = Sr/Ca) with a ferroelectric material, polarization charges on the ferroelectric side of the interface are screened by charges with opposite sign on the manganite side, effectively altering the hole concentration, corresponding to the x value in the stoichiometry, near the interface [92, 93]. If the manganite has chemical composition x close to a phase boundary, then the reversal of polarization can induce a transition locally near the interface. Burton and Tsymbal [46] recently showed from first-principles calculations that the change in magnetic order around x $\sim$0.5, discussed above, can be induced by polarization switching at the manganite-ferroelectric interface. Furthermore, the same authors predicted that in a FTJ with such a magnetoelectrically active interface, switching of the ferroelectric barrier

is expected to change the "perpendicular metallicity" of the interface of the HD manganite electrode, effectively changing the tunneling barrier thickness, and leading to a giant change in conductance [47]. Experimentally, a very recent paper demonstrates a significant enhancement of tunnel electroresistance (TER) for temperatures below 180 K in ferroelectric tunnel junctions consisting of $BaTiO_3$ tunneling barriers and $La_{0.7}Sr_{0.3}MnO_3$ electrodes when a nanometer thick $La_{0.5}Ca_{0.5}MnO_3$ interlayer is inserted at one of the interfaces [62].

The structures investigated in the present thesis are shown in figure 5.2.2. The HD manganite $La_{0.5}Sr_{0.5}MnO_3$ (LSMO5) and $La_{0.5}Ca_{0.5}MnO_3$ (LCMO5) layers are chosen specifically at the boundary between the FM-M ($x < 0.5$) and the AF-I phase ($x > 0.5$). For ferroelectric polarization pointing towards the thin HD layer (Figure 5.2.2, right), the electron accumulation or hole depletion induced to screen the polarization is expected to push the doping level of the HD manganite towards the $x < 0.5$ FM-M phase. At the other interface of the BTO barrier, the optimally doped LSMO (i.e. $La_{0.7}Sr_{0.3}MnO_3$) has a stoichiometry that is far enough from the phase boundary and a change in magnetic order is not expected owing to the accumulation of screening charge. On the other hand, for polarization pointing away from the HD manganite layer (Figure 5.2.2, left), the hole accumulation biases the interface towards the $x > 0.5$ side of the phase boundary, that is, towards the AF-I phase. Such a magnetoelectrically induced metal-insulator transition in the HD manganite would effectively increase the tunneling barrier thickness, thereby leading to an exponential enhancement of the junction resistance, and hence to an overall enhancement of the TER effect compared to the case of pure FE Pt/BTO/LSMO FTJs (section 5.1).

There is another important factor that has to be taken into account when we integrate HD manganites thin films in FTJs: the role of strain. It is well known that in manganites, the magnetic and the orbital degrees of freedom are strongly coupled. This coupling allows the control of the orbital order by applying a magnetic field, but the reverse process is also possible: magnetic order can be indirectly controlled, via orbital order, by the lattice distortion. One noticeable example is the drastic modification of the ground state of the

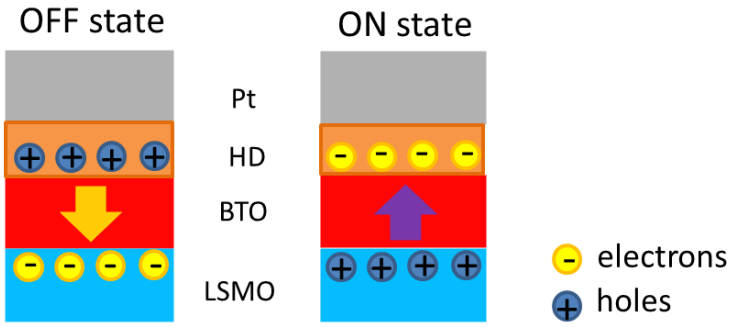

Figure 5.2.2: Schematic demonstration of screening charge accumulation in electrodes for opposite ferroelectric polarization orientations in the BTO layer for Pt/HD/BTO/LSMO FTJs.

large conduction bandwidth (W_0) LSMO5 obtained by Konishi et al. [94] by growing thin films on different substrates and so controlling the tetragonality (c/a, where (a, c) are the in-plane and out-of-plane unit cell parameters respectively). By changing c/a only from 1.04 (in-plane compressive strain, $\varepsilon < 0$) to 0.98 (in-plane tensile strain, $\varepsilon > 0$), the LSMO5 follows a sequence of different ground states: from the insulating and antiferromagnetic C-type AF, to the metallic and ferromagnetic F-FM and finally to an in-plane conducting and antiferromagnetic A-type AF phase, in good agreement with the phase diagram obtained by first-principles band-structure calculations [95, 96]. Still the question if the A-AF phase remains stable and metallic under larger tensile strain (c/a < 0.98), which is expected to promote the narrowing of the quasi-2D conduction band, remains open.

In contrast to LSMO5, calculations of the effect of tetragonal distortion c/a on phase diagram of narrower W_0 oxides, such as LCMO5, are not yet available, most likely due to the existence of complex charge ordering (CO) and electronic phase separation (PS) phenomena, lengthy discussed in literature [95, 97, 90], here favored by the bandwidth narrowing induced by the smaller Ca^{2+} ions at A-sites in the $La_{0.5}A_{0.5}MnO_3$ perovskite. In brief, upon cooling, bulk LCMO5 undergoes first a paramagnetic to FM transition and, at lower temperature, a simultaneous AF and CO transition. Experimentally, strain effects on LCMO5 thin films are much less known. LCMO5 films on

different substrates have been reported [98, 99, 100] and there is consensus that PS occurs and, maybe not so surprisingly, properties of films are found to strongly vary depending on growth conditions and thickness. However, a systematic study of strain effects on magnetic and transport properties on LCMO5 films is still lacking.

It is thus clear that strain can have a profound effect on phase diagram of manganites films. Moreover, in adjustable FTJs the piezoresponse and polarization surface-charges of the ferroelectric layer both can contribute to modify the properties of the adjacent HD manganite layer and thus those of the tunnel barrier. Progress in this direction and discrimination between strain and field-effects in FE/HD heterostructures require detailed understanding of the epitaxial strain effects on the properties of HD manganite ultrathin films.

In next subsection (5.2.2) we present the results of the investigation of the effect of strain on the magnetic and transport properties of HD manganite thin films LSMO5 and LCMO5. Then (subsection 5.2.3) we present some preliminary results concerning the realization and characterization of FTJs integrating thin layers of HD manganites (Figure 5.2.2), aiming to exploit their electric field induced phase transition to obtain an overall enhancement of the TER effect compared to the case of pure FE Pt/BTO/LSMO FTJs studied in section 5.1.

5.2.2 Epitaxial thin films of HD manganites: strain effects on magnetic & transport properties

In this subsection, we report on the systematic investigation of the magnetic and transport properties of $La_{0.5}Sr_{0.5}MnO_3$ (LSMO5) and $La_{0.5}Ca_{0.5}MnO_3$ (LCMO5) thin films grown on different substrates ($DyScO_3$, $SrTiO_3$, $(La,Sr)(Al,Ta)O_3$, $LaAlO_3$ and $YAlO_3$) which allows to explore a wide range of structural mismatch and subsequent strain state of the films. Furthermore, the use of two compounds with different conduction bandwidth (W_0 (LSMO5) $>$ W_0 (LCMO5)) allows to study the impact of this parameter on the evolution of the magnetic and transport phase diagram vs. strain. This new knowl-

	LSMO5			LCMO5		
substrate	δ(%)	a_{q-plot} (Å)	$c_{\theta-2\theta}$ (Å)	δ(%)	a_{q-plot} (Å)	$c_{\theta-2\theta}$ (Å)
DSO	+2.13	3.925	3.761	+2.87	3.91	3.733
STO	+1.22	3.907	3.803	+1.96	3.907	3.74
LSAT	+0.31	3.87	3.833	+1.04	3.865	3.77
LAO	-1.71	3.802	3.965	-0.99	3.793	3.88
YAO	-3.58	3.864	3.891	-2.87	3.833	3.90

Table 5.2.1: The calculated mismatch values (δ) and the in-plane (a) and out-of-plane (c) lattice parameters measured by q-plots and θ-2θ scans, respectively, for LSMO5 and LCMO5 films grown on five different substrates. Data LSMO5 on LSAT, which cannot be evaluated from the θ-2θ scan, have been estimated by assuming a full in-plane strain and assuming unit cell conservation.

edge is valuable in view of the engineering of heterostructures involving HD manganites for application in oxide electronics devices.

Thin films of LSMO5 and LCMO5, 20 nm thick, were epitaxially grown by PLD at ICMAB on (001) - oriented single-crystalline substrates (a pseudo-cubic notation is used for those which are not cubic): (a) $DyScO_3$ (abbreviated hereafter as DSO, lattice constant of 3.940 Å), (b) $SrTiO_3$ (STO, 3.905 Å), (c) $(La,Sr)(Al,Ta)O_3$ (LSAT, 3.870 Å), (d) $LaAlO_3$ (LAO, 3.792 Å), (e) $YAlO_3$ (YAO, 3.720 Å). For LSMO5 (3.858 Å) the mismatch values referred to bulk compounds, $\delta = (a_{substrate} - a_{manganite})/a_{manganite}$ x 100%, are: +2.13% (DSO), +1.22% (STO), +0.31% (LSAT), -1.71% (LAO) and -3.58% (YAO). For LCMO5 films (3.830 Å) the mismatch values δ are: +2.87% (DSO), +1.96% (STO), +1.04% (LSAT), -0.99% (LAO) and -2.87% (YAO). Mismatch values for LSMO5 and LCMO5 on different substrates are summarized in Table 5.2.1. The films have been deposited at 725°C in 0.2 mbar oxygen pressure with subsequent free cooling in 100 mbar oxygen pressure.

Figure 5.2.3(a) and (b) show the θ-2θ XRD pattern around the (002) reflections of LSMO5 and LCMO5 films grown on all used substrates, respectively. The substrates (002) reflections are identified by vertical lines and by the corresponding name of the substrate. Solid vertical lines (purple) indicate the position of the (002) reflections of LSMO5 and LCMO5 films

and the dashed vertical lines indicate the position of the bulk (002) LSMO5 or LCMO5 peaks. Broader angular range scans do not show any reflection different than (00l) thus indicating that films are fully c-axis textured. In most cases (except films on YAO) the Laue fringes are well visible indicating excellent films planarity and constant thickness. Horizontal arrows in Figs. 5.2.3(a,b) emphasize the shift between the measured position of the peaks of LSMO5 and LCMO5 films and the corresponding bulk positions which reflects the strain state of the films. As shown in Fig. 5.2.3(a), LSMO5 on YAO and LAO films have the (002) reflections at lower 2θ angles than bulk LSMO5; this indicates an out-of-plane expansion as expected from the lattice mismatch ($\delta < 0$) imposing a compressive in-plane stress. On the contrary, in LSMO5 on STO and DSO, the (002) reflections occur at higher 2θ angles than bulk LSMO5; this indicates a shrinking of the out-of-plane cell parameter, in agreement with the lattice mismatch ($\delta > 0$) imposing a tensile in-plane stress. In the case of LSMO5 on LSAT, the (002) reflection of the film overlaps with the (002) reflection of the substrate as expected from their small mismatch. Note that the position of the (002) peak from LSMO5 film on YAO is very close to the bulk one, while from the mismatch value (δ = -3.58%) it should occur at lower angle than that of the film of LSMO5 on LAO (δ = -1.71%). This observation indicates that LSMO5 on YAO is almost relaxed.

Overall, data for LCMO5 films on the different substrates (Fig. 5.2.3(b)) show the same trends. However, remarkable difference exists: as the unit cell of bulk LCMO5 is smaller than that of LSMO5, the stress-compressed films are less compressed and the tensile-stressed films are more tensile strained. The calculated out-of-plane lattice constants from these XRD data ($c_{\theta-2\theta}$) are included in Table 5.2.1. The data for LSMO5 on LSAT, which cannot be evaluated from the θ-2θ scan, has been estimated by assuming a full in-plane strain and assuming unit cell conservation.

To determine the in-plane cell parameters, reciprocal space maps around the (113) reflections were collected. In Fig. 5.2.3(c)-(f) we show the maps for the two extreme cases for each manganite: LSMO5 and LCMO5 films on DSO substrate, with in-plane tensile stress, and on YAO substrate, with

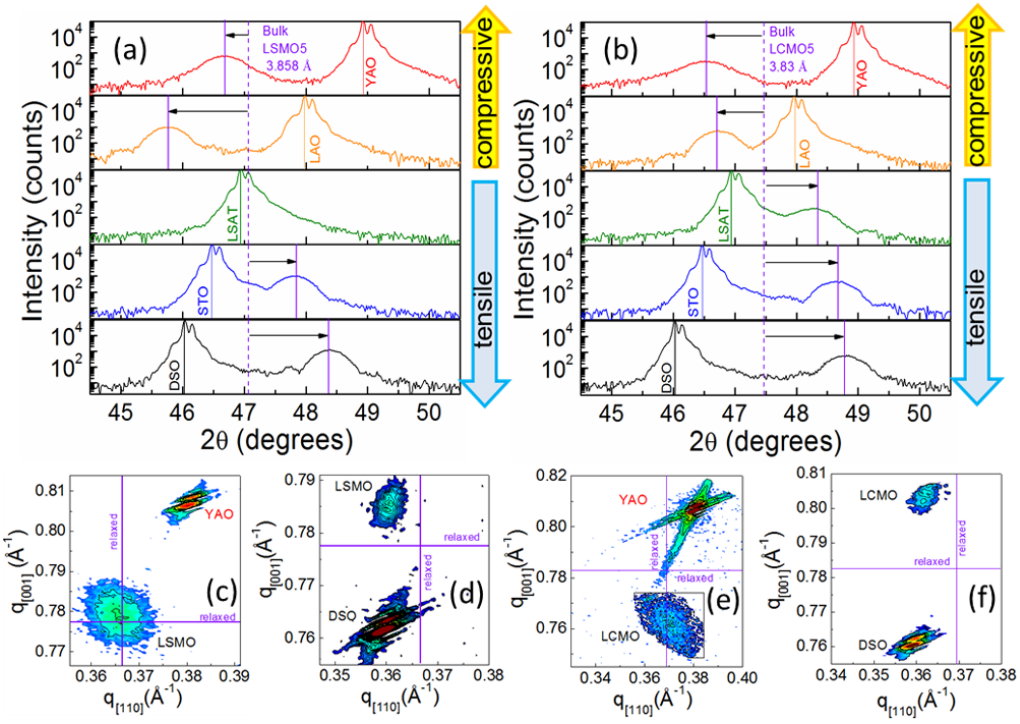

Figure 5.2.3: Top panels: θ-2θ XRD scans of the (002) reflections for LSMO5 (a) and LCMO5 (b) films grown on five different substrates. Bottom panels: reciprocal space maps around (113) reflections for LSMO5 films on YAO (c) and DSO (d) substrates and for LCMO5 films on YAO (e) and DSO (f) substrates.

in-plane compressive stress. In the first case (DSO substrate, Figure 5.2.3(d) and (f)) it can be appreciated that the reflections from the films have $q_{[110]}$ values that roughly coincide with the ones of the substrate and are definitely far from the relaxed position (vertical line), while the $q_{[001]}$ values of the spots from the films and the substrate are quite different. This means that the in-plane lattice constant (a) of the film expands and closely matches that of the substrate, whereas the out-of-plane lattice constant (c) shrinks. In the case of LSMO5 and LCMO5 on YAO (fig. 5.2.3(c) and 5.2.3(e), respectively) the position of the spots of the films are closer to those of the corresponding bulk compounds, indicating lattice relaxation. From the position of the (113) film's reflection we calculated the in-plane (a_{q-plot}) and out-of-plane (c_{q-plot}) lattice parameters. The a_{q-plot} data are included in Table 5.2.1, where we also show the c-parameter arising from θ-2θ scans ($c_{\theta-2\theta}$). Since θ-2θ scans have higher resolution than q-plots in determining out-of-plane cell parameters, we used $c_{\theta-2\theta}$ and a_{q-plot} to calculate the tetragonality ratio c/a and the unit cell volume values ($V_{uc} = (a_{q-plot})^2 c_{\vartheta-2\vartheta}$), shown in Figure 5.2.4. These c/a values reflect the actual strain state of the films and they will be used accordingly, in the following. In Fig. 5.2.4(a) we show the dependence of c/a (left axis, solid symbols) and V_{uc} (right axis, empty symbols) of the epitaxial LSMO5 films on the mismatch with the substrates. The corresponding data for LCMO5 are shown in Fig. 5.2.4(b). We first note that in these 20 nm thick films, the c/a ratio (solid symbols) can be changed from 0.958 to 1.043 for LSMO5 and from 0.954 to 1.023 for LCMO5 films, going, in both cases, from DSO to LAO substrate. Note that for LSMO5 films on YAO, the c/a value is close to the bulk one (c/a $\approx$ 1, unstrained state) as expected from the high mismatch ($\approx$ 3.58 %), and in agreement with this, relaxation is observed in Figs. 5.2.3(c,e). Very small tetragonality (c/a $\sim$ 1) also occurs when the mismatch is very small, as for LSMO5 on LSAT substrates. In the other cases, elongation (c/a $>$ 1) or contraction (c/a $<$ 1) is found when the mismatch is compressive or tensile, respectively. On the other hand, it can be also appreciated that neither for LSMO5 nor for LCMO5, the unit cell volume of the films (empty symbols) is preserved under strain (the corresponding bulk values are indicated by red dashed horizontal lines) but vary with the

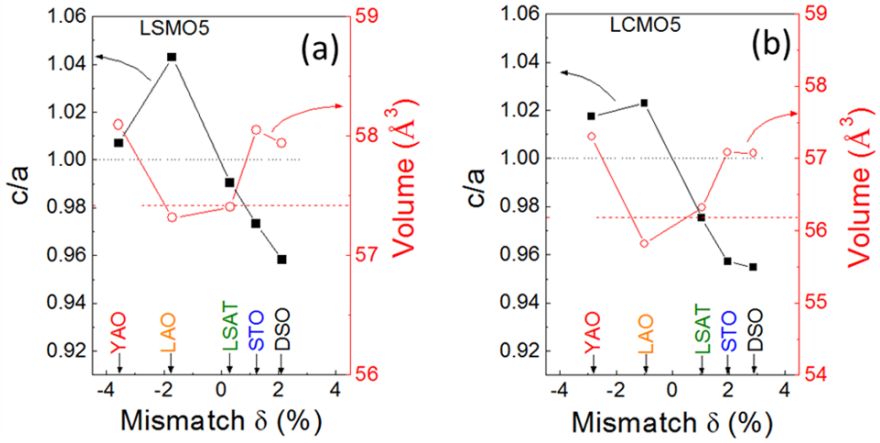

Figure 5.2.4: Dependence of tetragonality ratio c/a (left axis, solid squares) and unit cell volume (right axis, empty circles) values of the epitaxial LSMO5 (a) and LCMO5 (b) films on the structural mismatch imposed by various substrates (YAO, LAO, LSAT, STO and DSO). Dotted and dashed horizontal lines indicate the corresponding bulk values of c/a and volume, respectively.

mismatch. V_{uc} is close to the bulk value for the films with smaller strain (c/a $\approx$ 1) but systematically enlarges upon tensile or compressive epitaxial strain. The very same trend is observed in LSMO5 (Fig. 5.2.4(a)) and LCMO5 (Fig. 5.2.4(b)). These data do not allow to discriminate if this variation reflects a non-volume preserving pure elastic response of the LSMO5 and LCMO5 lattices under strain, or some sort of chemical self-adaptation (i.e. non-stoichiometry, to minimize the strain-related elastic energy), as reported in related oxides [101, 102]. The atomic force microscopy images of all the films indicate a surface roughness of about (or smaller than) a single perovskite unit cell ($\approx$ 0.4 nm) which does not vary significantly by the strain.

Figures 5.2.5(a,b and c) display the temperature-dependent magnetization M(T) (measured in field-cooling conditions (FC) using an in-plane field H = 1kOe), the field-dependent magnetization M(H) (at 50 K) and the in-plane resistivity ρ(T) of the LSMO5 films on different substrates, respectively. Figures 5.2.5(d,e and f) show the corresponding data for LCMO5. In these figures the magnetic data for films on DSO are not included because the strong magnetic contribution of the substrate largely masks the film contri-

bution.

As shown in Figure 5.2.5(a) the LSMO5 film grown on a matching substrate (LSAT (c/a = 0.990, green circles)) displays a FM transition at the Curie temperature (T_C) around 345 K, and a large magnetization (about 400 emu/cm^3) at the lowest temperature which is similar to that reported for bulk LSMO5 [103, 89]. LSMO5 on YAO (c/a = 1.007, red triangles), with a small compressive strain, also displays a similar FM behavior but with a somewhat reduced magnetization ($\approx$ 300 emu/cm^3) and T_C decreased to about 335 K. The low temperature enhancement of magnetization is due to paramagnetic impurities in the YAO substrate. When increasing further the compressive strain, as in LSMO5/LAO (c/a = 1.043, orange stars), the M(T) data shows a severely depressed magnetization ($<$ 50 emu/cm^3) and a peak at about 190 K, which indicates a transition from paramagnetic to antiferromagnetic AF state at the Neel temperature. The tensile strained LSMO5/STO (c/a = 0.973, blue squares) film displays a much suppressed magnetization although a ferromagnetic contribution rise below $T_C \approx$ 285K. The magnetization data of films on DSO (not shown here) are consistent with an antiferromagnetic behavior. The M(H) loops (Fig. 5.2.5(b)) (measurements have been performed at 50 K to minimize the paramagnetic contribution from the substrates) display the same trends as observed in the M(T) data (Fig. 5.2.5(a)), namely a sharp suppression of ferromagnetism by strain.

As shown in Figure 5.2.5(c), the in-plane resistivity ρ(T) is also reflecting the change of the magnetic ground state of LSMO5 under strain. It is clear that films grown on roughly matched substrates (LSMO5/LSAT (c/a = 0.990, green circles)) or quasi-relaxed (LSMO5/YAO (c/a = 1.007, red triangles)) are metallic: resistivity decreases decreasing temperature. This is also true for the film grown on the moderately tensile stressing substrates LSMO5/STO (c/a = 0.973, blue squares). In contrast, a compressive strain (LSMO5/LAO (c/a = 1.043, orange stars)) drive the LSMO5 into an insulating phase, evidenced by the negative ρ(T) slope at 300K. By increasing further the tensile strain (LSMO5/DSO (c/a = 0.958, black rhombi)), ρ(T) displays a rather week temperature dependence, with a metallic-like slightly positive dρ(T)/dT slope down to about 200 K, and a rapid increase at lower

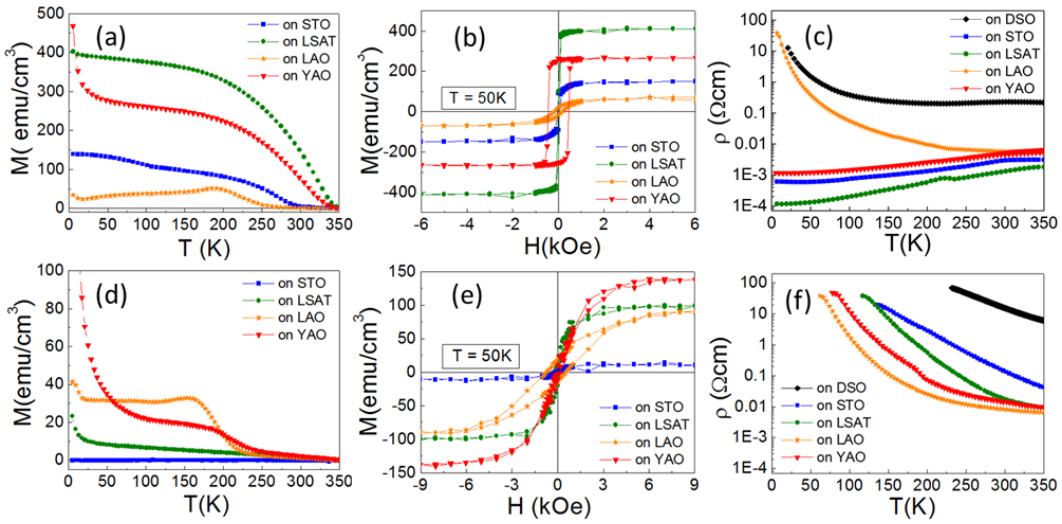

Figure 5.2.5: Temperature-dependent magnetization M(T) (FC conditions; in-plane field H = 1 kOe), field-dependent magnetization M(H) loops (at 50K, H in plane) and temperature-dependent resistivity ρ(T) of the LSMO5 (a,b,c) and LCMO5 (d,e,f) films on different substrates (DSO, STO, LSAT, YAO and LAO), respectively.

temperature. It can also be appreciated in Fig. 5.2.5(c) that the room-temperature resistivity of the LSMO5/DSO film is larger than that of the LSMO5/LAO film. This at first sight puzzling behavior is due to the presence of fracture microcraks in the highly tensile stressed LSMO5/DSO film. The dependencies of the remanent magnetization (at 50K) and resistivity (at 230K) of LSMO5 films on the tetragonality ratio c/a are collected in Figs. 5.2.6(a) and Fig. 5.2.6(b) (black solid squares).

Summarizing, LSMO5 films have FM ground state that shifts towards AF ordering when increasing the tetragonal distortion, either c/a $>$ 1 or c/a $<$ 1. However, it is clear in Figs. 5.2.5(a) and 5.2.5(b) that the transition from FM to AF does not produce a full suppression of magnetization but some ferromagnetic contribution persists in the films. This is fully consistent with a PS scenario where FM/AF phase coexistence is modulated by strain [97]. On the other hand, LSMO5 films, either unstrained or under tensile strain; a compressive strain, instead, produces an insulating ground state.

The LCMO5 films display a very different response. As shown by the

M(T) and M(H) data in Fig. 5.2.5(d) and 5.2.5(e) respectively, all films have a very small magnetization signaling PS with predominant regions in the AF ground state, most noticeable in LCMO5/LAO film (c/a = 1.023, orange stars) where a peak in the magnetization (Fig. 5.2.5(d)) at about 170 K suggests a paramagnetic to AF phase transition; the M(T) plateau at lower temperatures signals the presence of a small FM contribution (about 30 emu/cm^3) while the increase of M(T) for very low temperature is due to the paramagnetic contribution of the LAO substrate. A similar behavior is displayed by LCMO5/YAO (c/a = 1.017, red triangles) in Fig. 5.2.5(d) where we observe a very weak magnetic contribution (about 20 emu/cm^3) and the strong paramagnetic contribution of the YAO substrate. In contrast, the magnetization of LCMO5/STO (c/a = 0.957, blue squares) is negligible indicating a pure AF phase. Figure 5.2.5(e) shows the M(H) loops measured at T = 50 K. These plots confirm the presence of a residual FM phase in the LCMO5 films although the strong paramagnetic substrate contribution does not permit to easily appreciate the trend of M vs strain which is more evident in M(T) data in Figure 5.2.5(d). In summary, all LCMO5 films are AF. Films compressively strained, such as LCMO5/LAO and LCMO5/YAO, display major residual FM contributions, indicative of PS, which are not appreciated in the magnetization response of the films with tensile strain.

The ρ(T) data in Fig. 5.2.5(f), show that LCMO5 films, irrespectively of the substrate, are insulating. Inspection of data in Fig. 5.2.5(f) indicates that the resistivity increases when decreasing c/a: from LAO, c/a = 1.023 in-plane compressive strain, to DSO, c/a = 0.955 in-plane tensile strain.

The overall trends in magnetization (at 50 K) and resistivity (at 230 K) vs. tetragonality of LCMO5 films are better seen in Figs. 5.2.6(a) and 5.2.6(b) (red empty symbols). When comparing the magnetic and transport results obtained for LSMO5 films and for LCMO5 films we can observe that: a) for LSMO5 films a compressive strain drives its FM/M ground state towards a PS state with predominance of AF/I regions, whereas tensile strains promote the formation of AF/M regions, and b) for LCMO5 films, the ground state is AF/I and strain does not change it. The existence of FM PS-regions in LCMO5 films is more evident in films under compressive strain. Probably

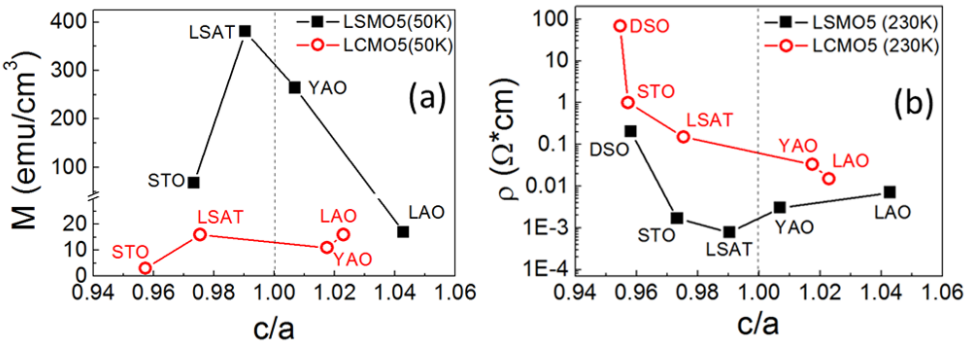

Figure 5.2.6: Dependencies of the (a) remanent magnetization (at 50K), extracted from M(H) loops, and (b) resistivity (at 230K), extracted from ρ(T) curves, for LSMO5 (solid squares) and LCMO5 (empty circles) films, respectively, on the tetragonality ratio c/a.

this is also the reason why the resistivity of these films is lower than that of their tensile-strained counterpartners.

In conclusion, we have performed a study of epitaxial strain on thin films of HD manganites $La_{0.5}Sr_{0.5}MnO_3$ (LSMO5) and $La_{0.5}Ca_{0.5}MnO_3$ (LCMO5) on a variety of substrates. It is found that epitaxial strain imposed by the substrates promotes pseudo-tetragonal cells with c/a ratio that can be largely tuned: $0.958 < \text{c/a} < 1.04$ (LSMO5) and $0.954 < \text{c/a} < 1.023$ (LCMO5). The ground state of bulk LSMO5 is recovered in thin films grown on well matched substrates, and the corresponding thin films are ferromagnetic and metallic. In contrast, compressive biaxial strain leads to the emergence of an antiferromagnetic insulating state and tensile strain leads to an uncommon antiferromagnetic and metallic (in-plane) phase. The reduced metallicity of LSMO5 upon stronger tensile strain is attributed to the combined effect of conduction band narrowing and the ubiquitous presence of extended planar defects in the film. In the narrower bandwidth LCMO5 oxide, the epitaxial strain imposed by the substrates drives in all cases the films into an AF and insulating state, with minor effects on conductivity or magnetization. It thus follows that strain has remarkably different effects on LSMO5 and LCMO5 that mainly arise from the difference in the electronic bandwidth and the corresponding ground state. Therefore we anticipate that

HD manganites, if integrated on piezoelectric stressors or tunnel junctions in conjunction with ferroelectric layers, will respond differently depending of their bandwidth. For instance, we envisage that field effects should dominate in LCMO5 based barriers whereas piezo-induced strain may have a more prominent role on LSMO5. Although more investigations are needed to definitely settle the microscopic nature of spin and orbital ordering in these films, the findings here reported should help to design more responsive devices, such as multifunctional tunnel barriers with improved response.

5.2.3 TER in Pt/HD/BTO/LSMO TJs: preliminary results and perspectives

In this subsection we present some preliminary results concerning the realization of FTJs integrating thin layers of the HD manganites studied in previous subsection, aiming to exploit their electric field induced phase transition to obtain an overall enhancement of the TER effect compared to the case of pure FE Pt/BTO/LSMO FTJs studied in section 5.1.

FTJs were fabricated on Pt(22 nm)/LSMO5(1-2 nm)/BTO(2-3 nm)/LSMO(30 nm) (LSMO5 stays for $La_{0.5}Sr_{0.5}MnO_3$) and Pt(22 nm)/LCMO5(1-2 nm)/BTO(2-3 nm)/LSMO(30 nm) (LCMO5 stays for $La_{0.5}Ca_{0.5}MnO_3$) heterostructures grown on (001) - oriented $SrTiO_3$ (STO) and $LaAlO_3$ (LAO) single crystal substrates. The oxide trilayers were epitaxially grown by pulsed laser deposition at ICMAB. LSMO, LSMO5 and LCMO5 films were deposited at 725°C in 0.2 mbar oxygen pressure and BTO films at 700°C in 0.02 mbar oxygen pressure. After the trilayer deposition a free cooling in 100 mbar oxygen pressure was performed. The growth rate, for all films, was calibrated by measuring, by X-ray Reflectivity (XRR), the thickness of some on-purpose prepared films. Laser fluence was verified to be constant for all growth processes. Twelve samples were grown combining BTO barrier layer thickness 2 nm and 3 nm, LSMO5 (LCMO5) thickness 1 nm and 2 nm, and STO and LAO substrates (figure 5.2.7). The metallic Pt layers were deposited ex-situ at room temperature by sputtering. After deposition of the stacks, micrometric tunneling junctions, with area A ranging from 4 to 100 μm^2, were

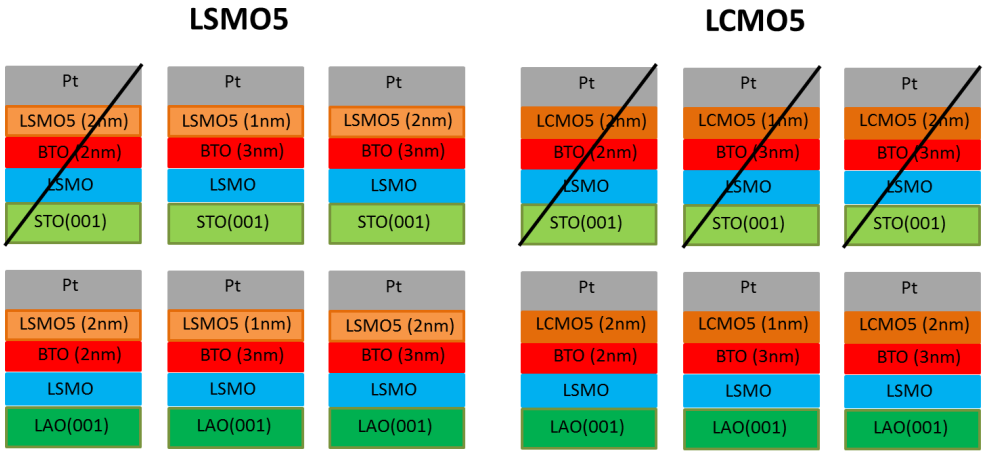

Figure 5.2.7: Sketch of the twelve samples grown for the fabrication of engineered interfaces FTJs. The heterostructures combine BTO thickness 2 nm and 3 nm, LSMO5 (LCMO5) thickness 1 nm and 2 nm, and STO and LAO substrates. Black diagonal line indicate heterostructures which suffered problems during the lithographic process and thus which are not available for measurements.

fabricated at LNESS using optical lithography, as described in subsection 3.2.2. A schematic diagram of the FTJ device geometry is shown in Figure 5.2.8.

The electrical measurements of the junctions were performed, as in the case of pure FE junction (section 5.1), in two-probe geometry (for details see section 3.5). Positive bias corresponds to current flow from the top to the bottom electrode. The ferroelectric polarization of the BTO barrier layer was switched by manually applying poling voltages V_{write} about 0.5 s long with a Keithley 2611. All resistances reported here are resistance values (R= V/I) at V = 100 mV extracted from I-V curves (from -0.2 V to 0.2 V, step 0.002 V) recorded with the same Keithley 2611 after the poling voltage pulse V_{write} was removed. In the following we report only on the preliminary results obtained at room temperature on the available Pt/LSMO5/BTO/LSMO junctions.

I-V curves of Pt/LSMO5/BTO/LSMO//STO junctions were collected upon polarizing BTO barrier layer with positive or negative V_{write} pulses, corresponding to ferroelectric polarization of BTO pointing down (P_{dn}) or

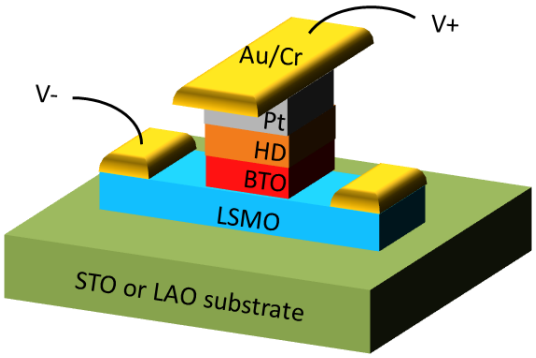

Figure 5.2.8: A schematic diagram of the FTJ device geometry integrating HD manganite layers.

up (P_{up}) respectively. Figure 5.2.9a shows I-V curves in P_{up} and P_{dn} states (violet and orange lines, respectively) of a representative FTJ with BTO ferroelectric barrier layer thickness 3 nm and LSMO5 thickness 1 nm, as shown in the inset. I-V characteristics are highly nonlinear, as expected for tunneling transport regime, and asymmetric in both P_{up} and P_{dn} states. Figure 5.2.9a also clearly shows that the resistance of these junctions depend on the direction of the polarization. I-V curves measured upon poling FE BTO barrier reveal a resistance difference between the positively (P_{dn}) or negatively (P_{up}) poled junctions more pronounced for positive bias, where tunneling is probing the unoccupied states of the HD manganite. The non-volatile resistance switching in these Pt/LSMO5/BTO/LSMO//STO FTJs is demonstrated by the clear hysteretic variation of the tunneling resistance obtained for all the junctions and shown in figure 5.2.9b for the same representative junction of panel a. Positive pulses set the device to the high-resistance (OFF) state by driving the polarization to point to the LSMO bottom electrode, whereas negative pulses switch the device to the low-resistance (ON) state by polarization reversal.

The same measurements were performed for Pt/LSMO5/BTO/LSMO FTJs grown on LAO substrates. Figure 5.2.10a shows I-V curves in P_{up} and P_{dn} states (violet and orange lines, respectively) of a representative FTJ with BTO ferroelectric barrier layer thickness 2 nm and LSMO5 thickness 2 nm, as shown in the inset. I-V characteristics are nonlinear, as expected

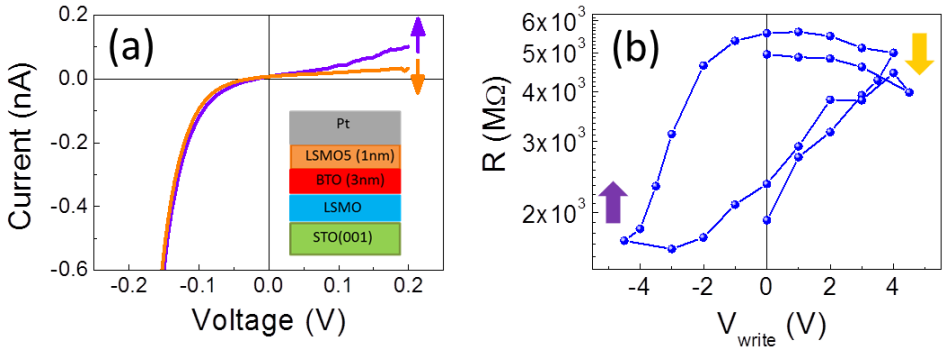

Figure 5.2.9: (a) ON and OFF room temperature I-V curves (violet and orange lines, respectively) of a Pt/LSMO5/BTO/LSMO FTJ (shown in the inset) grown on STO(001) substrate with BTO thickness 3 nm, LSMO5 thickness 1 nm and junction area A = 16 μm^2. (b) Resistance hysteresis loop measured using a pulse train for the same junction.

for tunneling transport regime, and symmetric in both P_{up} and P_{dn} states. Figure 5.2.10a also suggests that the resistance of these junctions depend on the direction of the FE polarization in the BTO. I-V curves measured upon poling FE BTO barrier reveal a resistance difference between the positively (P_{dn}) or negatively (P_{up}) poled junctions. The non-volatile resistance switching in these FTJs is demonstrated by the clear hysteretic variation of the tunneling resistance obtained for all the junctions and shown in figure 5.2.10b for the same representative junction of panel a. Positive pulses set the device to the high-resistance (OFF) state by driving the polarization to point to the LSMO bottom electrode, whereas negative pulses switch the device to the low-resistance (ON) state by polarization reversal.

Summarizing Pt/LSMO5/BTO/LSMO FTJs grown on LAO and STO show nonlinear I-V characteristics, as expected for tunneling transport regime, and clear hysteretic variation of the tunneling resistance, as expected for tunnel electroresistance effect. In particular, positive pulses set the device into the high-resistance (OFF) state by driving the polarization to point to the LSMO bottom electrode, whereas negative pulses switch the device into the low-resistance (ON) state by polarization reversal. Finally, note that FTJs on STO substrates show strongly asymmetric I-V curves, contrary to the case

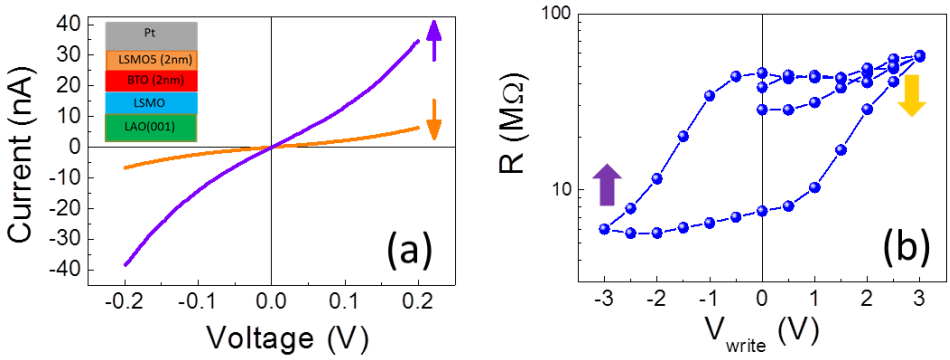

Figure 5.2.10: (a) ON and OFF room temperature I-V curves (violet and orange lines, respectively) of a Pt/LSMO5/BTO/LSMO FTJ (shown in the inset) grown on LAO(001) substrate with BTO thickness 2 nm, LSMO5 thickness 2 nm and junction area A = 8 μm^2. (b) Resistance hysteresis loop measured using a pulse train for the same junction.

of FTJs on LAO substrates.

To quantitatively compare the behavior of Pt/LSMO5/BTO/LSMO junctions grown on different (STO and LAO) substrates we use, as in section 5.1, the junction resistance per area product (R*A) and the tunnel electroresistance (TER) ratio, $TER = \frac{R_{OFF}-R_{ON}}{R_{ON}} * 100\%$, where R_{OFF} is the junction resistance in the high resistance state corresponding to BTO ferroelectric polarization pointing towards LSMO bottom electrode and R_{ON} is the junction resistance in the low resistance state corresponding to BTO ferroelectric polarization pointing towards Pt/LSMO5 top electrode. R*A and TER results are summarized in figure 5.2.11.

Figure 5.2.11a shows the average junction resistance per area product R*A (at 100 mV) corresponding to the OFF (P_{dn}) and ON (P_{up}) states (full and empty symbols, respectively) as a function of BTO barrier and HD thickness (sample 1: BTO 2 nm and LSMO5 2 nm, sample 2: BTO 3 nm and LSMO5 2 nm, sample 3: BTO 3 nm and LSMO5 1 nm, as indicated in the horizontal axis) for Pt/LSMO5/BTO/LSMO FTJs grown on STO (black squares) and LAO (red triangles) substrates. As a reference, we report in the same graph also the results obtained in section 5.1 for Pt/BTO/LSMO//STO (without LSMO5) junctions for the corresponding BTO thicknesses (2, 3 and

3 nm, respectively, green rhombus). Pt/LSMO5/BTO/LSMO FTJs grown on STO substrates (black squares) show higher R*A with respect to their analogous without LSMO5 layers (green rhombus). Moreover, we can observe an increase of R*A with higher LSMO5 thickness (compare sample 2 and sample 3, with constant BTO thickness but different half-doped thickness). These findings suggest that LSMO5 in Pt/LSMO5/BTO/LSMO//STO FTJs presents a strong insulating character. Pt/LSMO5/BTO/LSMO FTJs grown on LAO substrates (red triangles) instead show R*A values lower than the same FTJs grown on STO substrates (black squares) and comparable with the case of Pt/BTO/LSMO//STO junctions (green rhombus), thus indicating that resistance of LSMO5 in Pt/LSMO5/BTO/LSMO//LAO FTJs is definitely lower than that of BTO. However note that in the case of Pt/LSMO5/BTO/LSMO//LAO sample with 2 nm thick BTO barrier and 2 nm thick LSMO5 layer, R*A corresponding to the OFF (P_{dn}) state is well above the expected one for junctions without half-doped layer (green rhombus). This finding suggests that in this sample only for positive pulses (P_{dn} state) the additional resistance due to the LSMO5 film is comparable with that due to the BTO.

Figure 5.2.11b shows the TER ratios of all the measured junctions of the same samples considered in panel a. Data show that TER in Pt/LSMO5/BTO/LSMO FTJs grown on STO substrate (black squares) is lower than in corresponding pure FE Pt/BTO/LSMO//STO junctions (green rhombus). The same results is in general obtained for Pt/LSMO5/BTO/LSMO FTJs grown on LAO substrate (red triangles). However, for Pt/LSMO5/BTO/LSMO//LAO sample with 2 nm thick BTO and 2 nm thick LSMO5, measured TER ratios are well above the average one measured in Pt/BTO(2 nm)/LSMO//STO junctions (green rhombus). This is a promising result showing that the introduction of the HD manganite can be effective in increasing the TER, even though the fact that this is seen only for one substrate (LAO) and a proper combination of the HD and BTO thickness must be still clarified.

In conclusion, Pt/LSMO5/BTO/LSMO FTJs were fabricated on LAO and STO substrates. All junctions show at room temperature nonlinear I-V characteristics, as expected for tunneling transport regime, and clear

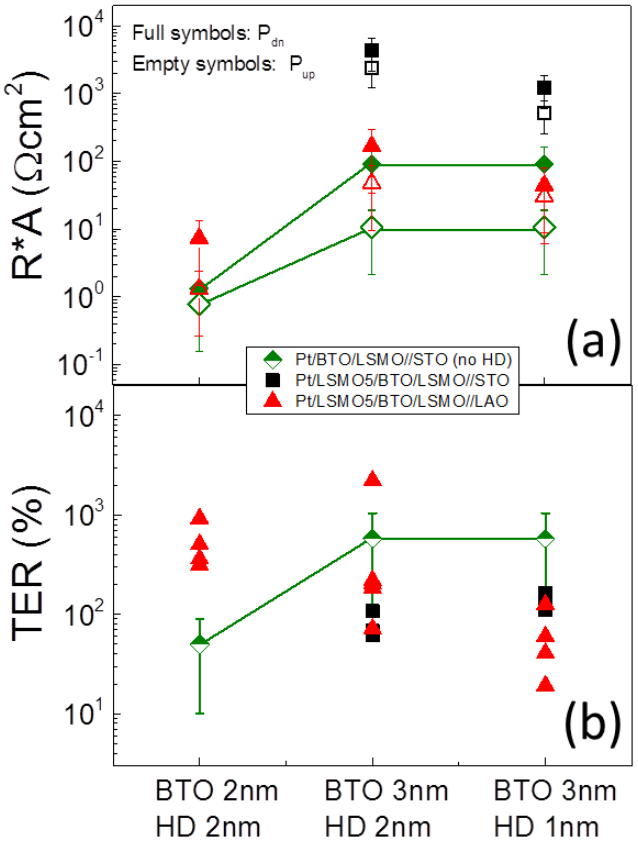

Figure 5.2.11: (a) Average junction resistance (at 100 mV) per area product R*A corresponding to the OFF (P_{dn}) and ON (P_{up}) states (full and empty symbols, respectively) as a function of BTO barrier and HD thickness (as indicated in the horizontal axis) for Pt/LSMO5/BTO/LSMO FTJs grown on STO (black squares) and LAO (red triangles) substrates. (b) TER of all the measured junctions of samples of panel (a). For comparison, green rhombus indicate the average results obtained for Pt/BTO/LSMO//STO (without LSMO5) junctions for the corresponding BTO thicknesses (2 and 3 nm).

hysteretic variation of the tunneling resistance, as expected for tunnel electroresistance effect. In particular, positive pulses set the device into the high-resistance (OFF) state by driving the polarization to point toward the LSMO bottom electrode, whereas negative pulses switch the device into the low-resistance (ON) state by polarization reversal. FTJs on STO substrates show strongly asymmetric I-V curves. A quantitative comparison between junctions grown on STO and LAO substrate suggests that at room temperature LSMO5 layers when integrated in Pt/LSMO5/BTO/LSMO//STO FTJs behave as strong insulators, while in the Pt/LSMO5/BTO/LSMO//LAO FTJs their contribution to the resistance is not comparable with that of the BTO, independently on FE polarization direction of BTO. Only in the case of sample Pt/LSMO5(2 nm)/BTO(2 nm)/LSMO//LAO the resistance of the LSMO5 layer seems to get comparable with the BTO one for BTO ferroelectric polarization pointing toward the LSMO bottom electrode (P_{dn}). Correspondingly, TER effect seems to be depressed by the presence of the LSMO5 layer in the FTJs, thus suggesting that in these samples at room temperature LSMO5 layers are not active: no electric field induced phase transition. Only in the particular case of Pt/LSMO5(2 nm)/BTO(2 nm)/LSMO//LAO sample, the TER ratio is well above the one measured in the corresponding pure FE Pt/BTO/LSMO//STO junctions (without LSMO5 layers), as would be expected in case of E-field induced metal-insulator transition of the HD manganite. This is a promising result showing that the introduction of the HD can be effective in increasing the TER, even though the fact that this is seen only for one substrate (LAO) and a proper combination of the HD and BTO thickness must be still clarified.

These preliminary results underline the complexity and potential of Pt/HD/BTO/LSMO FTJs. Further measurements and low temperature characterization are needed to fully understand the possible role of HD manganite in tunneling process.

Part IV

Conclusions

Chapter 6

Summary

The present thesis was devoted to the investigation of memory/logic devices based on tunnel junctions which are characterized by (at least) two well defined remanent resistance states that can be controlled by an external E-field. As it has been mentioned in the introduction, two different strategies have been used:

A) *E-field control of the remanent resistance states of a magnetic tunnel junction (MTJ) by using magnetoelectric coupling (MEC) effects at multiferroic (FE & FM) interfaces.*

B) *E-field control of the remanent resistance states of a tunnel junction with FE barrier (FTJ) displaying TER effect.*

In the following are presented the main results and future prospects for each strategy.

6.1 Magneto-electric coupling at Fe/BTO interface for the E-field control of MTJs

The first part of the present thesis was devoted to the study of the physics of magnetoelectric coupling (MEC) at the $Fe/BaTiO_3$ (BTO) fully epitaxial multiferroic interface. This knowledge is of fundamental scientific interest

and should be valuable in view of the engineering of multiferroic heterostructures for application in electrically controlled spintronic devices.

Fully epitaxial Fe/BTO bilayers have been grown on $La_{0.67}Sr_{0.33}MnO_3$ // $SrTiO_3$(001) (LSMO//STO) or $Nb : SrTiO_3$(001) (Nb:STO, which stands for conductive 1.0% wt. Nb doped STO single-crystal substrates) in a multichamber system equipped with both pulsed laser deposition and molecular beam epitaxy.

Ferroelectric and structural characterization of BTO films grown with the optimized recipe reveal their good ferroelectric properties and high quality of their interfaces, which is a fundamental starting point for the growth and the study of epitaxial Fe/BTO interfaces.

Structural and chemical characterization of Fe films indicate that Fe grows epitaxially on BTO with a well defined cubic structure presenting a 45° rotation with respect to the BTO lattice. However, ultrathin Fe films (thickness $\leq$ 1 nm) grow on BTO in a three dimensional mode while 2D growth can be achieved only in optimized conditions. This is consistent with the characteristic tendency of metals to form nanoislands at the early stage of growth onto oxides. The Fe/BTO interface is sharp and Fe oxidation is limited to the first atomic layer (FeOx) in chemical contact with the BTO. Characterization as a function of the growth conditions clearly point out the high robustness and chemical stability of the Fe/BTO interface. This knowledge is of fundamental importance in view of the studying of magnetoelectric coupling mechanisms taking place at this same interface.

Magnetic and magnetoelectric characterization of the fully epitaxial Fe/BTO system performed by Magneto-Optical Kerr Effect (MOKE) experiments under electric-bias conditions show that: i) Fe films (few nm thick) display the expected fourfold anisotropy, with easy axes rotated by 45° with respect to the BTO[100] direction, according to the previously established epitaxial relationship; ii) no appreciable changes of Fe thin films magnetic anisotropy and coercivity are observed upon reversal of the BTO polarization. This finding indicates that strain-mediated MEC is suppressed in fully epitaxial Fe/BTO systems, likely due to clamping of BTO to the substrate.

Magnetoresistance measurements under electric-bias conditions on mag-

netic tunnel junctions (MTJs) Fe/MgO/Fe fabricated on BTO films show no sizable variations of the magnetic coercive fields or of the tunnel magnetoresistance (TMR) upon reversal of the polarization of the BTO layer in contact with the Fe bottom electrode of the MTJ. These findings confirm the absence of sizable strain-mediated effect and demonstrate the strong localization at the Fe/BTO interface of predicted pure-electronic MEC mechanisms. In this contest, the feasibility of the E-MTJ approach is discussed.

Pure-electronic MEC at fully epitaxial Fe/BTO interface is demonstrated by using ultrathin Fe films in combination with X-ray magnetic circular dichroism and first principles calculations. We find evidence for an undisclosed physical mechanism for interfacial MEC in the fully epitaxial Fe/BTO system: the magnetization of the interfacial ultrathin oxidized iron layer (FeOx) can be electrically and reversibly switched on-off at room-temperature by reversing the BTO polarization. The suppression / recovery of interfacial ferromagnetism results from the asymmetric effect that ionic displacements in BTO produces on the exchange coupling constants in the adjacent FeOx layer. These results shed light on the physics of MEC at fully epitaxial Fe/BTO interface and confirm the great potential of the peculiar mechanism for MEC here disclosed to achieve a reversible, fully electrical writing of the magnetic information in spintronic devices, such as MTJs, where the surface magnetization plays a major role. However we envisage that the device geometry must be compatible with the strong interfacial localization of these effects, as in the case of multiferroic tunnel junctions (MFTJs), where the multiferroic interface is directly involved in the tunneling.

6.2 FTJs displaying TER effect

The second part of the present thesis was devoted to the fabrication and characterization of ferroelectric tunnel junctions (FTJs) whose remanent resistance states can be controlled by an electric field by exploiting the tunnel electroresistance (TER) effect.

Micron-sized FTJs have been fabricated on Pt(22 nm)/BTO(2-4 nm)/LSMO(30 nm) heterostructures grown at ICMAB on (001) - oriented STO single crys-

tal substrates by pulsed laser deposition and ex-situ sputtering techniques. Electrical characterization of the junctions indicate that, despite these are large area devices, transport at room temperature is dominated by tunneling. Moreover, FTJ devices display two remanent resistance states that can be controlled electrically switching the ferroelectric polarization direction in the BTO barrier. TER ratio increases exponentially with BTO barrier thickness, suggesting that the mechanisms governing the TER in these micron-sized junctions are the same reported previously for non-lithographed samples measured using SPM techniques with the conductive tip used as a top electrode in contact with the surface of the ferroelectric layer. Finally we underline that TER ratios achieved in our junctions (up to 10^4%) represent up to now record values for room temperature TER in micron-sized FTJs without engineered interfaces.

Aiming to develop barriers of adjustable width and thus enhance the TER ratio, materials displaying E-field induced metal-insulator transition (half-doped manganites $La_{0.5}A_{0.5}MnO_3$, A = Ca/Sr) have been developed and integrated in epitaxial FE/half-doped manganite heterostructures.

We have thus firstly explored the strain role on half-doped (HD) manganites magnetic and transport properties. Thin films of $La_{0.5}Sr_{0.5}MnO_3$ (LSMO5) and $La_{0.5}Ca_{0.5}MnO_3$ (LCMO5), 20 nm thick, have been epitaxially grown by pulsed laser deposition at ICMAB on a variety of substrates. It is found that epitaxial strain imposed by the substrates promotes pseudo-tetragonal cells with c/a ratio that can be largely tuned. The ground state of bulk LSMO5 is recovered in thin films grown on well matched substrates, and the corresponding thin films are ferromagnetic and metallic. In contrast, compressive biaxial strain leads to the emergence of an antiferromagnetic insulating state and tensile strain leads to an uncommon antiferromagnetic and metallic (in-plane) phase. The reduced metallicity of LSMO5 under strong tensile strain is attributed to the combined effect of conduction band narrowing and the ubiquitous presence of extended planar defects in the film. In the narrower bandwidth LCMO5 oxide, the epitaxial strain imposed by the substrates drives in all cases the films into an antiferromagnetic and insulating state, with minor effects on conductivity or magnetization. It thus

follows that strain has remarkably different effects on LSMO5 and LCMO5 that mainly arise from the difference in the electronic bandwidth and the corresponding ground state. These findings suggest that HD manganites, if integrated on piezoelectric stressors or tunnel junctions in conjunction with ferroelectric layers, will respond differently depending of their bandwidth. For instance, we envisage any field effects should dominate in LCMO5 based barriers whereas piezo-induced strain may have a more prominent role on LSMO5.

Finally Pt(22 nm)/LSMO5(1-2 nm)/BTO(2-3 nm)/LSMO(30 nm) and Pt(22 nm)/LCMO5(1-2 nm)/BTO(2-3 nm)/LSMO(30 nm) tunnel heterostructures have been grown on STO(001) and $LaAlO_3$(001) (LAO) substrates and processed into devices for TER measurements. Preliminary experiments performed at room temperature show an increase of the TER, with respect to the corresponding case without the HD manganite, only in case of a barrier made of 2 nm of BTO and 2 nm of LSMO5.

This is a promising result for future developments, even though the understanding of the fine details of the phenomena involved in this kind of engineered TER junctions asks for further investigation. Noteworthy, the possibility of studying these effects in micron sized fabricated tunnel junctions, offers the opportunity of performing experiments onto statistically meaningful set of devices. This is crucial in order to put the research on this field on a more solid basis, and advance towards the exploitation of these concepts.

Bibliography

[1] J. Frenkel, "On the electrical resistance of contacts between solid conductors," *Physical Review*, vol. 36, pp. 1604–1618, 1930. [Online]. Available: http://prola.aps.org/abstract/PR/v36/i11/p1604_1

[2] M. Bibes, J. E. Villegas, and A. Barthélémy, "Ultrathin oxide films and interfaces for electronics and spintronics," *Advances in Physics*, vol. 60, no. 1, pp. 5–84, Feb. 2011. [Online]. Available: http://www.tandfonline.com/doi/abs/10.1080/00018732.2010.534865

[3] M. Julliere, "Tunneling between ferromagnetic films," *Physics Letters A*, vol. 54, no. 3, pp. 225–226, Sep. 1975. [Online]. Available: http://linkinghub.elsevier.com/retrieve/pii/0375960175901747

[4] P. Tedrow and R. Meservey, "Spin-Dependent Tunneling into Ferromagnetic Nickel," *Physical Review Letters*, vol. 26, pp. 192–195, 1971.

[5] E. Y. Tsymbal, O. N. Mryasov, and P. R. LeClair, "Spin-dependent tunnelling in magnetic tunnel junctions," *Journal of Physics: Condensed Matter*, vol. 15, no. 4, pp. R109–R142, Feb. 2003. [Online]. Available: http://stacks.iop.org/0953-8984/15/i=4/a=201?key=crossref.ddb2aa5408ae58ff8bdc0d3ceca723b1

[6] J. S. Moodera, L. R. Kinder, T. M. Wong, and R. Meservey, "Large Magnetoresistance at Room Temperature in Ferromagnetic Thin Film Tunnel Junctions," *Physical Review Letters*, vol. 74, no. 16, pp. 3273–3276, Apr. 1995. [Online].

Available: http://prl.aps.org/abstract/PRL/v74/i16/p3273_1http://link.aps.org/doi/10.1103/PhysRevLett.74.3273

[7] S. Ikeda, J. Hayakawa, Y. Ashizawa, Y. M. Lee, K. Miura, H. Hasegawa, M. Tsunoda, F. Matsukura, and H. Ohno, "Tunnel magnetoresistance of 604% at 300 K by suppression of Ta diffusion in CoFeB/MgO/CoFeB pseudo-spin-valves annealed at high temperature," *Applied Physics Letters*, vol. 93, no. 8, p. 082508, 2008. [Online]. Available: http://link.aip.org/link/APPLAB/v93/i8/p082508/s1&Agg=doi

[8] E. Tsymbal, a. Gruverman, V. Garcia, M. Bibes, and a. Barthélémy, "Ferroelectric and multiferroic tunnel junctions," *MRS Bulletin*, vol. 37, no. 02, pp. 138–143, Feb. 2012. [Online]. Available: http://www.journals.cambridge.org/abstract_S0883769411003587

[9] J. P. Velev, S. S. Jaswal, and E. Y. Tsymbal, "Multi-ferroic and magnetoelectric materials and interfaces." *Philosophical transactions. Series A, Mathematical, physical, and engineering sciences*, vol. 369, no. 1948, pp. 3069–97, Aug. 2011. [Online]. Available: http://rsta.royalsocietypublishing.org/content/369/1948/3069.abstracthttp://www.ncbi.nlm.nih.gov/pubmed/21727115

[10] N. a. Pertsev and H. Kohlstedt, "Magnetic tunnel junction on a ferroelectric substrate," *Applied Physics Letters*, vol. 95, no. 16, p. 163503, 2009. [Online]. Available: http://link.aip.org/link/APPLAB/v95/i16/p163503/s1&Agg=doi

[11] E. Y. Tsymbal and H. Kohlstedt, "Applied physics. Tunneling across a ferroelectric." *Science (New York, N.Y.)*, vol. 313, no. 5784, pp. 181–3, Jul. 2006. [Online]. Available: http://www.ncbi.nlm.nih.gov/pubmed/16840688

[12] E. Y. Tsymbal and A. Gruverman, "Ferroelectric tunnel junctions: Beyond the barrier." *Nature materials*, vol. 12, no. 7, pp. 602–4, Jul. 2013. [Online]. Available: http://books.google.com/books?hl=en&lr=&id=dZk46iaENlAC&oi=fnd&pg=PT4&dq=Beyond+the+barrier&ots=

EjKCGNHKid&sig=odDRfySsX8gq4dr8XszlxYWQfrAhttp://books.google.com/books?hl=en&lr=&id=dZk46iaENlAC&oi=fnd&pg=PT4&dq=Beyond+the+barrier&ots=EjKCGNHKk9&sig=zsa7qciwINj830Y8Z5p6DHCAZ1Ahttp://www.ncbi.nlm.nih.gov/pubmed/23685862

[13] A. M. Ionescu, "Nanoelectronics: Ferroelectric devices show potential." *Nature nanotechnology*, vol. 7, no. 2, pp. 83–5, Feb. 2012. [Online]. Available: http://www.ncbi.nlm.nih.gov/pubmed/22306895

[14] M. Bibes, "Nanoferronics is a winning combination." *Nature materials*, vol. 11, no. 5, pp. 354–7, May 2012. [Online]. Available: http://www.ncbi.nlm.nih.gov/pubmed/22522625

[15] C. a. F. Vaz, J. Hoffman, C. H. Ahn, and R. Ramesh, "Magnetoelectric coupling effects in multiferroic complex oxide composite structures." *Advanced materials (Deerfield Beach, Fla.)*, vol. 22, no. 26-27, pp. 2900–18, Jul. 2010. [Online]. Available: http://www.ncbi.nlm.nih.gov/pubmed/20414887

[16] H. Schmid, "Multi-ferroic magnetoelectrics," *Ferroelectrics*, vol. 162, pp. 317–338, 1994.

[17] T. Lottermoser, T. Lonkai, U. Amann, D. Hohlwein, J. Ihringer, and M. Fiebig, "Magnetic phase control by an electric field," *nature*, vol. 430, pp. 541–544, 2004.

[18] T. Kimura, T. Goto, H. Shintani, K. Ishizaka, T. Arima, and Y. Tokura, "Magnetic control of ferroelectric polarization." *Nature*, vol. 426, pp. 55–58, 2003.

[19] J. Slonczewski, "Current-driven excitation of magnetic multilayers," *Journal of Magnetism and Magnetic Materials*, vol. 159, no. 1-2, pp. L1–L7, Jun. 1996. [Online]. Available: http://linkinghub.elsevier.com/retrieve/pii/0304885396000625

[20] W.-G. Wang, M. Li, S. Hageman, and C. L. Chien, "Electric-field-assisted switching in magnetic tunnel junctions." *Nature materials*, vol. 11, no. 1, pp. 64–8, Jan. 2012. [Online]. Available: http://www.ncbi.nlm.nih.gov/pubmed/22081084

[21] Y. Shiota, T. Nozaki, F. Bonell, S. Murakami, T. Shinjo, and Y. Suzuki, "Induction of coherent magnetization switching in a few atomic layers of FeCo using voltage pulses." *Nature materials*, vol. 11, no. 1, pp. 39–43, Jan. 2012. [Online]. Available: http://www.ncbi.nlm.nih.gov/pubmed/22081081

[22] N. A. Spaldin and M. Fiebig, "Materials science. The renaissance of magnetoelectric multiferroics." *Science (New York, N.Y.)*, vol. 309, no. 5733, pp. 391–2, Jul. 2005. [Online]. Available: http://www.sciencemag.org/content/309/5733/391.shorthttp://www.ncbi.nlm.nih.gov/pubmed/16020720

[23] G. A. Smolenskii and I. E. Chupis, "Ferroelectromagnets," *Soviet Physics Uspekhi*, vol. 25, pp. 475–493, 1982. [Online]. Available: http://iopscience.iop.org/0038-5670/25/7/R02

[24] N. a. Hill, "Why Are There so Few Magnetic Ferroelectrics?" *The Journal of Physical Chemistry B*, vol. 104, no. 29, pp. 6694–6709, Jul. 2000. [Online]. Available: http://pubs.acs.org/doi/abs/10.1021/jp000114x

[25] M. Fiebig, "Revival of the magnetoelectric effect," *Journal of Physics Dapplied Physics*, vol. 38, no. 8, pp. R123–R152, Apr. 2005. [Online]. Available: http://apps.webofknowledge.com/full_record.do?page=1&qid=15&log_event=no&viewType=fullRecord&SID=3EC@C12mK418aC8gLKo&product=UA&doc=1&search_mode=GeneralSearch

[26] C.-G. Duan, S. Jaswal, and E. Tsymbal, "Predicted Magnetoelectric Effect in Fe/BaTiO3 Multilayers: Ferroelectric Control of Magnetism,"

Physical Review Letters, vol. 97, no. 4, p. 047201, Jul. 2006. [Online]. Available: http://link.aps.org/doi/10.1103/PhysRevLett.97.047201

[27] C.-G. Duan, J. Velev, R. Sabirianov, Z. Zhu, J. Chu, S. Jaswal, and E. Tsymbal, "Surface Magnetoelectric Effect in Ferromagnetic Metal Films," *Physical Review Letters*, vol. 101, no. 13, p. 137201, Sep. 2008. [Online]. Available: http://link.aps.org/doi/10.1103/PhysRevLett.101.137201

[28] M. Fechner, I. Maznichenko, S. Ostanin, a. Ernst, J. Henk, P. Bruno, and I. Mertig, "Magnetic phase transition in two-phase multiferroics predicted from first principles," *Physical Review B*, vol. 78, no. 21, p. 212406, Dec. 2008. [Online]. Available: http://link.aps.org/doi/10.1103/PhysRevB.78.212406

[29] S. Valencia, A. Crassous, L. Bocher, V. Garcia, X. Moya, R. O. Cherifi, C. Deranlot, K. Bouzehouane, S. Fusil, A. Zobelli, A. Gloter, N. D. Mathur, A. Gaupp, R. Abrudan, F. Radu, A. Barthélémy, and M. Bibes, "Interface-induced room-temperature multiferroicity in BaTiO_3." *Nature materials*, vol. 10, no. 10, pp. 753–8, Oct. 2011. [Online]. Available: http://www.ncbi.nlm.nih.gov/pubmed/21857674

[30] C.-G. Duan, J. P. Velev, R. F. Sabirianov, W. N. Mei, S. S. Jaswal, and E. Y. Tsymbal, "Tailoring magnetic anisotropy at the ferromagnetic/ferroelectric interface," *Applied Physics Letters*, vol. 92, no. 12, p. 122905, 2008. [Online]. Available: http://link.aip.org/link/APPLAB/v92/i12/p122905/s1&Agg=doi

[31] S. Zhang, "Spin-dependent surface screening in ferromagnets and magnetic tunnel junctions," *Physical review letters*, vol. 83, no. 3, pp. 640–643, 1999. [Online]. Available: http://prl.aps.org/abstract/PRL/v83/i3/p640_1

[32] T. Cai, S. Ju, J. Lee, N. Sai, A. Demkov, Q. Niu, Z. Li, J. Shi, and E. Wang, "Magnetoelectric coupling and electric control of magnetization in ferromagnet/ferroelectric/normal-metal

superlattices," *Physical Review B*, vol. 80, no. 14, p. 140415, Oct. 2009. [Online]. Available: http://link.aps.org/doi/10.1103/PhysRevB.80.140415

[33] S. Brivio, D. Petti, R. Bertacco, and J. C. Cezar, "Electric field control of magnetic anisotropies and magnetic coercivity in Fe/BaTiO3(001) heterostructures," *Applied Physics Letters*, vol. 98, no. 9, p. 092505, 2011. [Online]. Available: http://link.aip.org/link/APPLAB/v98/i9/p092505/s1&Agg=doi

[34] S. Sahoo, S. Polisetty, C.-G. Duan, S. Jaswal, E. Tsymbal, and C. Binek, "Ferroelectric control of magnetism in BaTiO3/Fe heterostructures via interface strain coupling," *Physical Review B*, vol. 76, no. 9, p. 092108, Sep. 2007. [Online]. Available: http://link.aps.org/doi/10.1103/PhysRevB.76.092108

[35] V. Garcia, M. Bibes, L. Bocher, S. Valencia, F. Kronast, a. Crassous, X. Moya, S. Enouz-Vedrenne, a. Gloter, D. Imhoff, C. Deranlot, N. D. Mathur, S. Fusil, K. Bouzehouane, and a. Barthélémy, "Ferroelectric control of spin polarization." *Science (New York, N.Y.)*, vol. 327, no. 5969, pp. 1106–10, Feb. 2010. [Online]. Available: http://www.ncbi.nlm.nih.gov/pubmed/20075211

[36] H. Zheng, J. Wang, S. E. Lofland, Z. Ma, L. Mohaddes-Ardabili, T. Zhao, L. Salamanca-Riba, S. R. Shinde, S. B. Ogale, F. Bai, D. Viehland, Y. Jia, D. G. Schlom, M. Wuttig, A. Roytburd, and R. Ramesh, "Multiferroic BaTiO3-CoFe2O4 Nanostructures." *Science (New York, N.Y.)*, vol. 303, no. 5658, pp. 661–3, Jan. 2004. [Online]. Available: http://www.ncbi.nlm.nih.gov/pubmed/14752158

[37] D. G. Schlom, L.-Q. Chen, C.-B. Eom, K. M. Rabe, S. K. Streiffer, and J.-M. Triscone, "Strain Tuning of Ferroelectric Thin Films *," *Annual Review of Materials Research*, vol. 37, no. 1, pp. 589–626, Aug. 2007. [Online]. Available: http://www.annualreviews.org/doi/abs/10.1146/annurev.matsci.37.061206.113016

[38] L. Esaki, R. B. Laibowitz, and P. J. Stiles, "Polar switch," *IBM Tech. Discl. Bull*, vol. 13, p. 2161, 1971.

[39] D. D. Fong, G. B. Stephenson, S. K. Streiffer, J. a. Eastman, O. Auciello, P. H. Fuoss, and C. Thompson, "Ferroelectricity in ultrathin perovskite films." *Science (New York, N.Y.)*, vol. 304, no. 5677, pp. 1650–3, Jun. 2004. [Online]. Available: http://www.ncbi.nlm.nih.gov/pubmed/15192223

[40] C. Lichtensteiger, J.-M. Triscone, J. Junquera, and P. Ghosez, "Ferroelectricity and Tetragonality in Ultrathin PbTiO3 Films," *Physical Review Letters*, vol. 94, no. 4, p. 047603, Feb. 2005. [Online]. Available: http://link.aps.org/doi/10.1103/PhysRevLett.94.047603

[41] D. a. Tenne, a. Bruchhausen, N. D. Lanzillotti-Kimura, a. Fainstein, R. S. Katiyar, a. Cantarero, a. Soukiassian, V. Vaithyanathan, J. H. Haeni, W. Tian, D. G. Schlom, K. J. Choi, D. M. Kim, C. B. Eom, H. P. Sun, X. Q. Pan, Y. L. Li, L. Q. Chen, Q. X. Jia, S. M. Nakhmanson, K. M. Rabe, and X. X. Xi, "Probing nanoscale ferroelectricity by ultraviolet Raman spectroscopy." *Science (New York, N.Y.)*, vol. 313, no. 5793, pp. 1614–6, Sep. 2006. [Online]. Available: http://www.ncbi.nlm.nih.gov/pubmed/16973874

[42] T. M. Shaw, S. Trolier-McKinstry, and P. C. McIntyre, "THE PROPERTIES OF FERROELECTRIC FILMS AT SMALL DIMENSIONS," *Annual Review of Materials Science*, vol. 30, no. 1, pp. 263–298, Aug. 2000. [Online]. Available: http://dx.doi.org/10.1146/annurev.matsci.30.1.263

[43] M. Zhuravlev, R. Sabirianov, S. Jaswal, and E. Tsymbal, "Giant Electroresistance in Ferroelectric Tunnel Junctions," *Physical Review Letters*, vol. 94, no. 24, p. 246802, Jun. 2005. [Online]. Available: http://link.aps.org/doi/10.1103/PhysRevLett.94.246802

[44] H. Kohlstedt, N. Pertsev, J. Rodríguez Contreras, and R. Waser, "Theoretical current-voltage characteristics of ferroelectric tunnel

junctions," *Physical Review B*, vol. 72, no. 12, p. 125341, Sep. 2005. [Online]. Available: http://link.aps.org/doi/10.1103/PhysRevB.72.125341

[45] J. Velev, C.-G. Duan, K. Belashchenko, S. Jaswal, and E. Tsymbal, "Effect of Ferroelectricity on Electron Transport in Pt/BaTiO3/Pt Tunnel Junctions," *Physical Review Letters*, vol. 98, no. 13, p. 137201, Mar. 2007. [Online]. Available: http://link.aps.org/doi/10.1103/PhysRevLett.98.137201

[46] J. Burton and E. Tsymbal, "Prediction of electrically induced magnetic reconstruction at the manganite/ferroelectric interface," *Physical Review B*, vol. 80, no. 17, p. 174406, Nov. 2009. [Online]. Available: http://link.aps.org/doi/10.1103/PhysRevB.80.174406

[47] J. D. Burton and E. Y. Tsymbal, "Giant Tunneling Electroresistance Effect Driven by an Electrically Controlled Spin Valve at a Complex Oxide Interface," *Physical Review Letters*, vol. 106, no. 15, p. 157203, Apr. 2011. [Online]. Available: http://link.aps.org/doi/10.1103/PhysRevLett.106.157203

[48] R. Waser and M. Aono, "Nanoionics-based resistive switching memories." *Nature materials*, vol. 6, no. 11, pp. 833–40, Nov. 2007. [Online]. Available: http://www.ncbi.nlm.nih.gov/pubmed/17972938

[49] A. Gruverman, O. Auciello, and H. Tokumoto, "IMAGING AND CONTROL OF DOMAIN STRUCTURES IN FERROELECTRIC THIN FILMS VIA SCANNING FORCE MICROSCOPY," *Annual Review of Materials Science*, vol. 28, no. 1, pp. 101–123, Aug. 1998. [Online]. Available: http://dx.doi.org/10.1146/annurev.matsci.28.1.101http://www.annualreviews.org/doi/abs/10.1146/annurev.matsci.28.1.101

[50] V. Garcia, S. Fusil, K. Bouzehouane, S. Enouz-Vedrenne, N. D. Mathur, a. Barthélémy, and M. Bibes, "Giant tunnel electroresistance for non-destructive readout of ferroelectric states." *Nature*, vol.

460, no. 7251, pp. 81–4, Jul. 2009. [Online]. Available: http://www.ncbi.nlm.nih.gov/pubmed/19483675

[51] P. Maksymovych, S. Jesse, P. Yu, R. Ramesh, A. P. Baddorf, and S. V. Kalinin, "Polarization control of electron tunneling into ferroelectric surfaces." *Science (New York, N.Y.)*, vol. 324, no. 5933, pp. 1421–5, Jun. 2009. [Online]. Available: http://www.ncbi.nlm.nih.gov/pubmed/19520954

[52] a. Gruverman, D. Wu, H. Lu, Y. Wang, H. W. Jang, C. M. Folkman, M. Y. Zhuravlev, D. Felker, M. Rzchowski, C.-B. Eom, and E. Y. Tsymbal, "Tunneling electroresistance effect in ferroelectric tunnel junctions at the nanoscale." *Nano letters*, vol. 9, no. 10, pp. 3539–43, Oct. 2009. [Online]. Available: http://www.ncbi.nlm.nih.gov/pubmed/19697939

[53] A. Crassous, V. Garcia, K. Bouzehouane, S. Fusil, a. H. G. Vlooswijk, G. Rispens, B. Noheda, M. Bibes, and A. Barthélémy, "Giant tunnel electroresistance with PbTiO[sub 3] ferroelectric tunnel barriers," *Applied Physics Letters*, vol. 96, no. 4, p. 042901, 2010. [Online]. Available: http://link.aip.org/link/APPLAB/v96/i4/p042901/s1&Agg=doi

[54] D. Pantel, S. Goetze, D. Hesse, and M. Alexe, "Room-Temperature Ferroelectric Resistive Switching in Ultrathin Pb(Zr 0.2 Ti 0.8)O 3 Films," *ACS Nano*, vol. 5, no. 7, pp. 6032–6038, Jul. 2011. [Online]. Available: http://link.aip.org/link/APPLAB/v100/i23/p232902/s1&Agg=doihttp://pubs.acs.org/doi/abs/10.1021/nn2018528

[55] D. Pantel, H. Lu, S. Goetze, P. Werner, D. Jik Kim, A. Gruverman, D. Hesse, and M. Alexe, "Tunnel electroresistance in junctions with ultrathin ferroelectric Pb(Zr0.2Ti0.8)O3 barriers," *Applied Physics Letters*, vol. 100, no. 23, p. 232902, 2012. [Online]. Available: http://link.aip.org/link/APPLAB/v100/i23/p232902/s1&Agg=doi

[56] A. Chanthbouala, A. Crassous, V. Garcia, K. Bouzehouane, S. Fusil, X. Moya, J. Allibe, B. Dlubak, J. Grollier, S. Xavier, C. Deranlot, A. Moshar, R. Proksch, N. D. Mathur, M. Bibes, and A. Barthélémy, "Solid-state memories based on ferroelectric tunnel junctions," *Nature nanotechnology*, vol. 7, no. 2, pp. 101–4, Feb. 2012. [Online]. Available: http://www.ncbi.nlm.nih.gov/pubmed/22138863

[57] H. Yamada, V. Garcia, S. Fusil, and S. Boyn, "Giant Electroresistance of Super-Tetragonal BiFeO3 Based Ferroelectric Tunnel Junctions," *ACS ...*, vol. 7, no. 6, pp. 5385–5390, 2013. [Online]. Available: http://pubs.acs.org/doi/abs/10.1021/nn401378t

[58] A. Chanthbouala, V. Garcia, R. O. Cherifi, K. Bouzehouane, S. Fusil, X. Moya, S. Xavier, H. Yamada, C. Deranlot, N. D. Mathur, M. Bibes, A. Barthélémy, and J. Grollier, "A ferroelectric memristor," *Nature materials*, vol. 11, no. 10, pp. 860–4, Oct. 2012. [Online]. Available: http://www.ncbi.nlm.nih.gov/pubmed/22983431

[59] D. Pantel, S. Goetze, D. Hesse, and M. Alexe, "Reversible electrical switching of spin polarization in multiferroic tunnel junctions." *Nature materials*, vol. 11, no. 4, pp. 289–93, Apr. 2012. [Online]. Available: http://dx.doi.org/10.1038/nmat3254http://www.ncbi.nlm.nih.gov/pubmed/22367005

[60] Z. Wen, L. You, J. Wang, A. Li, and D. Wu, "Temperature-dependent tunneling electroresistance in Pt/BaTiO3/SrRuO3 ferroelectric tunnel junctions," *Applied Physics Letters*, vol. 103, no. 13, p. 132913, 2013. [Online]. Available: http://link.aip.org/link/APPLAB/v103/i13/p132913/s1&Agg=doi

[61] Z. Wen, C. Li, D. Wu, A. Li, and N. Ming, "Ferroelectric-field-effect-enhanced electroresistance in metal/ferroelectric/semiconductor tunnel junctions." *Nature materials*, vol. 12, no. 7, pp. 617–21, Jul. 2013. [Online]. Available: http://www.ncbi.nlm.nih.gov/pubmed/23685861

[62] Y. W. Yin, J. D. Burton, Y.-M. Kim, a. Y. Borisevich, S. J. Pennycook, S. M. Yang, T. W. Noh, a. Gruverman, X. G. Li, E. Y. Tsymbal, and Q. Li, "Enhanced tunnelling electroresistance effect due to a ferroelectrically induced phase transition at a magnetic complex oxide interface." *Nature materials*, vol. 12, no. 5, pp. 397–402, May 2013. [Online]. Available: http://www.ncbi.nlm.nih.gov/pubmed/23416728

[63] D. J. Kim, H. Lu, S. Ryu, C.-W. Bark, C.-B. Eom, E. Y. Tsymbal, and a. Gruverman, "Ferroelectric tunnel memristor." *Nano letters*, vol. 12, no. 11, pp. 5697–702, Nov. 2012. [Online]. Available: http://www.ncbi.nlm.nih.gov/pubmed/23039785

[64] Y. W. Yin, M. Raju, W. J. Hu, X. J. Weng, X. G. Li, and Q. Li, "Coexistence of tunneling magnetoresistance and electroresistance at room temperature in La0.7Sr0.3MnO3/(Ba, Sr)TiO3/La0.7Sr0.3MnO3 multiferroic tunnel junctions," *Journal of Applied Physics*, vol. 109, no. 7, p. 07D915, 2011. [Online]. Available: http://link.aip.org/link/JAPIAU/v109/i7/p07D915/s1&Agg=doi

[65] D. Pantel, S. Goetze, D. Hesse, and M. Alexe, "Reversible electrical switching of spin polarization in multiferroic tunnel junctions." *Nature materials*, vol. 11, no. 4, pp. 289–93, Apr. 2012. [Online]. Available: http://www.ncbi.nlm.nih.gov/pubmed/22367005

[66] R. Bertacco, M. Cantoni, M. Riva, a. Tagliaferri, and F. Ciccacci, "Epitaxial growth and characterization of layered magnetic nanostructures," *Applied Surface Science*, vol. 252, no. 5, pp. 1754–1764, Dec. 2005. [Online]. Available: http://linkinghub.elsevier.com/retrieve/pii/S0169433205005787

[67] O. Svelto and D. C. Hanna, *Principles of Lasers*. Springer, 1998. [Online]. Available: http://books.google.it/books?id=F_-o6dVlRtUC

[68] M. P. Seah and W. A. Dench, "Quantitative Electron Spectroscopy of Surfaces : A Standard Data Base for Electron Inelastic Mean Free Paths in Solids," *Surface and Interface Analysis*, vol. 1, pp. 2–11, 1979.

[69] I. Fina, "Ferroelectricity and magnetoelectric coupling in magnetic ferroelectrics and artificial multiferroic heterostructures," Ph.D. dissertation, Institut de Ciència de Materials de Barcelona, 2012. [Online]. Available: http://www.tesisenred.net/handle/10803/81981

[70] M. state university, "X-ray Magnetic Circular Dichroism," p. http://www.physics.montana.edu/magnetism/. [Online]. Available: http://www.physics.montana.edu/magnetism/

[71] P. Vavassori, "Polarization modulation technique for magneto-optical quantitative vector magnetometry," *Applied Physics Letters*, vol. 77, no. 11, pp. 1605–1607, 2000. [Online]. Available: http://ieeexplore.ieee.org/xpls/abs_all.jsp?arnumber=4904444

[72] G. Kresse and D. Joubert, "From ultrasoft pseudopotentials to the projector augmented-wave method," *Physical Review B*, vol. 59, no. 3, pp. 1758–1775, Jan. 1999. [Online]. Available: http://link.aps.org/doi/10.1103/PhysRevB.59.1758

[73] J. P. Perdew, K. Burke, and M. Ernzerhof, "Generalized Gradient Approximation Made Simple," *Physical Review Letters*, vol. 77, no. 18, pp. 3865–3868, Oct. 1996. [Online]. Available: http://link.aps.org/doi/10.1103/PhysRevLett.77.3865

[74] H. J. Monkhorst and J. D. Pack, "Special points for Brillouin-zone integrations," *Physical Review B*, vol. 13, no. 12, pp. 5188–5192, Jun. 1976. [Online]. Available: http://link.aps.org/doi/10.1103/PhysRevB.13.5188

[75] S. Dudarev and G. Botton, "Electron-energy-loss spectra and the structural stability of nickel oxide: An LSDA+ U study," *Physical Review ...*, vol. 57, no. 3, pp. 1505–1509, 1998. [Online]. Available: http://www.researchgate.net/publication/216328488_Electron-energy-loss_spectra_and_the_structural_stability_of_nickel_oxide_An_LSDAU_study/file/d912f508faead272b1.pdf

[76] G. Radaelli, S. Brivio, I. Fina, and R. Bertacco, "Correlation between growth dynamics and dielectric properties of epitaxial BaTiO3 films," *Applied Physics Letters*, vol. 100, no. 10, p. 102904, 2012. [Online]. Available: http://link.aip.org/link/APPLAB/v100/i10/p102904/s1&Agg=doi

[77] S. Brivio, C. Rinaldi, D. Petti, R. Bertacco, and F. Sanchez, "Epitaxial growth of Fe/BaTiO3 heterostructures," *Thin Solid Films*, vol. 519, no. 17, pp. 5804–5807, Jun. 2011. [Online]. Available: http://linkinghub.elsevier.com/retrieve/pii/S0040609010018596

[78] L. Bocher, A. Gloter, A. Crassous, V. Garcia, K. March, A. Zobelli, S. Valencia, S. Enouz-Vedrenne, X. Moya, N. D. Mathur, N. D. Marthur, C. Deranlot, S. Fusil, K. Bouzehouane, M. Bibes, A. Barthélémy, C. Colliex, and O. Stéphan, "Atomic and electronic structure of the BaTiO3/Fe interface in multiferroic tunnel junctions." *Nano letters*, vol. 12, no. 1, pp. 376–82, Jan. 2012. [Online]. Available: http://www.ncbi.nlm.nih.gov/pubmed/22191458

[79] V. Serin, S. Andrieu, R. Serra, F. Bonell, C. Tiusan, L. Calmels, M. Varela, S. Pennycook, E. Snoeck, M. Walls, and C. Colliex, "TEM and EELS measurements of interface roughness in epitaxial Fe/MgO/Fe magnetic tunnel junctions," *Physical Review B*, vol. 79, no. 14, p. 144413, Apr. 2009. [Online]. Available: http://link.aps.org/doi/10.1103/PhysRevB.79.144413

[80] R. Bertacco, M. Riva, M. Cantoni, L. Signorini, and F. Ciccacci, "Epitaxial La[2/3]Sr[1/3]MnO[3] thin films with metallic behavior above the Curie temperature," *Applied Physics Letters*, vol. 86, no. 25, p. 252502, 2005. [Online]. Available: http://link.aip.org/link/APPLAB/v86/i25/p252502/s1&Agg=doi

[81] G. Venkataiah, Y. Shirahata, I. Suzuki, M. Itoh, and T. Taniyama, "Strain-induced reversible and irreversible magnetization switching in Fe/BaTiO3 heterostructures," *Journal of Applied Physics*,

vol. 111, no. 3, p. 033921, 2012. [Online]. Available: http://link.aip.org/link/JAPIAU/v111/i3/p033921/s1&Agg=doi

[82] S. Yuasa, T. Nagahama, A. Fukushima, Y. Suzuki, and K. Ando, "Giant room-temperature magnetoresistance in single-crystal Fe/MgO/Fe magnetic tunnel junctions." *Nature materials*, vol. 3, no. 12, pp. 868–71, Dec. 2004. [Online]. Available: http://www.ncbi.nlm.nih.gov/pubmed/15516927

[83] a. Cattoni, D. Petti, S. Brivio, M. Cantoni, R. Bertacco, and F. Ciccacci, "MgO/Fe(001) and MgO/Fe(001)-p(1x1)O interfaces for magnetic tunnel junctions: A comparative study," *Physical Review B*, vol. 80, no. 10, p. 104437, Sep. 2009. [Online]. Available: http://link.aps.org/doi/10.1103/PhysRevB.80.104437

[84] T. Regan, H. Ohldag, C. Stamm, F. Nolting, J. Lüning, J. Stöhr, and R. White, "Chemical effects at metal/oxide interfaces studied by x-ray-absorption spectroscopy," *Physical Review B*, vol. 64, no. 21, p. 214422, Nov. 2001. [Online]. Available: http://link.aps.org/doi/10.1103/PhysRevB.64.214422

[85] J. Crocombette, M. Pollak, and F. Jollet, "X-ray-absorption spectroscopy at the Fe L_ {2, 3} threshold in iron oxides," *Physical Review B*, vol. 52, no. 5, pp. 3143–3150, 1995. [Online]. Available: http://prb.aps.org/abstract/PRB/v52/i5/p3143_1

[86] F. Bonell, Y. T. Takahashi, D. D. Lam, S. Yoshida, Y. Shiota, S. Miwa, T. Nakamura, and Y. Suzuki, "Reversible change in the oxidation state and magnetic circular dichroism of Fe driven by an electric field at the FeCo/MgO interface," *Applied Physics Letters*, vol. 102, no. 15, p. 152401, 2013. [Online]. Available: http://link.aip.org/link/APPLAB/v102/i15/p152401/s1&Agg=doi

[87] Y. Fan, K. J. Smith, G. Lüpke, a. T. Hanbicki, R. Goswami, C. H. Li, H. B. Zhao, and B. T. Jonker, "Exchange bias of the interface spin system at the Fe/MgO interface." *Nature*

nanotechnology, vol. 8, no. 6, pp. 438–44, Jun. 2013. [Online]. Available: http://www.ncbi.nlm.nih.gov/pubmed/23728074

[88] M. Fechner, S. Ostanin, and I. Mertig, "Effect of oxidation of the ultrathin Fe electrode material on the strength of magnetoelectric coupling in composite multiferroics," *Physical Review B*, vol. 80, no. 9, p. 094405, Sep. 2009. [Online]. Available: http://link.aps.org/doi/10.1103/PhysRevB.80.094405

[89] Y. Tokura and Y. Tomioka, "Colossal magnetoresistive manganites," *Journal of Magnetism and Magnetic Materials*, vol. 200, no. 1-3, pp. 1–23, Oct. 1999. [Online]. Available: http://linkinghub.elsevier.com/retrieve/pii/S0304885399003522

[90] P. Schiffer, A. Ramirez, W. Bao, and S. Cheong, "Low Temperature Magnetoresistance and the Magnetic Phase Diagram of La1- xCaxMnO3," *Physical Review Letters*, vol. 75, no. 18, pp. 3336–3339, 1995. [Online]. Available: http://scholar.google.com/scholar?hl=en&btnG=Search&q=intitle:low+temperature+magnetoresistance+and+the+magnetic+phase+diagram+of+La1-xCaxMnO3#0

[91] C. H. Ahn, J.-M. Triscone, and J. Mannhart, "Electric field effect in correlated oxide systems." *Nature*, vol. 424, no. 6952, pp. 1015–8, Aug. 2003. [Online]. Available: http://www.ncbi.nlm.nih.gov/pubmed/12944958

[92] C. A. F. Vaz, J. Hoffman, Y. Segal, J. W. Reiner, R. D. Grober, Z. Zhang, C. H. Ahn, and F. J. Walker, "Origin of the Magnetoelectric Coupling Effect in Pb(Zr [0.2]Ti[0.8])O[3]/La[0.8]Sr[0.2]MnO[3] Multiferroic Heterostructures," *Physical Review Letters*, vol. 104, no. 12, p. 127202, Mar. 2010. [Online]. Available: http://link.aps.org/doi/10.1103/PhysRevLett.104.127202

[93] S. Mathews, R. Ramesh, T. Venkatesan, and J. Benedetto, "Ferroelectric Field Effect Transistor Based on Epitaxial Perovskite

Heterostructures," *Science*, vol. 276, no. 5310, pp. 238–240, Apr. 1997. [Online]. Available: http://www.sciencemag.org/cgi/doi/10.1126/science.276.5310.238

[94] Y. Konishi, Z. Fang, M. Izumi, T. Manako, M. Kasai, H. Kuwahara, M. Kawasaki, K. Terakura, and Y. Tokura, "Orbital-State-Mediated Phase-Control of Manganites," *Journal of the Physics Society Japan*, vol. 68, no. 12, pp. 3790–3793, Dec. 1999. [Online]. Available: http://jpsj.ipap.jp/link?JPSJ/68/3790/

[95] A. Baena, L. Brey, and M. Calderón, "Effect of strain on the orbital and magnetic ordering of manganite thin films and their interface with an insulator," *Physical Review B*, vol. 83, p. 064424, 2011. [Online]. Available: http://prb.aps.org/abstract/PRB/v83/i6/e064424

[96] Z. Fang, I. Solovyev, and K. Terakura, "Phase diagram of tetragonal manganites," *Physical review letters*, vol. 84, no. 14, pp. 3169–72, Apr. 2000. [Online]. Available: http://www.ncbi.nlm.nih.gov/pubmed/11019039

[97] A. Millis, "Lattice effects in magnetoresistive manganese perovskites," *Nature*, vol. 392, no. March, pp. 147–150, 1998. [Online]. Available: http://www.nature.com/nature/journal/v392/n6672/abs/392147a0.html

[98] Y. M. Xiong, G. Y. Wang, X. G. Luo, C. H. Wang, X. H. Chen, X. Chen, and C. L. Chen, "Magnetotransport properties in La[1-x]Ca[x]MnO[3] (x=0.33, 0.5) thin films deposited on different substrates," *Journal of Applied Physics*, vol. 97, no. 8, p. 083909, 2005. [Online]. Available: http://link.aip.org/link/JAPIAU/v97/i8/p083909/s1&Agg=doi

[99] M. Malfait, I. Gordon, V. Moshchalkov, Y. Bruynseraede, G. Borghs, and P. Wagner, "Sign inversion of the high-field Hall slope in epitaxial La0.5Ca0.5MnO3 thin films," *Physical Review B*,

vol. 68, no. 13, p. 132410, Oct. 2003. [Online]. Available: http://link.aps.org/doi/10.1103/PhysRevB.68.132410

[100] a. Antonakos, D. Lampakis, E. Liarokapis, M. Filippi, W. Prellier, G. H. Aydogdu, and H.-U. Habermeier, "Phase separation in manganite thin films," *Journal of Physics: Condensed Matter*, vol. 20, no. 43, p. 434232, Oct. 2008. [Online]. Available: http://stacks.iop.org/0953-8984/20/i=43/a=434232?key=crossref.764fb8ec142ac4c9002a2b8792d3befc

[101] S. Estrade, J. M. Rebled, J. Arbiol, F. Peiro, I. C. Infante, G. Herranz, F. Sanchez, J. Fontcuberta, R. Cordoba, B. G. Mendis, and A. Bleloch, "Effects of thickness on the cation segregation in epitaxial (001) and (110) La[2/3]Ca[1/3]MnO[3] thin films," *Applied Physics Letters*, vol. 95, no. 7, p. 072507, 2009. [Online]. Available: http://link.aip.org/link/APPLAB/v95/i7/p072507/s1&Agg=doi

[102] J. Gazquez, S. Bose, M. Sharma, M. a. Torija, S. J. Pennycook, C. Leighton, and M. Varela, "Lattice mismatch accommodation via oxygen vacancy ordering in epitaxial La[0.5]Sr[0.5]CoO[3-δ] thin films," *APL Materials*, vol. 1, no. 1, p. 012105, 2013. [Online]. Available: http://link.aip.org/link/AMPADS/v1/i1/p012105/s1&Agg=doi

[103] Z. Jirak, J. Hejtmanek, K. Knizek, M. Marysko, V. Sima, and R. Sonntag, "Ferromagnetic-antiferromagnetic transition in tetragonal La[0.50]Sr[0.50]MnO[3]," *Journal of Magnetism and Magnetic Materials*, vol. 217, no. 1-3, pp. 113–119, Jul. 2000. [Online]. Available: http://linkinghub.elsevier.com/retrieve/pii/S0304885300003267

List of Figures

List of Tables